

Modeling Microstructural Evolution of Microalloyed Forging Steels During Thermomechanical Processing

by

Tianjun Liu

A thesis submitted to the Department of Materials and Metallurgical Engineering in
conformity with the requirements for the degree of Doctor of Philosophy

Queen's University
Kingston, Ontario
Canada

September, 2001

Copyright © Tianjun Liu, 2001



**National Library
of Canada**

**Acquisitions and
Bibliographic Services**

395 Wellington Street
Ottawa ON K1A 0N4
Canada

**Bibliothèque nationale
du Canada**

**Acquisitions et
services bibliographiques**

395, rue Wellington
Ottawa ON K1A 0N4
Canada

Your file Votre référence

Our file Notre référence

The author has granted a non-exclusive licence allowing the National Library of Canada to reproduce, loan, distribute or sell copies of this thesis in microform, paper or electronic formats.

L'auteur a accordé une licence non exclusive permettant à la Bibliothèque nationale du Canada de reproduire, prêter, distribuer ou vendre des copies de cette thèse sous la forme de microfiche/film, de reproduction sur papier ou sur format électronique.

The author retains ownership of the copyright in this thesis. Neither the thesis nor substantial extracts from it may be printed or otherwise reproduced without the author's permission.

L'auteur conserve la propriété du droit d'auteur qui protège cette thèse. Ni la thèse ni des extraits substantiels de celle-ci ne doivent être imprimés ou autrement reproduits sans son autorisation.

0-612-63433-7

Canada

To my family

Abstract

Thermomechanical processing has been extensively studied in the past decades. At the same time, modeling microstructural evolution has become a powerful tool for materials and process design by providing quantitative relations between microstructure, composition and processing. Much less attention has been paid to the thermomechanical processing of hot forging. This process is different from flat rolling. In addition to the different deformation geometry, the steels have higher carbon contents and the reheat treatment is faster. Induction heating is widely used in forging, which has a much higher heating rate and shorter holding time than conventional furnace heating.

This study focused on the microstructural evolution of microalloyed forging steels during induction reheat and after hot deformation. Four materials were studied: 1541Nb (0.41C-1.67Mn-0.038Nb-0.013S-0.005N), 1541VTi (0.40C-1.49Mn-0.11V-0.014Ti-0.042S-0.009N), 1541Al (0.40C-1.48Mn-0.023Al-0.026S-0.006N), and 1141Nb (0.39C-1.51Mn-0.046Nb-0.12S-0.005N).

Three investigations were carried out: (1) Grain growth and precipitate evolution during induction reheat; (2) Effect of initial microstructure on grain growth during induction reheat; and (3) Recrystallization kinetics following hot deformation.

A physical model was established to predict the evolution of the precipitate size distribution during continuous heating, resulting from diffusion-controlled precipitate dissolution followed by coarsening. The Zener equation for particle pinning was modified to incorporate the effect of a distribution of precipitate sizes. Starting from the initial precipitate size distribution in the bar stock, the models predict the precipitate size

distribution and the mean grain diameter at all stages of the heating cycle. The predicted results agree well with the experimental observations.

Different initial microstructures were produced by preheating as-rolled 1141Nb steel bar, and the grain growth behaviour was determined for each preheated condition. Reprecipitation occurred in the pre-quenched samples at 900-1000°C which resulted in smaller grain sizes at intermediate reheat temperatures. Grain growth and precipitate evolution were accurately predicted by the models provided no additional precipitates formed during reheat.

The measured recrystallization kinetics were fitted to the Avrami equation and a generalized equation for the recrystallization rate in the absence of strain-induced precipitation was determined for 1541Nb and 1541VTi. Classical nucleation theory was extended for complex carbonitrides and the onset of strain-induced precipitation was calculated to explain the observed recrystallization behaviour.

Table of Contents

1. Introduction	1
1.1 Microalloyed Forging Steels and Thermomechanical Processing	1
1.2 Objective of Study	2
2. Literature Review	5
2.1 Stability of Carbonitride Precipitates	5
(A) Solubility product of simple compounds	5
(B) Effect of surface curvature on solubility	8
(C) Solubility of complex compounds	9
2.2 Precipitate Growth, Dissolution and Coarsening Kinetics	10
(A) Precipitate growth and dissolution	10
(B) Precipitate coarsening	13
(C) Precipitate evolution during continuous heating	14
2.3 Grain Growth	15
(A) Empirical equations for grain growth	16
(B) Physical modeling of grain growth	17
2.4 Recrystallization	20
(A) Avrami kinetics	20
(B) Recrystallization kinetics of microalloyed steels	22
2.5 Strain-Induced Precipitation	25
(A) Chemical driving force	26
(B) Critical free energy for nucleation	27
(C) Nucleation rate	28

(D) Precipitation-start time	29
2.6 Summary	30
3. Experimental	31
3.1 Experimental Materials	31
3.2 Experimental Procedures	32
(A) Grain growth and precipitate evolution during induction heating	32
(B) Effect of initial microstructure on grain growth during induction reheat	34
(C) Recrystallization following hot deformation	35
3.3 Microstructure Characterization	39
4. Grain Growth and Precipitate Evolution During Induction Heating	44
4.1 Microstructures of As-Rolled Bar	44
4.2 Grain Growth During Induction Reheat	47
4.3 Precipitate Evolution During Induction Reheat	51
4.4 Discussion of Grain Growth & Precipitate Evolution During Induction Reheat	55
4.5 Modeling Precipitate Dissolution-Coarsening During Induction Heating	57
(A) Dissolution and coarsening of a distribution of precipitate sizes	57
(B) Precipitate dissolution and coarsening during continuous heating	60
(C) Precipitate evolution during induction heating	62
4.6 A Modified Zener Equation for a Distribution of Precipitate Sizes	65
(A) Derivation of the expression	66
(B) Evaluating the modified Zener equation	69
4.7 Modeling Grain Growth During Induction Heating	71

5. Effect of Microstructure on Grain Growth During Induction Reheat	74
5.1 Microstructures of As-Rolled Bar and After Preheat Treatment	74
5.2 Grain Growth During Induction Reheat	74
5.3 Precipitate Evolution	80
5.4 Discussion	86
6. Recrystallization After Hot Deformation	90
6.1 Stress-strain Curves During Deformation	90
6.2 Recrystallization Fraction and Softening Fraction	90
6.3 Microstructural Observation	94
6.4 Modeling Recrystallization Kinetics	102
6.5 Modeling Strain-Induced Precipitation	104
7. Summary	110
8. References	114
Appendix A. Calculation of Equilibrium Solubility of Complex Carbonitrides	129
A.1 Nb(C,N) type of carbonitrides	129
A.2 (Nb,V)(C,N) type of carbonitrides	131
A.3 (M ₁ ,...,M _n)(C,N) type of carbonitrides.	136
Appendix B. Calculation of Precipitate Evolution During Induction Heating	141
Appendix C. Calculation of Grain Growth During Induction Heating	154
Appendix D. Chemical Driving Force for Precipitation of (Ti,V)(C,N) Type Carbonitrides	157
Appendix E. Calculation of Strain-Induced Precipitation	160

List of Tables

Table 2.1 Typical mechanisms of microstructural evolution and controlling factors during TMP	5
Table 2.2. Solubility products for precipitate phases in microalloyed steels	7
Table 2.3 Lattice constant, density, mole volume and stoichiometry of microalloy carbonitrides	8
Table 2.4 Growth and dissolution kinetics of spherical precipitates	12
Table 2.5 Diffusion coefficients of microalloy elements in austenite	14
Table 2.6 Summary of empirical equations describing austenite grain growth	16
Table 2.7 Static recrystallization kinetics of plain carbon steels	21
Table 2.8 Static recrystallization kinetics of microalloyed steels	23
Table 3.1 Chemical compositions of the experimental steels (wt%)	31
Table 4.1 Precipitates in as-rolled steel bars	47

Table of Figures

Figure 2.1	Schematic concentration fields for growth and dissolution.	11
Figure 2.2	Free energy change with precipitate radius (1541Nb).	28
Figure 3.1	Schematic shows the sample location from the steel bar.	31
Figure 3.2	TRW induction heating cycle.	32
Figure 3.3	Schematic of quench-deformation dilatometer.	33
Figure 3.4	Welland Forge induction heating cycle.	34
Figure 3.5	Preheat treatments to produce four different initial microstructures.	35
Figure 3.6	The process for double-hit and single-hit experiments.	36
Figure 3.7	Schematic of cam plastometer.	37
Figure 3.8	Typical stress-strain curves from a double-hit test illustrating the method to determine softening fraction.	38
Figure 3.9	Schematic of etching apparatus for prior austenite grain boundaries.	40
Figure 3.10	Schematic of carbon evaporator.	41
Figure 3.11	Schematic of the basic procedures for preparing carbon replicas.	42
Figure 4.1	The microstructures (pearlite + ferrite) of the as-rolled bar.	45
Figure 4.2	Precipitate distributions at as-rolled bar.	46
Figure 4.3	Typical austenite grain microstructure in 1541Nb after 6s holding at different temperatures.	48
Figure 4.4	Austenite grain diameter as a function of heating temperature and holding time.	50
Figure 4.5	Typical precipitate distributions after 6s hold at different temperatures.	52

Figure 4.6	Measured precipitate size distributions for as-rolled condition and after induction reheat with 6s hold (1541Nb).	53
Figure 4.7	Schematic of the variation in precipitate size and volume fraction during dissolution and coarsening.	58
Figure 4.8	Schematic of calculation procedures for microstructural evolution during induction heating.	61
Figure 4.9	Effect of heating temperature on volume fraction and mean precipitate diameter for 6s hold (1541Nb).	63
Figure 4.10	Effect of temperature on precipitate dissolution (1541Nb).	63
Figure 4.11	Variation of precipitate diameter with temperature during continuous heating (1541Nb).	64
Figure 4.12	Schematic of Zener pinning from a group of precipitates of different sizes.	66
Figure 4.13	Schematic of a small section in a distribution of precipitate sizes.	67
Figure 4.14	Schematic illustration of the effect of precipitate size distribution on pinning force.	69
Figure 4.15	Effect of precipitate size distribution on equivalent precipitate size.	70
Figure 4.16	Variation in grain diameter with temperature and holding time (TRW heating cycle).	73
Figure 5.1	Initial microstructures of hot-rolled bar and after preheat (1141Nb).	75
Figure 5.2	Primary austenite grain structures following reheat for as-rolled microstructure (1141Nb).	76
Figure 5.3	Variation in mean grain diameter with reheat temperature for four	

	different initial microstructures.	80
Figure 5.4	Typical precipitate distributions of as-rolled bar and after preheat.	81
Figure 5.5	Evolution of precipitate size distributions during reheat for as-rolled conditions.	83
Figure 5.6	Reprecipitated precipitates after 1250Q+1000°C reheat.	86
Figure 5.7	Schematic of precipitate evolution from different initial microstructures.	87
Figure 5.8	Variation in grain diameter with temperature and holding time (Welland Forge cycle).	89
Figure 6.1	True stress - true strain curves with different temperatures and holding times (1541Nb).	91
Figure 6.2	True stress - true strain curves with different temperatures and holding times (1541VTi).	92
Figure 6.3	Softening fraction and recrystallization fraction vs. interruption time from double-hit and single hit tests.	93
Figure 6.4	Typical austenite microstructure of 1541VTi after deformation at 900°C.	95
Figure 6.5	Typical austenite microstructure after hot deformation.	96
Figure 6.6	Variation of austenite grain sizes with recrystallization.	97
Figure 6.7	Precipitate distribution in 1541VTi. (a) Undissolved precipitates (b) Strain-induced precipitates.	99
Figure 6.8	Typical precipitate size distributions before and after hot deformation (1541VTi).	100

Figure 6.9	Determining the constant values in Equation 6.3.	103
Figure 6.10	Determining the constant values in Equation 6.5.	104
Figure 6.11	Softening fraction predicted by the unified model compared with experimental data.	105
Figure 6.12	Chemical driving force of (Ti,V)(C,N) precipitation in 1541VTi and Nb(C,N) in 1541Nb.	107
Figure 6.13	Static recrystallization curves and the start time for strain-induced precipitation.	108
Figure A.1	Equilibrium solubility of V and Ti, volume fraction of precipitates, atomic fraction of Ti and C in precipitates at different temperatures (1541VTi).	136

List of Symbols

Ω_{CN} : regular solution parameter	D_c : critical grain diameter
δ_r : standard deviation of $\ln(r)$	D_m : bulk diffusion coefficient
$\rho(r)$: frequency of precipitates of radius r	f : mole fraction of precipitates
β^* : rate of atom addition to nucleus	FEA: finite element analysis
γ : austenite	F_p : precipitate pinning
α : ferrite	f_s : softening fraction
τ : incubation time	F_s : solute drag
ξ : modifier of interfacial energy	f_v : volume fraction of precipitates
λ : radius of surface curvature	f_r : recrystallization fraction
μ : shear modulus of austenite	\dot{G} : growth rate
μ_r : mean of $\ln(r)$	I : dirt factor
σ : standard deviation of precipitate sizes	K : equilibrium constant
ϵ : strain	k_A : Avrami constant
$\dot{\epsilon}$: strain rate	k_B : Boltzman's constant
ρ_d : dislocation density	k_s : supersaturation ratio
ΔG_n^* : critical nucleation energy	k_Z : constant in the Zener equation
ΔG : Gibbs free energy	LCN: regular solution parameter (Ω_{CN})
ΔG_{chem} : chemical driving force	M_{gb} : grain boundary mobility
ΔG_e : elastic energy	N : number of nucleation sites
ΔH : enthalpy of reaction	\dot{N} : nucleation rate
ΔS : entropy of reaction	P_d : driving pressure for grain growth
γ_{gb} : grain boundary energy	P_g : effective driving pressure for grain growth
γ_i : interfacial energy	P_z : Zener pinning pressure
a : activity/lattice constant	Q_d : activation energy for diffusion
b : Burgers vector	Q_{gg} : activation energy for grain growth
D : grain diameter	Q_x : activation energy for recrystallization
d : precipitate diameter	

R: gas constant/grain radius
r: precipitate radius
R_c: critical grain radius
r_d: radius of dislocation core
R_x: recrystallization grain radius
S: area
SRCT: static recrystallization critical temperature
T: absolute temperature
t_{0.05}: recrystallization-start time
t_{0.5}: 50% recrystallization time
T_d: complete dissolution temperature
t_d: complete dissolution time

TMP: thermomechanical processing
t^p_{0.05}: precipitation-start time
V: volume
x, y: atomic fraction of Ti (or Nb) and C in carbonitrides
X_i, X_p, X_∞: solute concentration of X at interface, in precipitates or matrix
[X] or X: solute concentration of element X
Z: Zeldovich non-equilibrium factor
Z_g: Gladman's non-uniform factor
Z': Zener-Holloman parameter

Chapter 1. Introduction

1.1 Microalloyed Forging Steels and Thermomechanical Processing

Medium carbon steels have been widely used as structural components where high strength, hardness and good toughness are required. Traditionally, the required properties were obtained by quenching and tempering treatment. The drawbacks of this process have been well recognized, such as high energy consumption, severe distortion, cracking, stress concentration, and insufficient hardenability during quenching operations.

Since the 1970s, a new class of steels has been developed for more effective processing. A small amount of microalloy elements (V, Ti or Nb) is added to the steel to improve strength and toughness. These medium-carbon microalloyed steels (also called "microalloyed forging steels") provide the same strength level by thermomechanical processing (TMP), thus the need for heat treatment is eliminated. Compared with the traditional heat treated steels, microalloyed forging steels exhibit not only simplified operation procedures, but also increased microstructural uniformity, better machinability, less stress concentration and improved dimensional stability. The toughness level, however, is lower.

Unlike heat treated steels where high strength and toughness are obtained by heat treatment, the mechanical properties of the microalloyed forging steels are highly dependent on their compositions and the TMP. The microstructure of microalloyed forging steels usually consists of pearlite and ferrite. The required strength level is mainly provided by grain refinement and precipitation strengthening from microalloy elements. Undissolved and precipitated microalloy carbonitrides prevent grain coarsening during heating and TMP, resulting in improved strength and toughness. Precipitation of microalloy carbonitrides in austenite and ferrite produces significant precipitation

strengthening, although this is accompanied by a decrease in toughness.

In order to improve mechanical properties of microalloyed forging steels, a high degree of microstructure refinement, proper amount of precipitates, and well-balanced, favorably distributed ferrite and pearlite phases are necessary. Consequently, control of microstructure through an optimization of chemistry and manufacturing process is important for the best use of TMP and the improvement of mechanical properties. Traditionally, this is achieved by laboratory-scale experiments and production-scale trials before mass production. Nowadays, the increase in cost, and the time needed for optimization become a serious problem.

1.2 Objective of Study

Modeling of microstructural evolution during TMP has been considered as a powerful tool for efficient development of high quality steels since the 1980s, which was first demonstrated by Sellars and Whiteman (1979). Their study showed that the evolution of microstructure during hot rolling of C-Mn steels could be predicted as a function of rolling schedule (temperature, reduction, speed, pass time) and initial microstructure. Relations describing static recrystallization and grain growth were derived from laboratory observations. Predictions made from the relations gave reasonable agreement with the microstructures observed in hot-rolled products.

The concept of microstructural evolution has been extended by the following studies to describe all the metallurgical transformations during TMP, including grain growth (Sellars, 1979; Hodgson and Gibbs, 1992; Anderson and Grong, 1995; Manohar *et al.*, 1996); recovery and recrystallization (Roberts *et al.*, 1986; Sunuma and Yada, 1988;

Humphreys, 1992; Yoshie *et al.* 1992; Kuziak, 1994 and 1996); precipitate dissolution and coarsening (Agren, 1982; Saito *et al.*, 1988); strain-induced precipitation (Dutta and Sellars, 1987; Liu and Jonas, 1988; Militzer *et al.*, 1992); austenitization and austenite decomposition (Akbay *et al.*, 1994; Garcia de Andres *et al.*, 1998; Puskar *et al.* 1999); and integrated modeling of various TMP processes (Devadas *et al.*, 1991; Ashby, 1992; Anelli, 1992; Kwon, 1992; Pietrzyk *et al.*, 1994; Majta *et al.*, 1996; Saito, 1997). Both empirical equations and mathematical models have been established for precise process control.

Most of the studies have been focused on microstructural evolution of C-Mn steels and low-carbon microalloyed steels during hot rolling. Much less attention has been paid to hot forging processes, especially for microalloyed forging steels. In the limited literature (Gegel *et al.*, 1988; Howson and Delgado, 1989; Duggirala, 1990; Delgada *et al.*, 1994; Pietrzyk *et al.*, 1994a,b; Kuziak *et al.*, 1994 and 1996; Almaguer *et al.*, 1999; Wang *et al.*, 1999), most of the work focused on finite element analysis of non-uniform temperature and strain distributions in the forged parts, rather than on metallurgical characteristics of the forged materials and the processes.

Microstructural evolution during rapid induction heating is an area in need of study. Compared with traditional furnace heating, induction heating has much faster heating rate and short holding time. A typical induction heating cycle takes only a few minutes or shorter (Simpson, 1960). Under such rapid heating, it is expected that both grain growth behaviour and precipitate evolution will be different to the well-studied furnace reheating.

One example is the interesting phenomenon observed by Welland Forge. During

forging operations, most of the hot-rolled steel billets are forged after induction heating. Occasionally, however, the billets are heated but not forged because the forging operation is interrupted or the billets are overheated. These unforged billets are cooled down to room temperature either by air cooling or by water quench, and then recharged later for a second induction heating cycle. It has been found that the final grain sizes of hot-forged products varied with the preheat cycle. Compared with the hot-rolled billets, the final microstructures of preheated + air-cooled billets are coarsened and non-uniform, while those of preheated + water-quenched billets are refined.

To understand these phenomena, the microstructural evolution during induction heating and forging needs to be determined. Furthermore, empirical relations or physical models need to be derived for precise process control. In view of this, a research consortium of nine steel and automotive manufacturers was formed in 1997 to investigate the physical metallurgy of microalloyed forging steels. The main objective of this project is to develop alloys and processes to achieve improved toughness and machinability. This thesis work is an important part of the project.

This thesis has focused on modeling microstructural evolution of microalloyed forging steels during TMP. Grain growth and precipitate evolution during induction heating, and recrystallization and strain-induced precipitation after hot deformation, have been investigated by experiments. Physical models and empirical equations were derived to simulate metallurgical processes, and the predictions of the models were verified by experimental observations.

Chapter 2. Literature Review

A typical TMP schedule includes three stages: heating, forming and cooling. The controlling factors at each stage and the related mechanisms are summarized in Table 2.1. The microstructural evolution mechanisms considered in this thesis are: carbonitride dissolution, carbonitride coarsening and austenite grain growth during induction heating, austenite recrystallization and strain-induced precipitation after hot deformation. The literature on these mechanisms is briefly reviewed in the following sections.

Table 2.1 Typical mechanisms of microstructural evolution and controlling factors during TMP

TMP process	Controlling factor	Microstructural evolution mechanisms
Heating	heating temperature, time and heating rate	austenization, grain growth, carbonitride dissolution and coarsening
Forming (in recrystallization zone)	deformation temperature, reduction, time interval	recrystallization, grain growth, carbonitride precipitation
Forming (in non-recrystallization zone)		deformed microstructure, carbonitride precipitation
Cooling	start- and finish-cooling temperature, cooling rate	austenite decomposition

2.1 Stability of Carbonitride Precipitates

The solubility product has been widely used to define the equilibrium solubility of carbonitride precipitates. The difference between actual solute concentration and equilibrium solubility can be used to determine the chemical driving force for precipitate dissolution and precipitation.

(A) Solubility product of simple compounds

The solubility product for simple compounds like A_nB_m can be derived from the Gibbs free energy ΔG^0 of the following reaction (Martin and Doherty, 1976):



where [A] and [B] is the solute concentration (in mole fraction) of atoms A and B respectively. n and m are the atomic fraction of A and B respectively in the compound.

After equilibrium at temperature T, we have:

$$\Delta G^0 = \Delta H^0 - T\Delta S^0 = -RT \ln K = -RT \ln 10 \times \log \frac{a_A^n a_B^m}{a_{A_n B_m}} \quad [2.2]$$

where ΔH^0 and ΔS^0 are the enthalpy and entropy of the reaction, respectively. K is the equilibrium constant. a_A , a_B and $a_{A_n B_m}$ are the activities of A, B and $A_n B_m$ in the solution, respectively. R is gas constant. Base 10 logarithm is usually used for the solubility product expressions.

When pure $A_n B_m$ is set as the standard state, the activity of the compound ($a_{A_n B_m}$) is equal to unity. For a dilute solution, it is a fair approximation to set $a_A=[A]$ and $a_B=[B]$, where the units can be in either wt% or at%. Hence, Equation 2.2 can be written as:

$$\log[A]^n [B]^m = \frac{\Delta S^0}{R \ln 10} - \frac{\Delta H^0}{RT \ln 10} = p - \frac{q}{T} \quad [2.3]$$

where p and q are constants.

The above derivation is suitable for microalloyed steels since the microalloy content in these steels is very low, usually less than 0.1wt% and the solution is dilute. Table 2.2 gives a summary of solubility product equations for microalloy carbonitrides.

The complete dissolution temperature (T_d) of the precipitates can be determined by rearranging Equation 2.3:

$$T_d = \frac{q}{p - \log[A]^n [B]^m} \quad [2.4]$$

Table 2.2 Solubility products for precipitate phases in microalloyed steels (Strid and Easterling, 1985; Yong *et al.*, 1989)

No	Compound	Expression	p	q
1			-0.63	2500
2*			4.37	9290
3	NbC	$K=[Nb][C]$	3.70	9100
4			3.04	7290
5			3.3	7900
6	NbC ^{0.87}	$K=[Nb][C]^{0.87}$	3.18	7700
7			3.11	7520
8*	NbN	$K=[Nb][N]$	4.04	10230
9			3.70	10800
10		$K=[Nb][C+N]$	1.54	5860
11	Nb(C,N)	$K=[Nb][C+^{12/14}N]$	2.26	6770
12		$K=[Nb][C]^{0.83}[N]^{0.14}$	4.46	9800
13*	TiC	$K=[Ti][C]$	2.75	7500
14			2.0	20790
15	TiN	$K=[Ti][N]$	6.75	19740
16*			0.322	8000
17			3.82	15020
18*	VC	$K=[V][C]$	6.72	9500
19			2.27	7070
20*	VN	$K=[V][N]$	3.46	8330
21			3.46+0.12[Mn]	8330
22			1.033	6770
23			0.725	6180
24	AlN	$K=[Al][N]$	1.95	7400
25			1.8	7750
26			1.48	7500

* These equations are used for the calculations in this study.

With the solubility product and ideal stoichiometry, the equilibrium solute concentration and the volume fraction of the undissolved precipitates can be calculated. Some of the related data are listed in Table 2.3.

Table 2.3 Lattice constant, density, mole volume and stoichiometry of microalloy carbonitrides (Yong *et al.*, 1989)

Compound	Lattice	Lattice constant (Å)	Density (g/cm ³)	Mole volume (cm ³ /mol)	stoichiometry (weight ratio)
VC	fcc	4.19	5.68	11.1	4.24
VN	fcc	4.09	6.30	10.3	3.64
TiC	fcc	4.33	4.91	12.2	3.99
TiN	fcc	4.24	5.39	11.5	3.42
NbC	fcc	4.47	7.80	13.5	7.74
NbN	fcc	4.39	8.39	12.7	6.63

(B) Effect of surface curvature on solubility

The above derivation does not take the effect of surface curvature into account. To reflect this effect, a simple way is to combine a solubility product equation with the Gibbs-Thompson equation (Trivedi, 1986). For a spherical particle of a simple compound like A_nB_m , we have

$$\Delta G^0 = \Delta H^0 - T\Delta S^0 - \frac{2\gamma_i V_m}{r} = -RT \ln([A]^n [B]^m) \quad [2.5]$$

where γ_i is the interfacial energy between precipitate and matrix. V_m is the molar volume of the precipitate and r is the precipitate radius. Similar to the above derivations, we have

$$\log[A]^n [B]^m = \frac{1}{\ln 10} \left(\frac{\Delta S}{R} - \frac{\Delta H_0}{RT} + \frac{2\gamma_i V_m}{RT r} \right) = \left(p - \frac{q}{T} \right) + \frac{2\gamma_i V_m}{RT r \ln 10} \quad [2.6]$$

where the last term at the right-hand side gives the Gibbs-Thompson effect. It can be found that small precipitates have higher solubility than larger ones. The variation of solubility of precipitates of different sizes provides the driving force for precipitate coarsening.

(C) Solubility of complex compounds

Some basic assumptions are necessary to calculate solubility of complex compounds: (1) perfect stoichiometry, i.e., the atomic fraction of microalloy elements in the precipitate is equal to that of C and N; (2) microalloy carbides and nitrides are completely soluble; (3) the multi-component carbonitride may be considered as a combination of binary carbides and nitrides. The remaining problem is to express the free energy of the complex compound as a function of those of the binary compounds.

For Nb(C,N)-type precipitates, it has been assumed by Hudd *et al.* (1971) that the free energy of the carbonitride varies linearly from pure NbC to pure NbN. The entropy of mixing is taken into account but the enthalpy of mixing is neglected. Then

$$\ln K = y \ln K_{\text{NbC}} + (1-y) \ln K_{\text{NbN}} + y \ln y + (1-y) \ln(1-y) \quad [2.7]$$

where y is the atomic fraction of carbon in the precipitate and K_{NbC} and K_{NbN} are the solubility products of NbC and NbN respectively. A group of two equations can be derived as follows:

$$yK_{\text{NbC}} = [\text{Nb}] \left\{ C_0 - y(\text{Nb}_0 - [\text{Nb}]) \frac{M_{\text{C}}}{M_{\text{Nb}}} \right\} \quad [2.8a]$$

$$(1-y)K_{\text{NbN}} = [\text{Nb}] \left\{ N_0 - (1-y)(\text{Nb}_0 - [\text{Nb}]) \frac{M_{\text{N}}}{M_{\text{Nb}}} \right\} \quad [2.8b]$$

where C_0 , N_0 and Nb_0 are the wt% of C, N and Nb in the steel respectively and M_{C} , M_{N} and M_{Nb} are the atomic weights of carbon, nitrogen and niobium respectively. There are two unknowns, $[\text{Nb}]$ and y , in the two equations. Their values can be found by numerical methods. Then all other values of interest (volume fraction of precipitate, carbon and nitrogen concentrations in solution) can be obtained. A computer program has been written to carry out this calculation, and is given in Appendix A.

The methods for determining the solubility of more complex carbonitrides have been given by Speer *et al.* (1987), Rios (1991) and other researchers (Zou and Kirkaldy, 1991; Adrian, 1992; Prikryl *et al.*, 1996). A brief summary of the first two methods and the calculation programs are also given in Appendix A.

2.2 Precipitate Growth, Dissolution and Coarsening Kinetics

(A) Precipitate Growth and Dissolution

The concentration fields for growth and dissolution of an isolated precipitate in an infinite matrix are shown in Figure 2.1. In any transformations involving long-range diffusion, the following equation (Aaron *et al.*, 1971)

$$D_m \nabla^2 X = \frac{\partial X}{\partial t} \quad [2.9]$$

must be satisfied. Where D_m is the diffusion coefficient of the solute element, X is the solute concentration and t is time.

For Equation 2.9, we have the following boundary conditions:

$$X(r = r_i, t) = X_i \quad (0 < t \leq \infty) \quad [2.10a]$$

and

$$X(r, t = 0) = X_\infty \quad (r \geq r_i) \quad [2.10b]$$

or

$$X(r = \infty, t) = X_\infty \quad (0 \leq t \leq \infty) \quad [2.10c]$$

where $r=r_i$ at the precipitate/matrix interface, X_i is the concentration in the matrix at the interface and X_∞ is the concentration at a point far from the precipitate. The flux balance must also be satisfied:

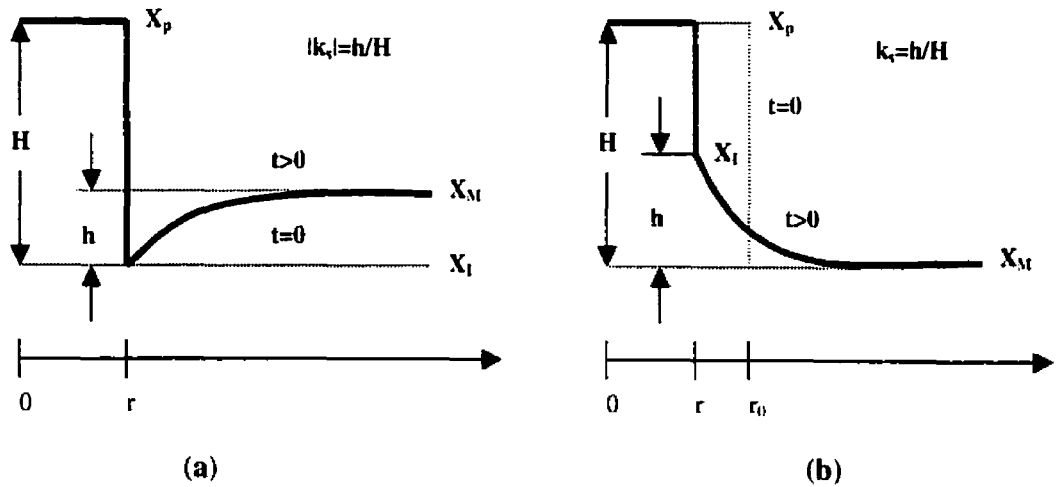


Figure 2.1 Schematic concentration fields for precipitate growth (a) and dissolution (b). k_s is a constant (Aaron *et al.*, 1971).

$$(X_p - X_I) \frac{dr}{dt} = D_m \left. \frac{\partial X}{\partial t} \right|_{r=r} \quad [2.11]$$

where X_p , the composition of the precipitate, is assumed constant and independent of r and t .

Exact solutions of Equation 2.9 are often difficult if not impossible to obtain. Several approximations have been proposed to simplify the calculation. Aaron *et al.* (1970) summarized the studies on this topic and classified the previous work into three groups: (1) Invariant-field approximation, which simplifies the field equation by setting $\partial X/\partial t=0$ and r_i is constant. Therefore, the diffusion rate is not a function of time; (2) Invariant-size approximation, which assumes $dr_i/dt=0$. Thus, the effect of a moving interface on the diffusion field is neglected; and (3) Linearized-gradient approximation, which assumes that the concentration gradient immediately surrounding the precipitate is linear to r . The solutions from these approximations are given in Table 2.4.

Table 2.4 Growth and dissolution kinetics of spherical precipitates

	Precipitate growth ($R = \lambda_i \sqrt{D_m t}$)	Precipitate dissolution
Exact solution	$\lambda^2 \exp(\lambda^2) [\exp(-\lambda^2) - \lambda \sqrt{\lambda} \operatorname{erfc}(\lambda)] = -\frac{k_s}{4}$ $\lambda_1 = 2\lambda$	No exact solution.
Invariant-field approximation	$\lambda_2 = \sqrt{-k_s}$	$r^2 = r_0^2 - 2k_s D_m t$
Invariant-size approximation	$\lambda_1 = -\frac{k_s}{2\sqrt{\pi}} + \sqrt{\frac{k_s^2}{4\pi} - k_s}$	$\ln(y + 2py\sqrt{\tau} + \tau) = \frac{-2p}{\sqrt{1-p^2}} \operatorname{arctan} \frac{\sqrt{1-p^2}}{\frac{y}{\sqrt{\tau}} + p}$ where $y = \frac{r}{r_0}$, $\tau = \frac{a^2 t}{r_0^2}$, $a^2 = k_s D_m$, $p^2 = \frac{k_s}{4\pi}$
Linearized-gradient approximation	$f(k_s) = \sqrt{\frac{-4k_s}{1+4k_s}}$, $\eta = \frac{1-f(k_s)}{f(k_s)}$ $\lambda_1 = \sqrt{-\frac{k_s}{\eta}}$	Sufficiently complex to negate its usefulness.

Aaron *et al.* (1970 and 1971) suggested that for most alloys of $k_s < 0.1$ (k_s is defined in Figure 2.1) the invariant-size approximation gives close results for both precipitate growth and dissolution. However, because of the complex form of the invariant-size approximation, it cannot be solved analytically and hence numerical methods have to be applied. For microalloyed steels, where k_s is very low, the simplest form given by the invariant-field approximation provides sufficient accuracy. Therefore, it has been extensively applied for precipitate growth and dissolution. For precipitate growth:

$$r^2 = r_0^2 + 2k_s D_m t \quad [2.12]$$

and for precipitate dissolution:

$$r^2 = r_0^2 - 2k_s D_m t \quad [2.13]$$

where r_0 is the initial precipitate radius.

(B) Precipitate coarsening

The model for diffusion-controlled precipitate coarsening kinetics was derived rigorously by Greenwood, Lifshitz and Slyozov, and Wagner (Martin and Doherty, 1976). Briefly, for a precipitate of size r in a group of precipitates of mean size \bar{r} , its size evolution can be given by:

$$\frac{\partial r}{\partial t} = \frac{2D_m \gamma_i V_m X_\infty}{RT r} \left(\frac{1}{\bar{r}} - \frac{1}{r} \right) \quad [2.14]$$

where X_∞ is the solute concentration for precipitates of infinitely large size. It is found that the precipitates of radii larger than the mean value grow, while those of $r < \bar{r}$ shrink. Eventually the small precipitates dissolve and the mean precipitate size increases. With some assumptions, this equation can be integrated to give the well-known Lifshitz-Slyozov-Wagner (LSW) equation:

$$\bar{r}^3 - \bar{r}_0^3 = \frac{8 D_m \gamma_i V_m X_\infty}{9 RT} t \quad [2.15]$$

The diffusion coefficient in the above equations is a function of temperature, which can be described as:

$$D_m = D_m^0 \exp\left(-\frac{Q_d}{RT}\right) \quad [2.16]$$

where D_m^0 is a constant and Q_d the activation energy for diffusion. Some of the diffusivity data for microalloy elements are listed in Table 2.5.

For multi-component diffusion, it is necessary to determine the rate-controlling element. Compared with microalloy elements, the interstitials (C and N) have much faster diffusivities in austenite. Of the three microalloy elements, the diffusion coefficient

Table 2.5 Diffusion coefficients of microalloy elements in austenite (Ashby and Easterling, 1982)

Solute	$D_m^{0.5}$ (mm ² /s)	Q_d (kJ/mol)	Solute	$D_m^{0.5}$ (mm ² /s)	Q_d (kJ/mol)
C	67	157	Nb	492	285
N	91	169	V	365	70
Ti	15	250			

decreases in the order of V, Nb and Ti. Therefore, the one with the slowest diffusivity is considered as the rate-controlling element.

(C) Precipitate evolution during continuous heating

Precipitate evolution during continuous heating has been studied for the heat-affected zone during welding (Ion *et al.*, 1984; Loberg *et al.*, 1984; Strid and Easterling, 1985; Akselsen *et al.*, 1986; Suzuki *et al.*, 1987; Wang *et al.*, 1989; Anderson and Grong, 1995; Grong, 1997). A main subject of these studies was to extend the precipitate coarsening/dissolution equations so that they are applicable for continuous heating. For precipitate coarsening, Ion *et al.* (1984) gave:

$$r^1 - r_0^1 = c_1 \int_{t_0}^{t_1} \frac{1}{T} \exp\left(-\frac{Q_d}{RT}\right) dt \quad [2.17]$$

where c_1 is a constant. For precipitate dissolution, Anderson and Grong (1995) suggested:

$$r^2 = r_0^2 - \int_{t_0}^{t_1} 2k_p D_m dt \quad [2.18]$$

Obviously, these are modified equations of precipitate coarsening and dissolution during isothermal holding.

The volume fraction of precipitates changes with precipitate dissolution. It cannot be calculated from solubility product data since equilibrium may not be reached within such a rapid cycle like welding. Ashby and Easterling (1982) gave the following equation:

$$f_v = 1 - \exp\left\{-\frac{t}{t^*} \exp\left[-\frac{Q_d}{R} \left(\frac{1}{T} - \frac{1}{T^*}\right)^2\right]\right\} \quad [2.19]$$

where T^* and t^* are the temperature and time at which the volume fraction of precipitates is known. These values are difficult to obtain, which limits the application of the equation. Agren (1990) gave a relative relationship to estimate the change of volume fraction:

$$\frac{f_v}{f_v^0} = \left(\frac{r}{r_0}\right)^3 \quad [2.20]$$

where f_v^0 is the initial volume fraction of precipitates. From this equation, it is found that with the increase of temperature, both the volume fraction and the mean diameter of the precipitates decrease.

2.3 Grain Growth

Grain growth during slow furnace reheat has been extensively studied (Gladman and Pickering, 1967; Hannerz and Kazinczy, 1970; Gladman and Dulieu, 1974; Kurtz, 1980; Cuddy and Raley, 1983; Kaspar and Mahmoud, 1991; Pickering, 1994; Manohar *et al.*, 1996; Militzer *et al.* 1996; Gladman, 1997). Two methods have been most widely used for the modeling of grain growth: empirical equations based on a power law and physical models based on Zener pinning.

(A) Empirical Equations for Grain Growth

Empirical equations have been widely used to describe grain growth behavior during isothermal heating. The power law relationship was first given by Beck *et al.* (1948a,b) for normal grain growth during isothermal annealing:

$$D^n - D_0^n = k_1 t \quad [2.21]$$

where D_0 and D are the initial and final grain diameters, t is annealing time and n and k_1 are constants. It has been found by Sellars and Whiteman (1979) that the k_1 value can be expressed by an Arrhenius-type equation, thus Equation 2.21 can be written as

$$D^n - D_0^n = k_2 \exp\left(-\frac{Q_{gg}}{RT}\right)t \quad [2.22]$$

where k_2 is a constant and Q_{gg} the activation energy for grain growth. Some empirical equations for grain growth of plain carbon and microalloyed steels are given in Table 2.6.

Table 2.6 Summary of empirical equations describing austenite grain growth (Sellars and Whiteman 1979; Hodgson *et al.*, 1992, Manohar *et al.* 1996)

Steel	Austenite condition	Equation
C-Mn	statically recrystallized	$n=10, k_2=3.87 \times 10^{12}, Q_{gg}=400 \text{ kJ/mol } (T > 1273 \text{ K})$
		$n=10, k_2=5.02 \times 10^{53}, Q_{gg}=914 \text{ kJ/mol } (T < 1273 \text{ K})$
low C-Mn	statically recrystallized	$n=2, k_2=4.27 \times 10^{12}, Q_{gg}=278.4 \text{ kcal/mol}$
0.22C-0.9Mn	statically recrystallized	$n=2, k_2=1.44 \times 10^{12}, Q_{gg}=266.6 \text{ kcal/mol}$
C-Mn and C-Mn-V	statically or metadynamically recrystallized	$n=7, k_2=1.45 \times 10^{27}, Q_{gg}=400 \text{ kJ/mol}$
C-Mn-Ti	statically or metadynamically recrystallized	$n=10, k_2=2.6 \times 10^{28}, Q_{gg}=437 \text{ kJ/mol}$
C-Mn-Nb	statically or metadynamically recrystallized	$n=4.5, k_2=4.1 \times 10^{23}, Q_{gg}=435 \text{ kJ/mol}$

(B) Physical Modeling of Grain Growth

The driving pressure (P_d) for motion of a spherically curved element of grain boundary is given by (Anderson and Grong, 1995)

$$P_d = \frac{2\gamma_{gb}}{\lambda} \quad [2.23]$$

where γ_{gb} is the grain boundary energy and λ the radius of surface curvature. Since λ can not be easily determined, it is usually replaced by a measurable size such as mean grain diameter D . Typically $\lambda=3D$ is used for calculation (Patterson and Liu, 1992; Anderson and Grong, 1995). In practice, the numerical constant in Equation 2.23 can vary by at least a factor of 3. Consequently, in the general cases the driving force pressure is given by: $P_d=k_d\gamma_{gb}/r$.

The effect of precipitate pinning on grain growth was first proposed by Zener (Manohar *et al.*, 1998). The Zener pinning pressure (P_z) is given by

$$P_z = \frac{3}{4} \frac{\gamma_{gb} f_v}{r} \quad [2.24]$$

It has been assumed that all the precipitates are of the same size. Again, considering the uncertainty of the numerical constant, Equation 2.24 changes into $P_z=k_p\gamma_{gb}f_v/r$. The critical (or limiting) grain radius (R_c) is obtained when $P_z=P_d$, which gives the well-known Zener equation:

$$R_c = k_z \frac{r}{f_v} \quad [2.25]$$

where k_z is a constant ($k_z=k_p/k_d$). Although Zener pinning has been recognized for more than fifty years, some arguments still remain on the k_z value (Manohar *et al.*, 1998). In the original Zener model k_z was set to 4/3. Hellman and Hillert (1975) proposed two

values: $4/9$ for normal grain growth and $2/3$ for abnormal grain growth. Manohar *et al.* (1998) summarized the experimental data from different alloy systems and found that the k_Z value falls close to 0.17 for $f_v < 0.05$. Gladman *et al.* (1997) considered the k_Z value as a function of grain size distribution. In this case, $k_Z = \pi/6(3/2 - 2/Z_g)$ where Z_g is the ratio of diameters of the growing and pinning grains. Based on this approach, the k_Z from Hillert corresponds to $Z_g = 3$ for normal grain growth, while that from Manohar to $Z_g = 1.7$. With different assumptions, the R_c values may vary by one order of magnitude.

Several assumptions have been incorporated in the Zener equation, including uniform precipitate size, randomly distributed incoherent precipitates, spherical grains and precipitates. Most of the assumptions have been modified by the following researchers for more realistic situations, which has been reviewed by Nes *et al.* (1985) and Manohar *et al.* (1998). However, little attention has been paid to the effect of precipitate size distributions on the Zener pinning. Fullman introduced a "dirt factor I" to describe the total pinning pressure from a distribution of precipitates (Manohar, 1998):

$$P_p = \frac{3\gamma_{gb} I}{4} \quad [2.26]$$

where $I = \sum f_v(r)/r$ and $f_v(r)$ is the volume fraction of monosized spherical precipitates of radius r . This equation has been rarely used since $f_v(r)$ is not readily determined. Therefore, the effect of precipitate size distributions on Zener pinning still remains unknown. Under this situation, the mean precipitate size is usually used to estimate the precipitate pinning pressure.

The effect of solute drag on grain growth can be described by the simplified approach given by Hu and Rath (1969, 1970). The grain boundary migration rate (v) is related to the effective driving pressure (ΔP_G) and the exponent (n) through the following equation:

$$v = dR / dt = M_{gb} \cdot \Delta P_G^{n-1} \quad [2.27]$$

where M_{gb} is grain boundary mobility. $M_{gb} = M_0 \exp(-Q_{gb}/RT)$. The grain boundary migration rate (v) becomes proportional to the effective driving force (ΔP_g) when $n = 2$. This corresponds to the limiting case where the grain boundary will break away from the surrounding impurity atmosphere. In most cases, however, the observed exponent, n , will be larger than the theoretical value because of the solute drag.

In alloys containing precipitates, ΔP_G is defined as the difference between P_U and P_z . By substituting the expressions of P_G and P_z into Equation 2.27 we have (Anderson and Grong, 1995)

$$v = M_{gb} (k_g \gamma_{gb})^{n-1} \left[\frac{1}{D} - \frac{f_v}{k_z r} \right]^{n-1} \quad [2.28]$$

Then we have the following equation for grain growth with solute drag and precipitate pinning:

$$\frac{dD}{dt} = M' \exp\left(-\frac{Q_{gb}}{RT}\right) \left(\frac{1}{D} - \frac{f_v}{k_z r}\right)^{n-1} \quad [2.29]$$

where $M' = 2M_{gb}(k_g \gamma_{gb})^{n-1}$. M' and k_z are considered as physical constants which reflect grain boundary mobility and pinning efficiency of the precipitates, respectively. Equation 2.29 can be integrated to give the mean grain size as a function of time:

$$\int_{D_0}^D \frac{dD}{(1/D - 1/D_c)^{n-1}} = M_0' \int_{t_0}^t \exp\left(-\frac{Q_{gb}}{RT}\right) dt \quad [2.30]$$

where D_c is critical grain diameter ($D_c = 2R_c$).

The right-hand side of Equation 2.30 represents the effect of thermal cycle with respect to grain growth, which can be determined by numerical methods when the T-t

cycle is known. The effect of precipitates on grain growth is reflected by D_c .

2.4 Recrystallization

(A) Avrami Kinetics

A theoretical treatment of recrystallization kinetics during hot deformation is very difficult. Most of the existing models have been established on the phase transformation theories proposed by Johnson and Mehl (1938), and Avrami (1939 and 1940). For recrystallization, it is assumed that: (1) the recrystallized grain size (R_r) is proportional to time (t) after incubation (τ):

$$R_r = \dot{G} (t - \tau) \quad [2.31]$$

where \dot{G} is growth rate. It is assumed that \dot{G} does not change with time; and (2) the nucleation rate in the non-recrystallized areas decreases exponentially with time. Then the volume fraction of recrystallization (f_r) may be expressed as (Avrami equation):

$$f_r = 1 - \exp(-Bt^{k_A}) \quad [2.32]$$

where B and k_A are constants. In practice, a normalized form of the Avrami equation has been widely used:

$$f_r = 1 - \exp\left\{\ln(1 - X)\left(\frac{t}{t_r}\right)^{k_A}\right\} \quad [2.33]$$

where X can be used as 0.5 for half recrystallization time ($t_{0.5}$), or 0.05 for recrystallization-start time ($t_{0.05}$) or 0.95 for recrystallization-finish time ($t_{0.95}$).

Extensive work has been done to determine the relationship between t_r and TMP parameters (Sellars, 1979 and 1986; Hansen *et al.* 1980; Yamamoto *et al.*, 1984; Andrade *et al.*, 1983; Akben and Jonas, 1984; Kwon and DeArdo, 1986; Choquet *et al.*, 1987;

Campbell *et al.*, 1988; Kwon *et al.*, 1990; Penalba and Carsi, 1995; Medina *et al.*, 1991-1999; Carsi *et al.*, 1996; Cruz-Rivera *et al.*, 1996; Kuziak and Cheng, 1996; Cabrera *et al.*, 1997; Lee, 1999). It is found that the empirical equation proposed by Sellars and Whiteman (1979) has been widely adopted by the following researchers for this relationship:

$$t_x = k_4 (\epsilon - \epsilon_0)^{p'} \dot{\epsilon}^{q'} d_0^{r'} \exp \frac{Q_x}{RT} \quad [2.34]$$

where ϵ is true strain, $\dot{\epsilon}$ strain rate and T the absolute temperature. Q_x is the activation energy for static recrystallization. d_0 is the initial grain size. k_4 , p' , q' , r' are constants.

Table 2.7 gives some of the empirical equations for static recrystallization kinetics of C-Mn steels. It is found that k_A is 2 in most cases, and the form of Equation 2.34 has been adopted by other researchers with minor modifications.

Table 2.7 Static recrystallization kinetics for plain carbon steels.

(1) Sellars and Whiteman (1979): $f_x = 1 - \exp\{\ln 0.5 \times (\frac{t}{t_{0.5}})^2\}$, $t_{0.5} = 2.5 \times 10^{-19} \epsilon^{-4} D_0^2 \exp(\frac{300000}{RT})$
(2) Senuma and Yada (1986): $f_x = 1 - \exp\{\ln 0.5 \times (\frac{t-t_0}{t_{0.5}})^2\}$, $t_{0.5} = 2.2 \times 10^{-12} S_v^{-0.5} \dot{\epsilon}^{-2} \epsilon^{-2} \exp(\frac{300000}{RT})$.
$S_v = \frac{24}{\pi D_0} \{0.491 \exp(\epsilon) + 0.155 \exp(-\epsilon) + 0.1433 \exp(-3\epsilon)\}$
(3) Kwon <i>et al.</i> (1990): $f_x = 1 - \exp\{\ln 0.5 \times (\frac{t}{t_{0.5}})^2\}$.
$t_{0.5} = 3.32 \times 10^{-15} D_0^{1.4145} \epsilon^{-3} Z^{-0.121} \exp(-\frac{285000}{RT})$
(4) Roberts <i>et al.</i> (1983): $f_x = 1 - \exp\{\ln 0.5 \times (\frac{t}{t_{0.5}})^2\}$, $t_{0.5} = 5 \times 10^{-21} \epsilon^{-4} D_0^2 \exp(\frac{330000}{RT})$
(5) Hodgson and Gibbs (1990): $f_x = 1 - \exp\{\ln 0.5 \times (\frac{t}{t_{0.5}})^{1.5}\}$, $t_{0.5} = 0.53 \times 10^{-5} Z^{-0.8} \exp(\frac{240000}{RT})$

(B) Recrystallization Kinetics of Microalloyed Steels

For microalloyed steels, recrystallization is retarded by solute drag and precipitate pinning. It has been found that the sigmoidal Avrami equation is valid until strain-induced precipitation occurs (Medina *et al.*, 1991-1999). The effect of solute drag on recrystallization is reflected by the decreased Avrami constant and increased activation energy. Some of the empirical equations for microalloyed steels are given in Table 2.8.

Recrystallization kinetics changes not only with the type of microalloy elements, but also with their concentration in solution. Considering this, Medina and Fabregue (1991) suggested that this effect be reflected by the change of recrystallization activation energy:

$$Q_r = 83600 + 978000 \frac{([Mn] + [Si])^{0.537}}{C^{1.269}} + 1729[Mo]^{0.704} + 0.05[Ti]^{3.663} + 260[Nb]^{1.256} \quad [2.35]$$

where the alloy contents are in wt% $\times 10^3$. The effect of vanadium is not included in this equation, because its effect is small. Similar results have been given by Choquet *et al.* (1987).

Another method to model recrystallization kinetics of microalloyed steels is to compare their recrystallization-start times with that of plain carbon steels (Sellars *et al.*, 1986). The recrystallization-start time of C-Mn steels ($\tau_{0.05}^{C-Mn}$) was used as standard. The solute drag effect of microalloy elements is assumed to be exponentially proportional to the alloy content in solution. Then

$$\tau_{0.05} = \tau_{0.05}^{C-Mn} \exp\left\{\frac{[X]F_s}{RT}\right\} \quad [2.36]$$

where F_s the solute drag per wt% of solute $[X]$. It is a function of temperature and can be modeled as:

Table 2.8 Static recrystallization kinetics for microalloyed steels.

Nb steel

(1) **Sellars and Whiteman (1979)**: $f_v = 1 - \exp\left\{\ln 0.95 \times \left(\frac{t}{t_{0.05}}\right)^2\right\}$,

$$t_{0.05} = 6.75 \times 10^{-20} D_0^2 \varepsilon^{-4} \exp\left(\frac{300000}{RT}\right) \exp\left\{\left(\frac{275000}{RT} - 185\right)[\text{Nb}]\right\}$$

(2) **Kwon et al. (1990)**: $f_v = 1 - \exp\left\{\ln 0.95 \times \left(\frac{t}{t_{0.05}}\right)^2\right\}$;

$$t_{0.05} = 6.75 \times 10^{-8} D_0^2 \varepsilon^{-4} \exp\left(\frac{300000}{RT}\right) \exp\left\{\left(\frac{275000}{RT} - 185\right)[\text{Nb}]\right\}$$

(3) **Lee (1999)**: $f_v = 1 - \exp\left\{\ln 0.95 \times \left(\frac{t}{t_{0.05}}\right)^2\right\}$;

$$t_{0.05} = t_{0.05}^{C-Mn} \exp\left\{\left(\frac{2.27 \times 10^5}{T} - 185\right)[\text{Nb}]\right\} \exp\left\{\frac{(\text{Nb})_p}{r_p} \left(\frac{1.534 \times 10^7}{T} - \frac{2.063 \times 10^5}{r_p}\right)\right\} \\ \times \exp\left\{\left(\frac{1.534 \times 10^7}{T} - \frac{2.063 \times 10^5}{r}\right) \frac{[\text{NbC}]}{r}\right\}$$

(4) **Medina et al. (1994)**: $\text{SRCT}(K) = 1326.5 - 178.3 \ln(1 + \varepsilon)$; $f_v = 1 - \exp\left\{\ln 0.5 \times \left(\frac{t}{t_{0.5}}\right)^{k_v}\right\}$,

$$k_v = 27.35 \exp\left(-\frac{40000}{RT}\right), \quad t_{0.5} = 3.943 \times 10^{-13} \varepsilon^{-1.96} \varepsilon^{-0.44} D_0 \exp\left(\frac{262000}{RT}\right) \quad (\text{when } T > \text{SRCT});$$

$$Q_v = 9.815 \times 10^{-6} \varepsilon^{-4} d_0^{1.9} \exp\left(\frac{1500000}{RT}\right) \quad (\text{when } T < \text{SRCT})$$

V steel

(1) **Kuziak et al. (1996)**: $f_v = 1 - \exp\left\{\ln 0.5 \times \left(\frac{t}{t_{0.5}}\right)^{0.95}\right\}$, $t_{0.5} = 9.3 \times 10^{-16} \varepsilon^{-4} D_0^2 \exp\left(\frac{23000}{RT}\right)$

(2) **Medina et al. (1994)**: $\text{SRCT}(K) = 1310 - 373.6 \ln(1 + \varepsilon)$, $f_v = 1 - \exp\left\{\ln 0.5 \times \left(\frac{t}{t_{0.5}}\right)^{k_v}\right\}$,

$$k_v = 4.33 \exp\left(-\frac{17000}{RT}\right), \quad t_{0.5} = 3.103 \times 10^{-11} \varepsilon^{-1.92} \varepsilon^{-0.44} D_0 \exp\left(\frac{198000}{RT}\right) \quad (\text{when } T > \text{SRCT});$$

$$Q_v = 3.052 \times 10^{-12} \varepsilon^{-4} d_0^{1.9} \exp\left(\frac{700000}{RT}\right) \quad (\text{when } T < \text{SRCT})$$

[‡] static recrystallization critical temperature.

Table 2.8 Static recrystallization kinetics for microalloyed steels (continued).

Ti steel

$$\text{Medina et al. (1994): SRCT(K)} = 1263 - 220.7 \ln(1 + \epsilon), \quad f_x = 1 - \exp\left\{\ln 0.5 \times \left(\frac{t}{t_{0.5}}\right)^{k_x}\right\},$$

$$k_x = 4.81 \exp\left(-\frac{20000}{RT}\right), \quad t_{0.5} = 3.702 \times 10^{-12} \epsilon^{-2.15} \dot{\epsilon}^{-0.44} D_0 \exp\left(\frac{227000}{RT}\right) \quad (\text{when } T > \text{SRCT});$$

$$Q_x = 3.145 \times 10^{-35} \epsilon^{-2.9} D_0^{1.9} \exp\left(\frac{800000}{RT}\right) \quad (\text{when } T < \text{SRCT})$$

Ti-V steel

$$\text{Roberts et al. (1983): } f_x = 1 - \exp\left\{\ln 0.5 \times \left(\frac{t}{t_{0.5}}\right)^2\right\}, \quad t_{0.5} = 5 \times 10^{-21} (\epsilon - 0.058)^{-1.5} D_0^2 \exp\left(\frac{280000}{RT}\right)$$

HSLA steel

$$\text{Choquet et al. (1987): } f_x = 1 - \exp\left\{\ln 0.5 \times \left(\frac{t}{t_{0.5}}\right)^2\right\}, \quad t_{0.5} = v_R \epsilon^P \epsilon^{-0.28} D_7^{0.878} \exp\left(\frac{Q_{\text{rex}}}{RT}\right)$$

$$\frac{Q_r}{R} = 39660 - 6025.8[C]^{0.4} + 755[C]^{0.65} + 2.848 \times 10^{-3}[\text{Mn}]^2 + 4423[\text{Mo}]^{0.2}$$

$$+ \{466.45 + 5.57 \times 10^5 (T_c - T)^4\} [\text{Nb}]^{0.68};$$

$$P = D_7^{-0.115} [-3.89 + f_p(\text{Nb})]; \quad v_R = f_R(\text{C, Mn, Mo, Nb})$$

$$F_x = p'' - q'' \times T \quad [2.37]$$

where p'' and q'' are constants. Equation 2.36 can then be rewritten as:

$$t_{0.05} = t_{0.05}^{\text{C-Mn}} \exp\left\{[X] \left(\frac{p_1}{T} - q_1\right)\right\} \quad [2.38]$$

where p_1 and q_1 are constants. Both the effects of temperature and microalloy elements are included in this equation, and its simple form makes it easy to be extended for more complex situations.

The recrystallization behavior becomes very complex if strain-induced precipitation is taken into account. It is found that recrystallization activation energy remains nearly constant until strain-induced precipitation occurs, but rapidly increases when temperature

is lower (Medina *et al.*, 1994). The increased activation energy is attributed to strain-induced precipitation. Medina *et al.* (1994-1999) have modeled the value of Q_x for different microalloyed steels when temperatures are below the SRCT.

Equation 2.38 has been extended to incorporate the effect of precipitate pinning on recrystallization kinetics (Kwon *et al.*, 1992 and Lee, 1999). It was further assumed that precipitate pinning on recrystallization-start time might be expressed as an exponential function. Then we have:

$$t_{0.05} = t_{0.05}^{C-Mn} \exp\left\{[X]\left(\frac{P_2}{T} - q_2\right)\right\} \exp\left(\frac{f_{vp} F_p}{RT}\right) \quad [2.39]$$

where f_{vp} is the volume fraction of precipitates. F_p is pinning force per volume. With this assumption, the kinetics of recrystallization with strain-induced precipitation has been modeled.

2.5 Strain-induced Precipitation

Dutta and Sellars (1987) first proposed an empirical equation for the kinetics of strain-induced Nb(C,N) precipitation. It was found that precipitation-start time could be described as a function of deformation temperature, strain and strain rate, and Nb concentration. Liu and Jonas (1988) derived a similar equation for Ti(C,N) precipitation. More generic models have been given by Saito *et al.* (1988), Militzer *et al.* (1992), Okaguchi and Hashimoto (1992), and Park and Jonas (1992) to predict precipitation-start time. All these studies are based on the classic nucleation theory established by Aaronson and Lee (1979).

(A) Chemical Driving Force

The decreased solubility during cooling provides the chemical driving force for precipitation, which can be described as a function of supersaturation (eg. TiC):

$$\Delta G_{\text{chem}} = -\frac{RT}{2V_m} \left(\ln \frac{X_{\text{Ti}}^e}{X_{\text{Ti}}^0} + \ln \frac{X_{\text{C}}^e}{X_{\text{C}}^0} \right) \quad [2.40]$$

where X_i^e and X_i^0 are the equilibrium concentrations of element i at the lower temperature and the solution temperature, respectively. V_m is the molar volume of the precipitate. For multi-component carbonitrides like Ti(C,N), the chemical driving force is given by (Liu and Jonas, 1988)

$$\Delta G_{\text{chem}} = -\frac{RT}{2V_m} \left\{ \ln \frac{X_{\text{Ti}}^e}{X_{\text{Ti}}^0} + y \ln \frac{X_{\text{C}}^e}{X_{\text{C}}^0} + (1-y) \ln \frac{X_{\text{N}}^e}{X_{\text{N}}^0} \right\} \quad [2.41]$$

The V_m value of Ti(C,N) can be calculated by:

$$V_m = \frac{N_0 a_p^3}{8} \quad [2.42]$$

where N_0 is Avogadro's constant. a_p is the lattice parameter of Ti(C,N), which varies with the composition of the nucleus. To reflect this variation, it is assumed that the lattice parameter of the carbonitride is proportional to the mole fraction of binary compounds according to law of mixtures; that is:

$$a_p = y a_{\text{TiC}} + (1-x) a_{\text{TiN}} \quad [2.43]$$

where a_{TiC} and a_{TiN} are the lattice parameters of TiC and TiN, respectively. Their values are given in Table 2.3.

(B) Critical Free Energy for Nucleation

The free energy change accompanying the formation of a nucleus (ΔG_n) on a dislocation can be written as (Dutta and Sellars, 1987):

$$\Delta G_n = V\Delta G_{\text{chem}} + \Delta G_e + S\xi\gamma \quad [2.44]$$

where ΔG_e is the elastic energy change by formation of nucleus. V and S are the volume and surface area of the nucleus. ξ is a modifier of interfacial energy with a value between 0 and 1, associated with the presence of dislocations.

For dislocation nucleation, the ΔG_e for a nucleus of radius r can be described by (Okaguchi and Hashimoto, 1992):

$$\Delta G_e = -\frac{\mu b^2 r}{2\pi} \ln \frac{2r}{r_d} - \frac{\mu b^2 r}{5} \quad [2.45]$$

where μ and b are the shear modulus and Burgers vector, respectively, for austenite. r_d is the radius of the dislocation core. Therefore, the free energy change for a spherical nucleus can be given by:

$$\Delta G_n = \frac{4}{3}\pi r^3 \Delta G_{\text{chem}} - \mu b^2 r \left(\frac{1}{2\pi} \ln \frac{2r}{r_d} + \frac{1}{5} \right) + 4\pi r^2 \gamma \quad [2.46]$$

It has been found that the shear modulus μ of austenite is a function of temperature, which can be written as (Militzer *et al.*, 1992):

$$\mu = 0.35[12.6 - 0.007(T - 1013)] \times 10^{10} \text{Pa} \quad [2.47]$$

Figure 2.2 shows the free energy change with precipitate radius of Nb(C,N) in 154Inb. It is found that both the critical energy and the critical nucleus radius are significantly reduced by dislocation nucleation.

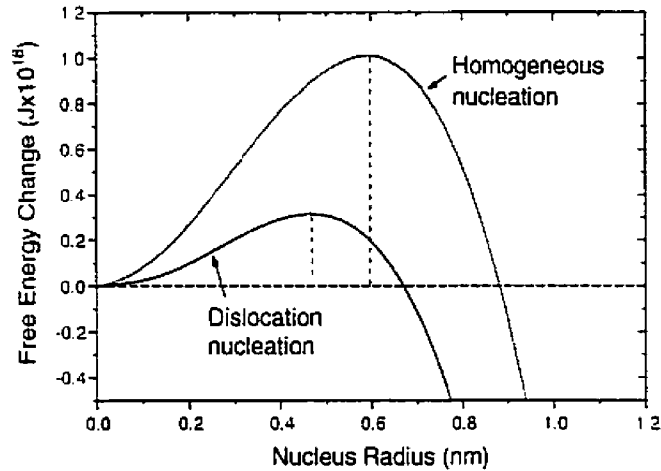


Figure 2.2 Free energy change with precipitate radius (1541Nb). The related constants were selected as $b=2.5 \times 10^{-10} \text{m}$ and $r_d=2 \times 10^{-10} \text{m}$.

(C) Nucleation Rate

The nucleation rate per unit volume (\dot{N}) is given by (Dutta and Sellars, 1987):

$$\dot{N} = Z\beta' N \exp\left(-\frac{\Delta G_n^*}{k_B T}\right) \quad [2.48]$$

where Z is the Zeldovich non-equilibrium factor. β' is the rate at which atoms are added to the critical nucleus. N is the number of nucleation sites per unit volume. ΔG_n^* is the critical free energy for nucleation. k_B is Boltzmann's constant.

For dislocation nucleation, the density of nucleation sites can be estimated from (Militzer *et al.*, 1992):

$$N = \frac{\rho_d}{a_\gamma} \quad [2.49]$$

where ρ_d is the dislocation density and a_γ lattice parameter of the austenite. The

dislocation density can be estimated by the following equation (Hansen *et al.*, 1980; Dutta *et al.* 1992):

$$\rho_d = \left(\frac{\sigma}{b\mu}\right)^2 \quad [2.50]$$

where σ is deformation stress which can be measured by experiment. It has found that the product of Z and β^* can be approximated as (Liu and Jonas, 1988):

$$Z\beta^* = \frac{D_m X}{a_1^2} \quad [2.51]$$

Considering that the segregation of microalloy elements along dislocation lines only accounts for a small amount of the bulk content, the pipe diffusion only has some effect on the nucleation rate at the very beginning. The following nucleation rate is still controlled by bulk diffusion. The bulk diffusivity is thus used for nucleation kinetics. Also considering that diffusivity is a function of temperature, the nucleation rate can be expressed as :

$$\dot{N} = \frac{\rho_d D_m^0 X}{a_1^2} \exp\left(-\frac{\Delta G_n^*}{k_B T}\right) \exp\left(-\frac{Q_d}{RT}\right) \quad [2.52]$$

(D) Precipitation-Start Time

For a small amount of precipitation, it is assumed that the nucleation rate is constant. Thus, the Johnson-Mehl equation is used to describe precipitation kinetics (Okaguchi and Hashimoto, 1992):

$$f_v = 1 - \exp\left\{-\frac{4\pi}{3} \int_0^t \dot{N} (2k_s D_m)^3 (t - \tau)^{\frac{3}{2}} d\tau\right\} \quad [2.53]$$

By setting the amount of 5% precipitation as precipitation-start time ($t_{0.05}^p$), its value can

be determined.

2.6 Summary

The mechanisms of microstructural evolution during TMP of microalloyed steels have been briefly reviewed, and different models have been described for each of the metallurgical processes. To develop a methodology for modeling microstructural evolution during the complex forging process, the following approaches have been selected: Grain growth is described as curvature-driven, diffusion-controlled, and limited by the Zener pinning mechanism; The stability of carbonitride precipitates is determined by their solubility products; The dissolution, growth and coarsening of carbonitrides are considered as diffusion-controlled processes; The nucleation of precipitates is modeled by classic nucleation theory; Recrystallization kinetics is modeled by fitting to the Avrami equation.

Chapter 3. Experimental

3.1 Experimental Materials

Four medium-carbon steels have been used for the experiments: 1541Nb, 1541VTi, 1541Al and 1141Nb. The compositions are given in Table 3.1. These steels are based on 0.41C-1.5Mn (wt%), with the addition of different microalloy elements. 1541VTi and 1141Nb are resulfurized for improved machinability.

Table 3.1 Chemical Compositions of the Experimental Steels (wt%)

Name	C	Mn	Si	P	S	Al	N	Microalloy Elements
1541Al	0.40	1.48	0.26	0.018	0.026	0.023	0.006	--
1541Nb	0.41	1.67	0.24	0.022	0.013	0.002	0.0053	Nb:0.036
1541VTi	0.40	1.49	0.56	0.016	0.042	0.004	0.009	V:0.11, Ti:0.014
1141Nb	0.39	1.51	0.19	0.012	0.12	0.001	0.0054	Nb:0.046

The steels were received as hot-rolled commercial bars. The bar size was 51mm diameter (2 in.) for all the steels except 1141Nb, whose diameter was 102mm (4 in.). Cylindrical samples were machined with their axis parallel to the rolling direction of the bar. All samples were taken from equivalent positions around the axis of the bar, as shown in Figure 3.1, to minimize the effect of segregation.

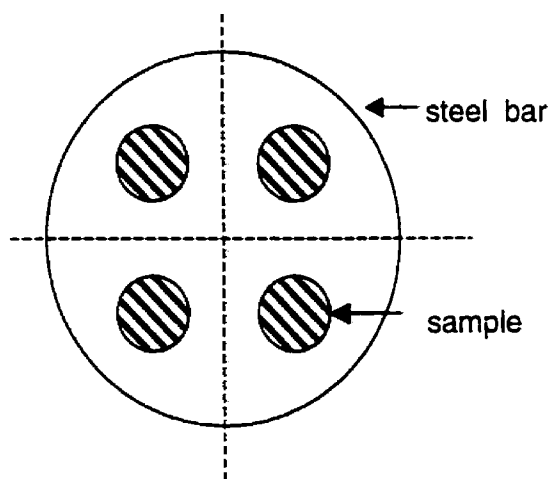


Figure 3.1 Schematic shows the sample location from the steel bar.

3.2 Experimental Procedures

Three experimental investigations were carried out to study microstructural evolution during TMP: (1) Grain growth and precipitate evolution during induction heating; (2) the effects of initial microstructure on grain growth during induction reheat; and (3) Recrystallization following hot deformation.

(A) Grain growth and precipitate evolution during induction heating

Three steels were studied in this experiment: 1541Nb, 1541VTi and 1541Al. Cylindrical samples (6 mm diameter \times 10 mm length) were used for this study.

An industrial induction heating cycle from TRW was used for this experiment, as is shown in Figure 3.2. Each steel bar was induction heated at 21°C/s from room temperature to 870°C , and then at 10°C/s to a specific temperature between $1200\text{--}1250^\circ\text{C}$. The steel bar is held at this temperature for about 6 seconds, followed by forging operations. The forged part is then cooled down by air-cooling. It only takes about 75 seconds to reach the maximum reheat temperature.

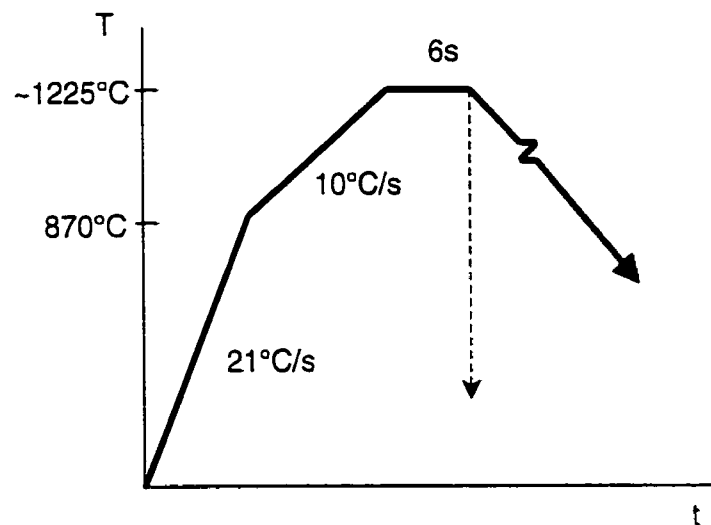


Figure 3.2 TRW induction heating cycle.

The simulated procedures are shown in Figure 3.2 by the dashed lines. The samples were quenched immediately after reheat for microstructure observations. A group of heating temperatures between 900-1250°C and holding times between 0-60 seconds were used to determine the effect of temperature and holding time on grain growth and precipitate evolution.

Induction heating simulations were carried out with a quench-deformation dilatometer made by Materials Measuring Corporation. Figure 3.3 shows a schematic of the dilatometer. This instrument provides a programmed temperature, time and strain control, and a high vacuum environment (10^{-6} torr). Therefore, it can be used to perform various thermomechanical simulations. Cylindrical samples are held between two quartz platens and are heated by an induction coil. The temperature is monitored by Pt/Pt -10%Rh thermocouples welded to the sample surface. The accuracy of the temperature control is $\pm 3^\circ\text{C}$. Two quartz rods, one extending to each platen, are connected to a sensitive linear variable differential transformer (LVDT). As the sample expands or contracts upon heating, cooling or phase transformation, the relative displacement of the quartz rods produces a voltage by the LVDT which is proportional to the dilation.

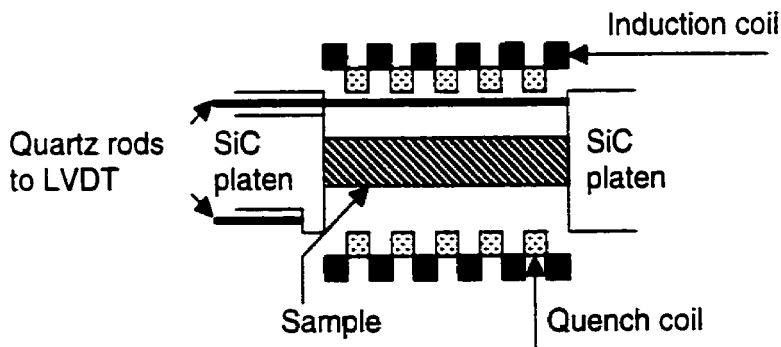


Figure 3.3 Schematic of quench-deformation dilatometer.

(B) Effect of Initial Microstructure on Grain Growth During Induction Reheat

A heating cycle from Welland Forge was used for this test, as is shown in Figure 3.4. Compared with the heating cycle from TRW, the Welland Forge cycle has slower heating rate and longer holding time. It takes about 225 seconds to reach the maximum reheat temperature. 1141Nb was used for this experiment. The samples are cylindrical with 6 mm diameter and 10 mm length.

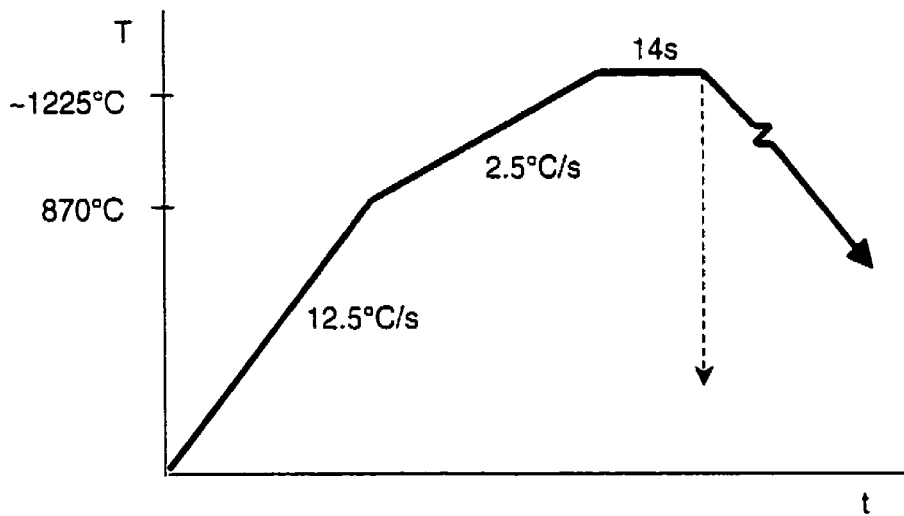


Figure 3.4 Welland Forge induction heating cycle.

Four different initial microstructures were produced by preheat treatments based on the Welland Forge heating cycle. The preheat treatments are shown in Figure 3.5. The 1250AC samples were heated to 1250°C, and held for 14 seconds. Then these samples were cooled at 1.7°C/s to 750°C, followed by cooling at 0.5°C/s to room temperature. 1250Q had the same heating and holding schedules as 1250AC except that the samples were quenched immediately after 14s holding at 1250°C. 900AC simulated a normalizing treatment, with a heating temperature of 900°C.

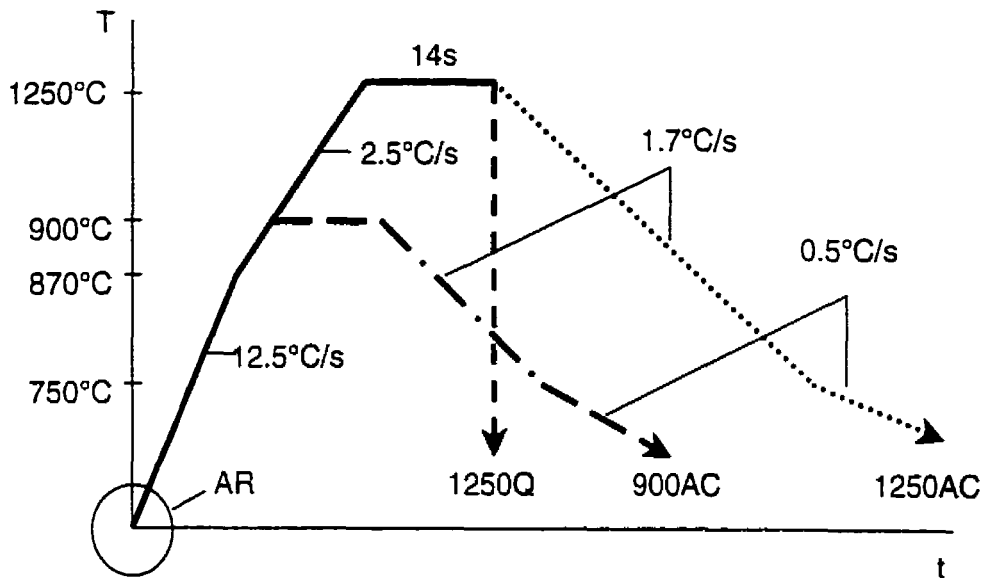


Figure 3.5 Preheat treatments to produce four different initial microstructures. AR—as hot-rolled condition; 1250AC—AR +1250°C preheat + air-cool (0.5°C/s); 1250Q—AR+1250°C preheat + water-quench (130°C/s); 900AC—AR + 900°C preheat + air-cool (0.5°C/s).

Samples representing each of the preheated treatments were reheated following the Welland Forge cycle to a specific temperature between 900 and 1250°C, held for 14 seconds and quenched to study the austenite grain sizes and precipitate evolution.

(C) Recrystallization Following Hot Deformation

Two steels have been used: 1541Nb and 1541VTi. The samples were cylindrical with 8.6 mm diameter and 11.6 mm length.

Recrystallization behavior was studied by the double-hit recrystallization test. The test procedure is illustrated in Figure 3.6. A sample was heated at -1°C/s from 900°C to a specified temperature, held for 180 seconds, then air-cooled at -1°C/s to a specified deformation temperature. The sample was held at this temperature for -1 minute to get

uniform temperature distribution. Double compressions were performed on this sample, with an interruption between the two deformations. Load-deflection values were recorded during the two deformations and converted to stress-strain curves. Different interruption times were used for different samples to obtain different softening fractions.

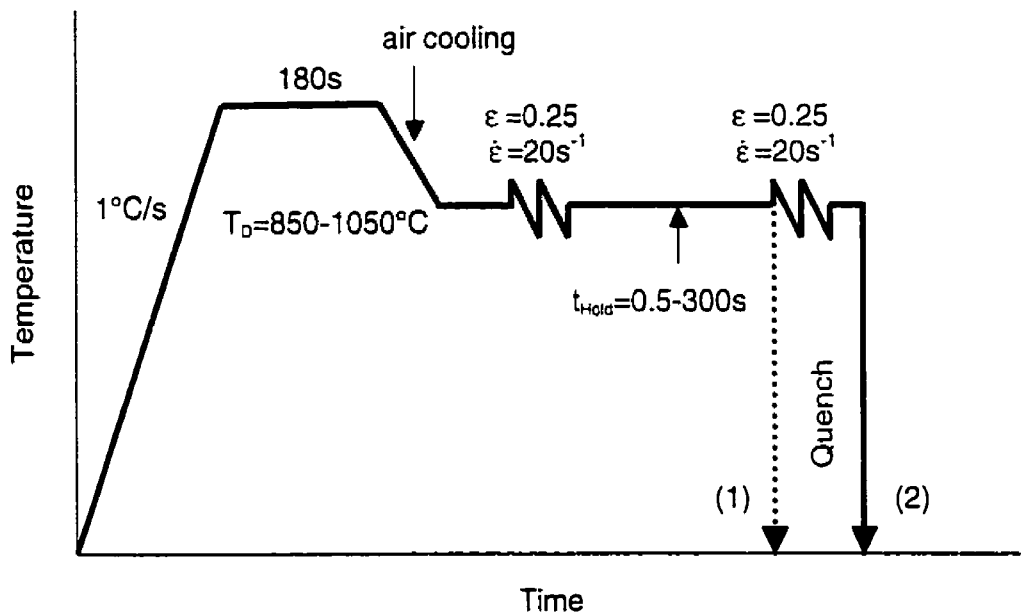


Figure 3.6 Test procedures for double-hit (2) and single-hit (1) experiments.

Some samples were quenched immediately after the first deformation and hold to determine recrystallization fraction by metallography. A strain of 0.25 and a strain rate of 20s^{-1} were applied in all the tests. Different heating temperatures were selected for different steels to obtain the same initial austenite grain size. These were 1200°C for 154INb and 1260°C for 154IVTi, respectively.

Double-hit recrystallization tests were carried out on a cam plastometer at CANMET. Figure 3.7 shows the schematic of the cam plastometer. It is a compression machine used

in studying the hot working behavior of metals. The sample is deformed between two flat dies. The lower die is caused to move upwards and deform the sample by the cam follower riding up the cam lobe. The cam is driven by a motor that maintains a constant speed. A flywheel is used at high speed to store energy for deformation so that speed is not lost during deformation. The sample is heated by an induction coil and cooled by air-cooling. The sample can be picked out for quenching when necessary. The temperature is controlled by a thermocouple welded inside the sample.

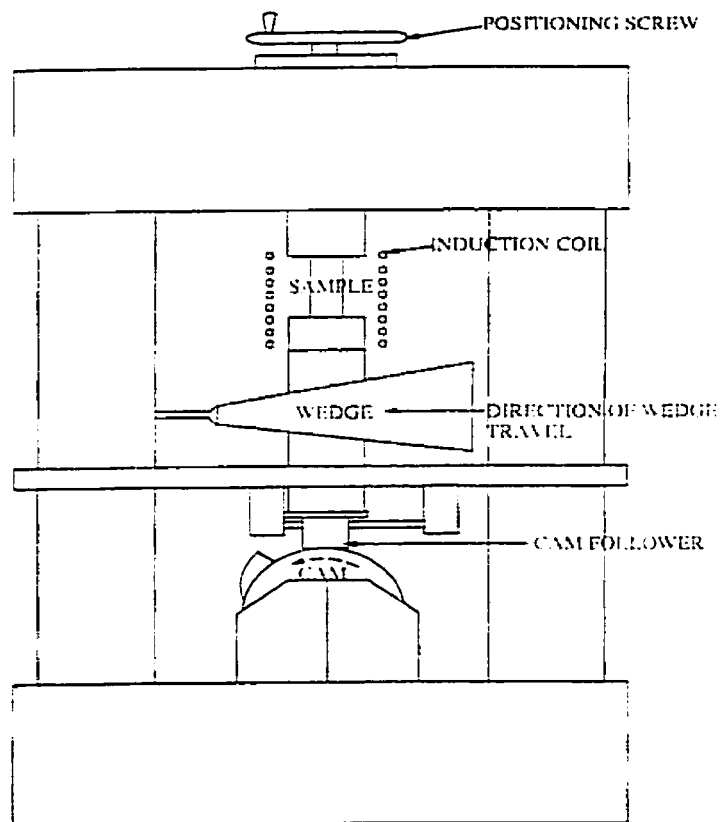


Figure 3.7 Schematic of cam plastometer

Several methods are available for measuring softening fractions from stress-strain curves, such as back extrapolation method, 0.2% offset method, and mean flow stress method (Fernandez *et al.*, 1999). Here the softening fraction was calculated by a method using the areas under stress-strain curves (Baragar, 1999). This method is illustrated in Figure 3.8. The two solid curves oa and bc are the true stress and true strain curves determined from experiments. Lines oe' and be are the linear extensions from elastic deformation. Quadrangles $oe'c'b$ and $becd$ are congruent each other.

If no softening occurred during the interruption time, the second flow curve would be the linear extension of the first flow curve (line ac). If complete recrystallization occurred, the second flow curve would be the same as the first one. Considering the elastic energy (the area of Δabe), the total energy release for a complete recrystallization can be expressed by the area S_1' . For partial recrystallization, the released energy S_2' is only a fraction of the energy for a complete recrystallization. This fraction is considered as

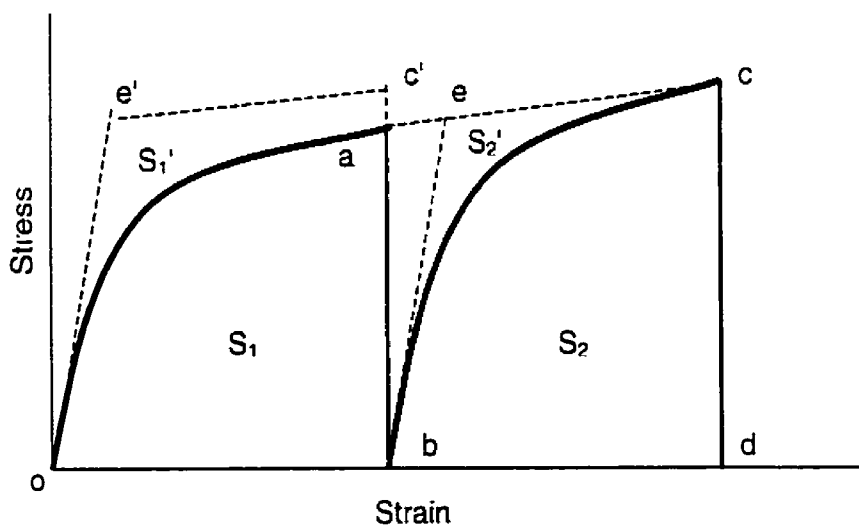


Figure 3.8 Typical stress-strain curves from a double-hit test illustrating the method to determine softening fraction.

softening fraction (f_s). Therefore, it can be given as:

$$f_s = \frac{S_2}{S_1} = \frac{(S_{abdc} - S_{abc}) - S_2}{(S_{abdc} - S_{abc}) - S_1} \quad [3.1]$$

The area S_{abdc} and S_{abc} can be determined directly from the stress-strain figures. The areas S_1 and S_2 can be calculated from the recorded stress-strain data by numerical integration. The f_s values can thus be obtained. Compared with the methods using stresses, this area method has sound physical meaning and better accuracy.

3.3 Microstructure Characterization

The prepared samples were sectioned longitudinally for microstructural observations. One half of the sample was used for austenite grain size measurement, the other half for precipitate observations.

The samples for austenite grain sizes were etched in a solution of saturated picric acid + wetting agent to reveal the prior austenite grain boundaries (Schacht and Richter, 1998). It has been found that this is a difficult method, especially for medium carbon steels. The following procedures were followed to ensure good etching effect (Figure 3.9):

- (1) The samples are tempered at 510°C for 2 hours to promote segregation along prior austenite grain boundaries.
- (2) The best chemical composition of the etchant seems to be 50 ml saturated picric water solution + 3 drops of wetting agent.
- (3) Make sure the picric acid water solution is saturated. A simple way is to add a little picric acid powder in the solution to make it remain saturated at elevated temperature.
- (4) A piece of cotton is put in the solution to avoid black stain forming at the sample surface.
- (5) Keep the solution temperature at 70-80°C.
- (6) Dip the sample in the solution for 0.5-2 minutes. Rub the

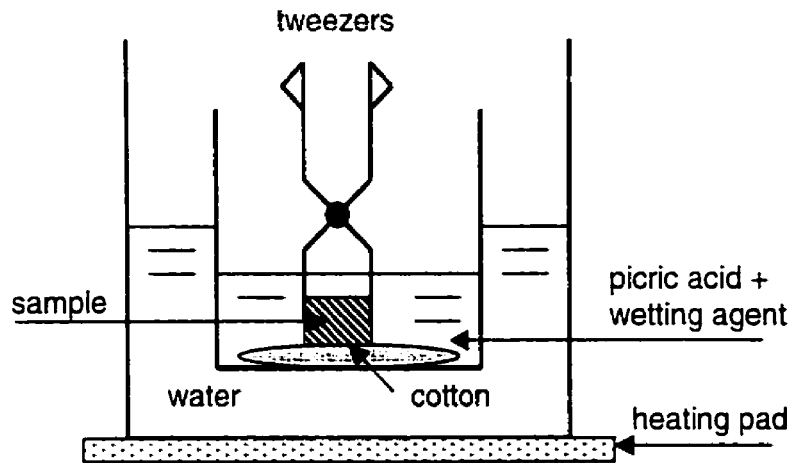


Figure 3.9 Schematic shows the etching apparatus for prior austenite grain boundaries.

sample with the cotton during etching to remove the surface layer. (7) Take the sample out of the solution and rinse with water. (8) Rub the sample slightly on a polishing disc with 0.5μ alumina to remove the surface layer and the microstructure in the grains. (9) Clean the sample with water and remove the water with a heat gun or dryer. (10) For good etching, the surface of the sample should look like silver matte, but still give the contour of an image. (11) Polishing and etching can be repeated to get better effect.

Grain sizes were measured by the linear intercept method according to ASTM E112. A small ruler (or a straight line with a known length) in the eyepiece is overlapped on the microstructure under a microscope. By selecting proper magnification, the number of intercept points between the ruler and the grain boundaries can be readily counted. The intercept distance and the mean grain diameter can thus be determined by referring to the ASTM standard. In order to achieve high accuracy, 150-800 grains were measured for each sample to determine a mean grain diameter, and the observation areas and the angle of the ruler were randomly selected for each count.

For double-hit recrystallization tests, non-uniform deformation can be observed at the

two ends of the sample. These areas were avoided for the microstructure observations. The recrystallization fraction was measured by standard point count method (ASTM E562). A small grid in the eyepiece was overlapped on the microstructure under a microscope. The cross points located in the recrystallized areas (or the non-recrystallized areas if recrystallization is more than 50%) were counted. The volume fraction of the recrystallized areas was then obtained by dividing by the total cross points on the grid. More than 20 areas were randomly selected and measured for each sample to get a average recrystallization fraction.

The samples for precipitate observations were polished and etched with 2% Nital. Carbon film was coated directly on the etched samples with a JOEL J-400 carbon evaporator. A schematic is given in Figure 3.10. The thickness of the coating was controlled by the colour. A piece of white paper, with a piece of glass on it, was put into

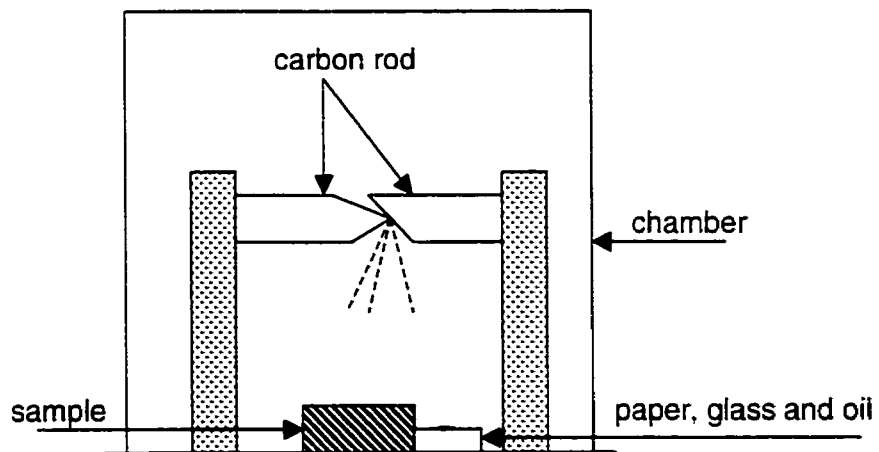


Figure 3.10 Schematic of carbon evaporator.

the chamber close to the samples. A drop of vacuum oil was put on the glass. The carbon deposited on the glass during coating except where it is covered by the oil. The coating

thickness can be estimated by the contrast between the oiled and surrounded areas. The deposition was stopped when the surrounded area becomes dark brown. The coated sample surface looks dark blue.

Carbon replicas were extracted from the samples by chemical etching. For quenched samples, the carbon film can be easily extracted by 10% Nital. The procedures include (Figure 3.11): (1) The carbon film at the centre of the sample was cut into many small pieces, about 2×2 mm square. (2) 10% Nital solution was dropped on the sample surface until some of the carbon films start bubbling. (3) The sample was then turned over (face down) with an angle of $\sim 45^\circ$ and slowly dipped into distilled water. The bubbled carbon replicas were peeled off the sample surface by the surface tension of the water. (4) The floating carbon replicas were collected on copper grids with small tweezers, and cleaned with distilled water several times by passing through water containers. (5) If the replica rolls up and cannot be flattened, it can be put into methanol (or alcohol) first and then back into water. The difference of surface tension between methanol and water will make the replica flat.

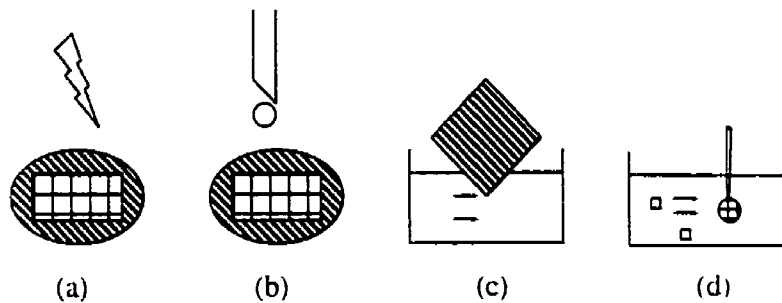


Figure 3.11 Schematic illustrates the basic procedures for preparing carbon replicas. (a) section carbon film; (b) drop 10% Nital on film until bubbling; (c) dip sample into water; (d) collect replicas with copper grid.

For the as-rolled and slowly cooled samples where microstructures were mainly pearlite, the replicas had to be extracted by electro-polishing. The electrolyte was 7% perchloric acid in 2-butoxyethanol (Feng *et al.* 1989), and the electro-polishing conditions were 19V, 0.1-0.2A, 2-5 minutes. The sectioned carbon film was dipped into the electrolyte and etched under current until some carbon replicas peeled off. For better effect, the electrolyte was kept in the freezer (about -20°C) before using and was changed when it became warm during etching.

The replicas were observed in a Philips CM20 electron microscope at 200 kV. Photographs were taken under different magnifications, depending on the sizes of the precipitates. The sample holder was tilted so that maximum precipitates were observed (some of them could not be observed because of their orientations). Precipitate diameters were measured directly on the micrographs (negatives). 200-800 precipitates were measured for each sample to determine a precipitate size distribution.

The composition of precipitates was determined by EDS analysis. In this technique, the electron beam was focused on a precipitate. The X-ray signals from the precipitates were collected by a Si-Li detector and processed by Voyager software. The types of elements (except C, N or lighter) and their amounts in the precipitate were analysed, and the composition of the precipitate was determined. More than 25 precipitates were analysed for each type of precipitate for an average composition.

**Chapter 4. Grain Growth & Precipitate
Evolution During Induction
Reheat**

4.1 Microstructures of As-Rolled Bar

The microstructures of the hot-rolled steel bars are shown in Figure 4.1. They were all composed of primary ferrite and pearlite. Intragranular ferrite was observed in some pearlite colonies. 1541VTi had higher volume fraction of ferrite. Some elongated MnS inclusions were observed in all the steels, but more in 1541VTi because of its high sulfur content.

The precipitates in the as-rolled bars are shown in Figures 4.2. They were found both in primary ferrite and pearlite. The precipitates were not uniformly distributed in the microstructures. Some areas had more precipitates than other areas, and a higher density of precipitates was found in ferrite than pearlite. Very low density of precipitates was observed in 1541Al (Figure 4.2d).

In 1541Nb and 1141Nb, most precipitates were globular. In 1541VTi, most small precipitates (<50nm) were globular, although some rod-like precipitates were also observed, while most large precipitates were cuboidal (Figure 4.2c). Most precipitates were cuboidal in 1541Al (Figure 4.2d).

EDS analyses showed that the precipitates in 1541Nb were Nb-rich, thus these precipitates were considered to be Nb(C,N). Two types of precipitates were observed in 1541VTi: V-rich and Ti-rich. Most small precipitates were V-rich, while most large cuboids were Ti-rich. They were considered to be V-rich and Ti-rich carbonitrides, respectively. The precipitates in 1541Al were Al-rich. Since Al does not form carbides, these precipitates were taken to be AlN. Some large globular MnS inclusions were also observed in the steels. Table 4.1 gives a summary of the precipitate type, shape and distribution in the four steels.

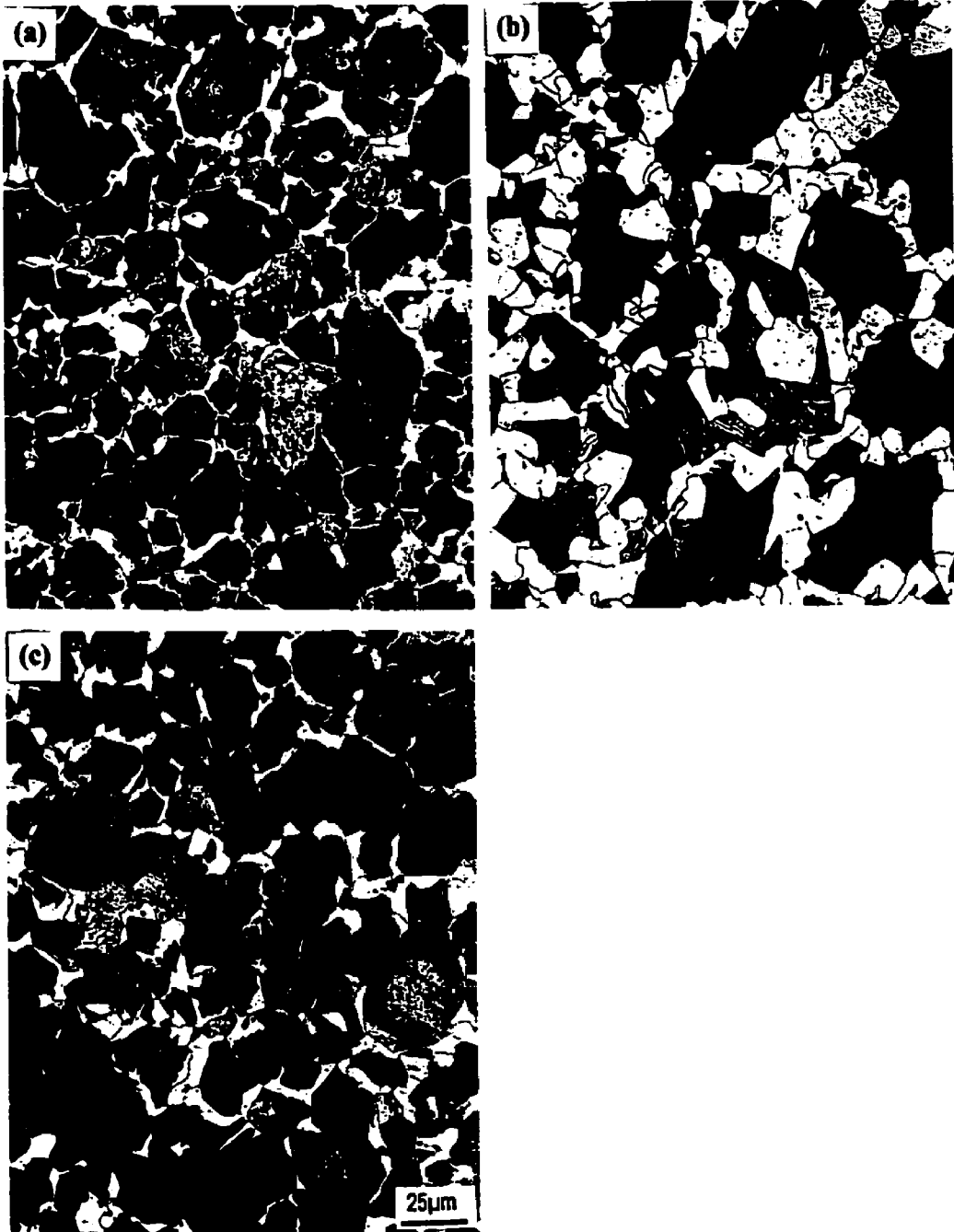


Figure 4.1 The microstructures (pearlite + ferrite) of the as-rolled bar. (a) 1541Nb. (b) 1541VTi
(c) 1541Al

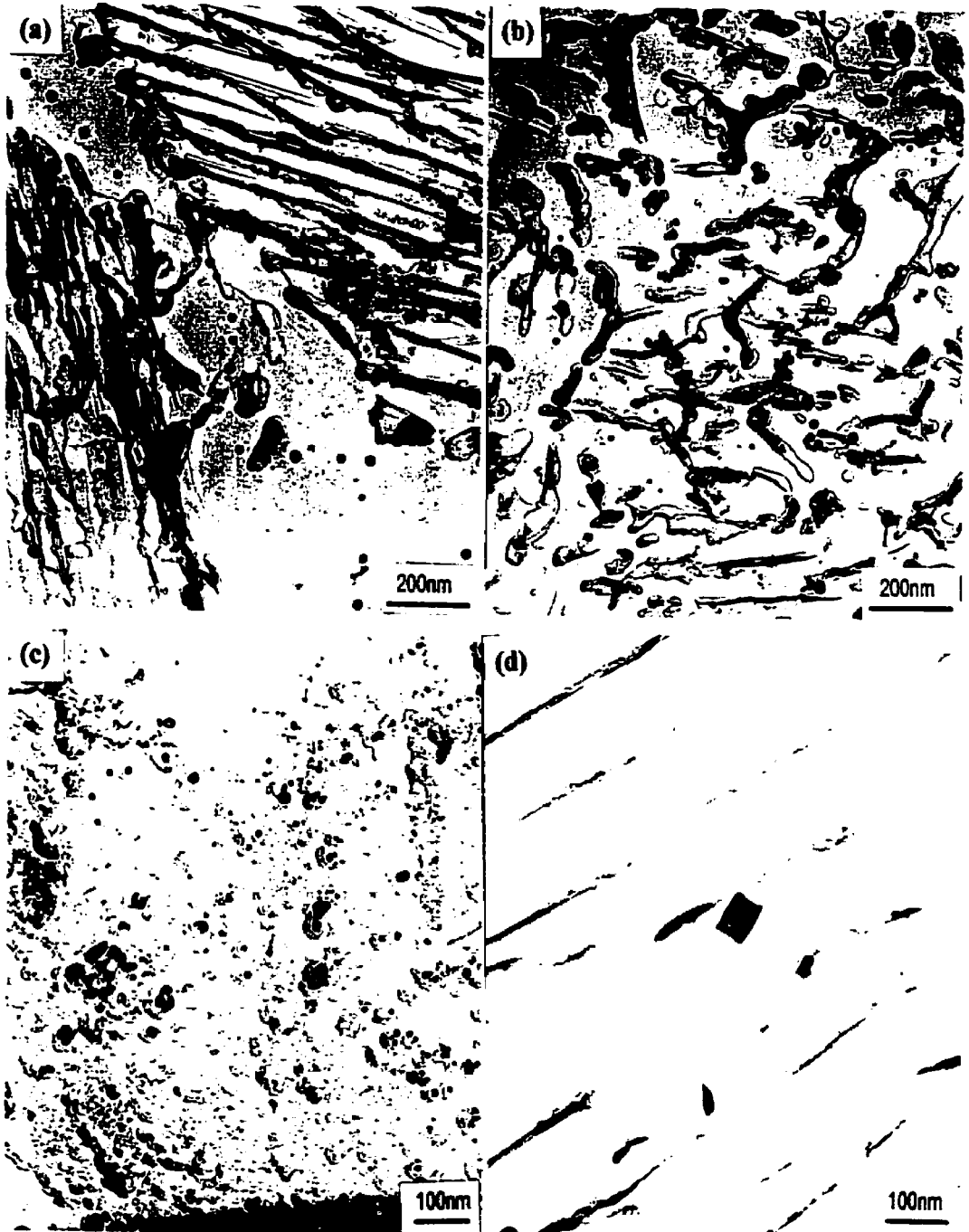


Figure 4.2 Precipitate distributions in as-rolled bar. (a and b) 1541Nb. (c) 1541VTi. (d) 1541Al.

Table 4.1 Precipitates in as-rolled steel bars

Steel	Type	Shape	Density	Distribution
1541Nb	Nb(C,N)	globular	high	ferrite and pearlite
1541VTi	(Ti,V)(C,N) Ti-rich	cuboidal	low	ferrite and pearlite
	(Ti,V)(C,N) V-rich	globular	high	
1541Al	AlN	cuboidal	low	ferrite and pearlite
1141Nb	Nb(C,N)	globular	high	ferrite and pearlite

4.2 Grain Growth During Induction Reheat

Typical austenite grain structures after induction heating at different temperatures are shown in Figures 4.3(a, b). Figure 4.4 gives the effects of heating temperature and holding time on the mean austenite grain diameter. 1541Nb and 1541Al had small grain sizes when the temperature was less than 1000°C, but the grain size increased quickly when the temperature was higher. Grain size also increased with increasing holding time, especially at higher temperatures. Although 1541VTi had similar grain sizes to the other steels at lower temperatures ($T < 1000^\circ\text{C}$), its grain size was much smaller at higher temperature. The heating temperature and holding time had less effect on the grain sizes of 1541VTi.

Normal grain growth was observed in all the steels at 900°C. Abnormal grain growth was found at higher temperatures. In the latter case, some grains were much larger than the neighboring grains. Therefore, mixed grain sizes were observed in the microstructure. For 1541VTi, abnormal grain growth was found at 1000°C or higher. For 1541Nb and 1541Al, abnormal grain growth occurred in the temperature ranges 1050-1200°C and 950-1150°C, respectively.

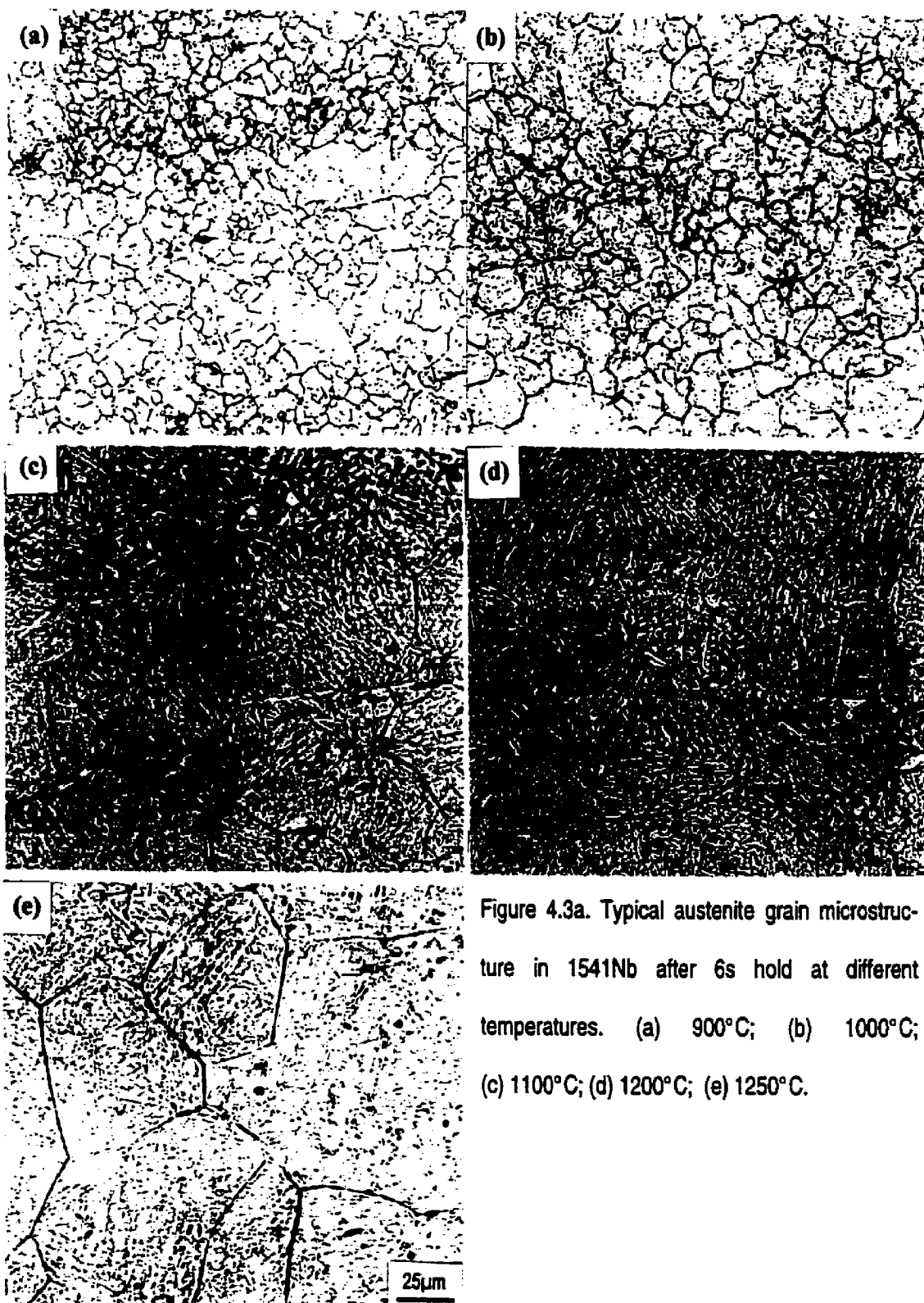


Figure 4.3a. Typical austenite grain microstructure in 1541Nb after 6s hold at different temperatures. (a) 900°C; (b) 1000°C; (c) 1100°C; (d) 1200°C; (e) 1250°C.

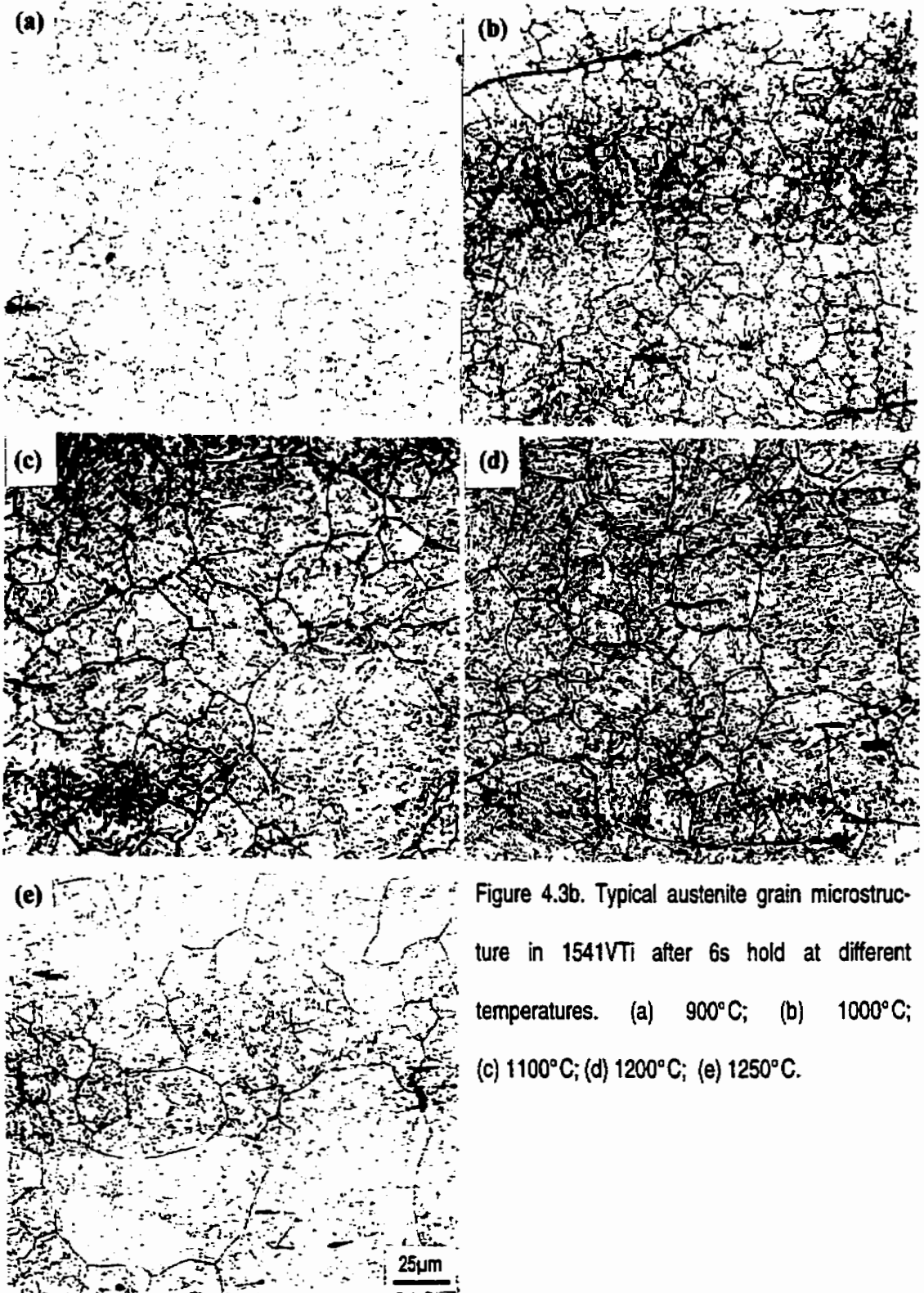


Figure 4.3b. Typical austenite grain microstructure in 1541VTi after 6s hold at different temperatures. (a) 900°C; (b) 1000°C; (c) 1100°C; (d) 1200°C; (e) 1250°C.

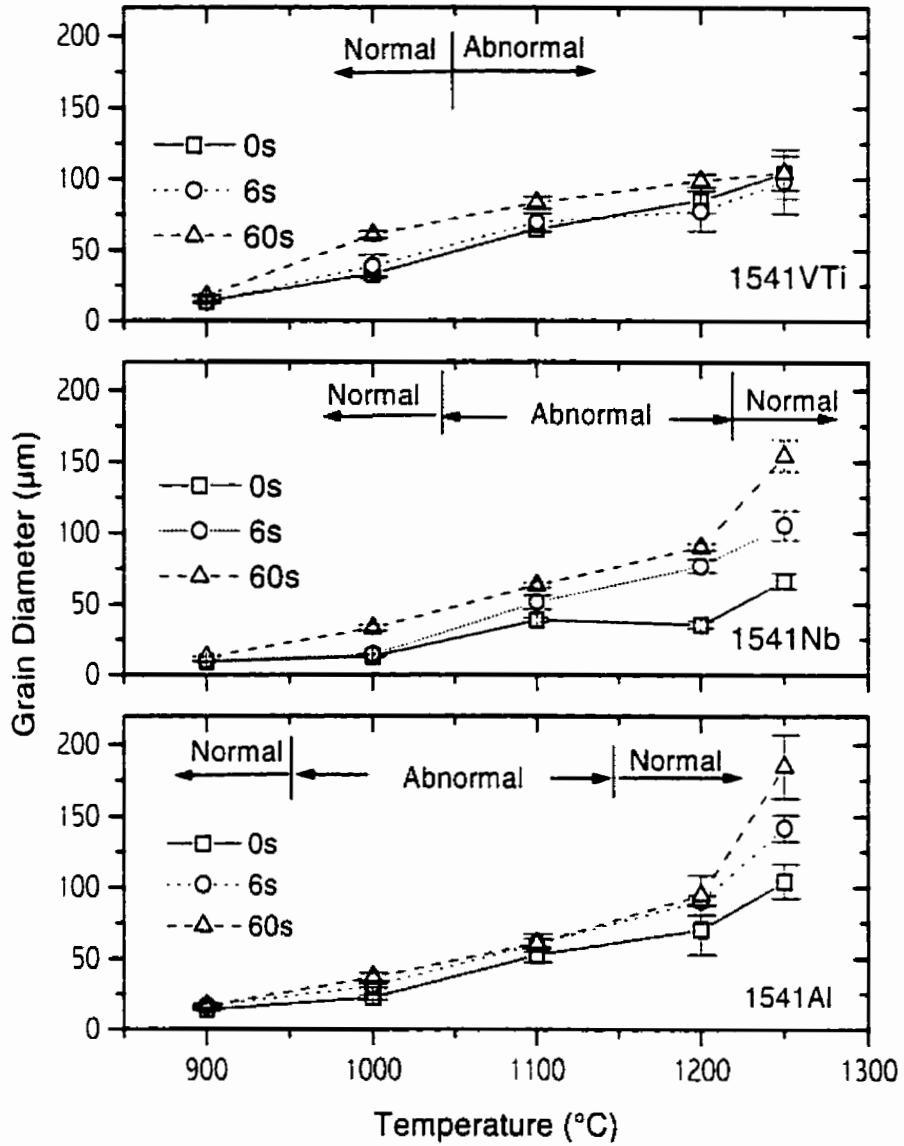


Figure 4.4 Austenite grain diameter as a function of heating temperature and holding time.

4.3 Precipitate Evolution during Induction Reheat

Typical precipitate distributions in reheated samples are shown in Figure 4.5. Both small and large precipitates were observed at each heating temperature, but the density of precipitates decreased significantly at high temperature, indicating the volume fraction of precipitates decreased with increasing temperature. Precipitates were observed in 1541VTi and 1541Nb even at the highest heating temperature (1250°C), showing that the temperatures for complete dissolution of the precipitates are higher than 1250°C.

Most of the undissolved precipitates in 1541Nb were globular, but those in 1541VTi were predominantly cuboidal after heating at high temperature ($T > 1100^\circ\text{C}$).

The precipitate size distributions in the as-rolled condition and after heating at different temperatures are shown in Figure 4.6 for 1541Nb. The distributions are right skewed, similar to a log-normal distribution. There is little variation in the mean precipitate diameter or the overall size distribution with increasing temperature.

For 1541VTi, bimodal distributions were observed for the hot-rolled condition and after heating at low temperatures, with one peak at ~15nm (diameter) and the other at 35nm. With increasing heating temperature, the peak of smaller sizes decreased and eventually disappeared at 1100°C. This indicates that a large amount of small precipitates dissolved during induction heating. The position of the larger-diameter peak only slightly changed with temperature. Since most of the small precipitates in 1541VTi were V-rich carbonitrides, they dissolved quickly when the temperature is close to 1000°C. Most of the large precipitates were Ti-rich carbonitrides, which were stable because of the low solubility of Ti carbonitrides.

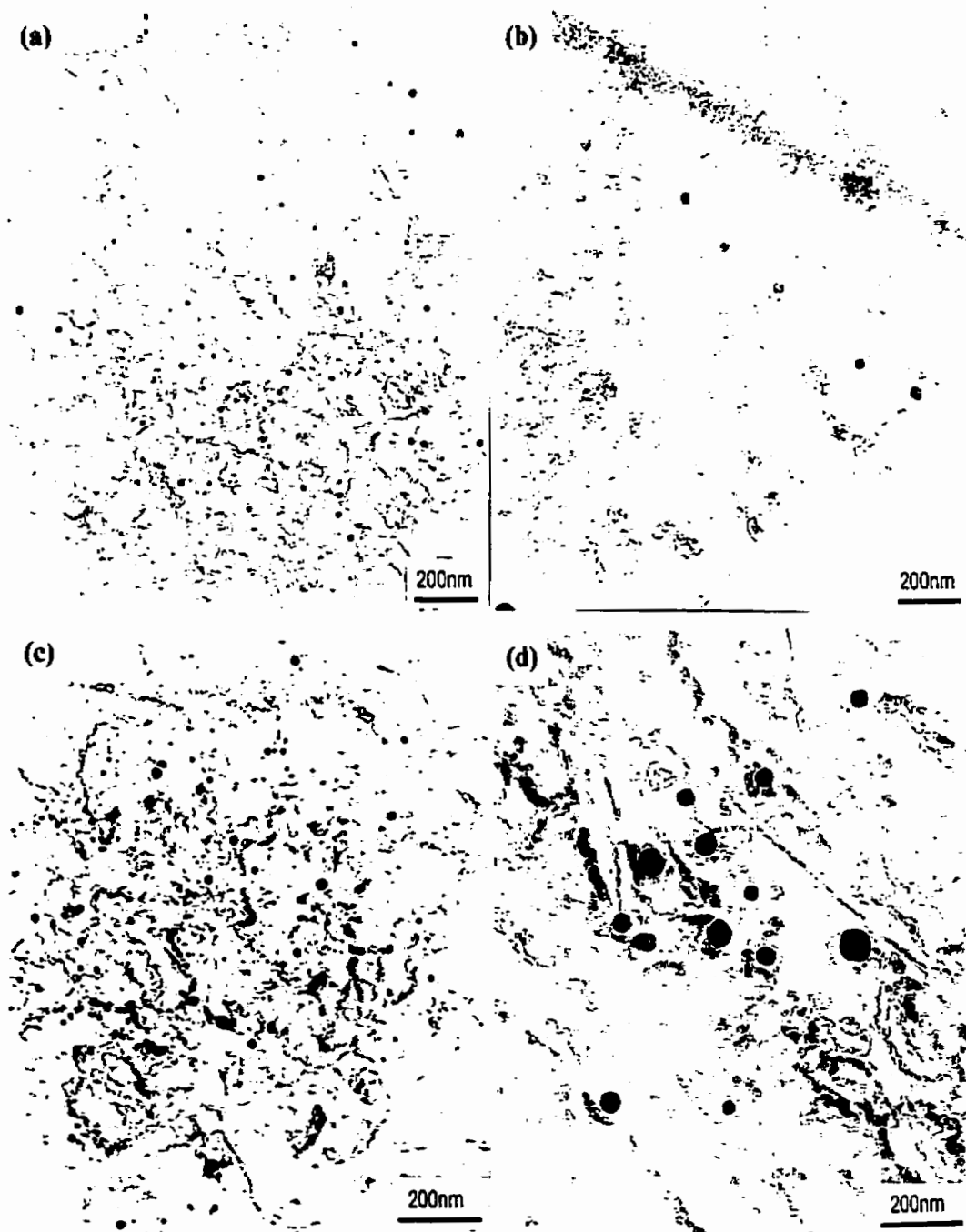


Figure 4.5 Typical precipitate distributions after 6s hold at different temperatures. (a) 1541VTi, 1000°C; (b) 1541VTi, 1200°C; (c) 1541Nb, 1000°C; (d) 1541Nb, 1250°C.

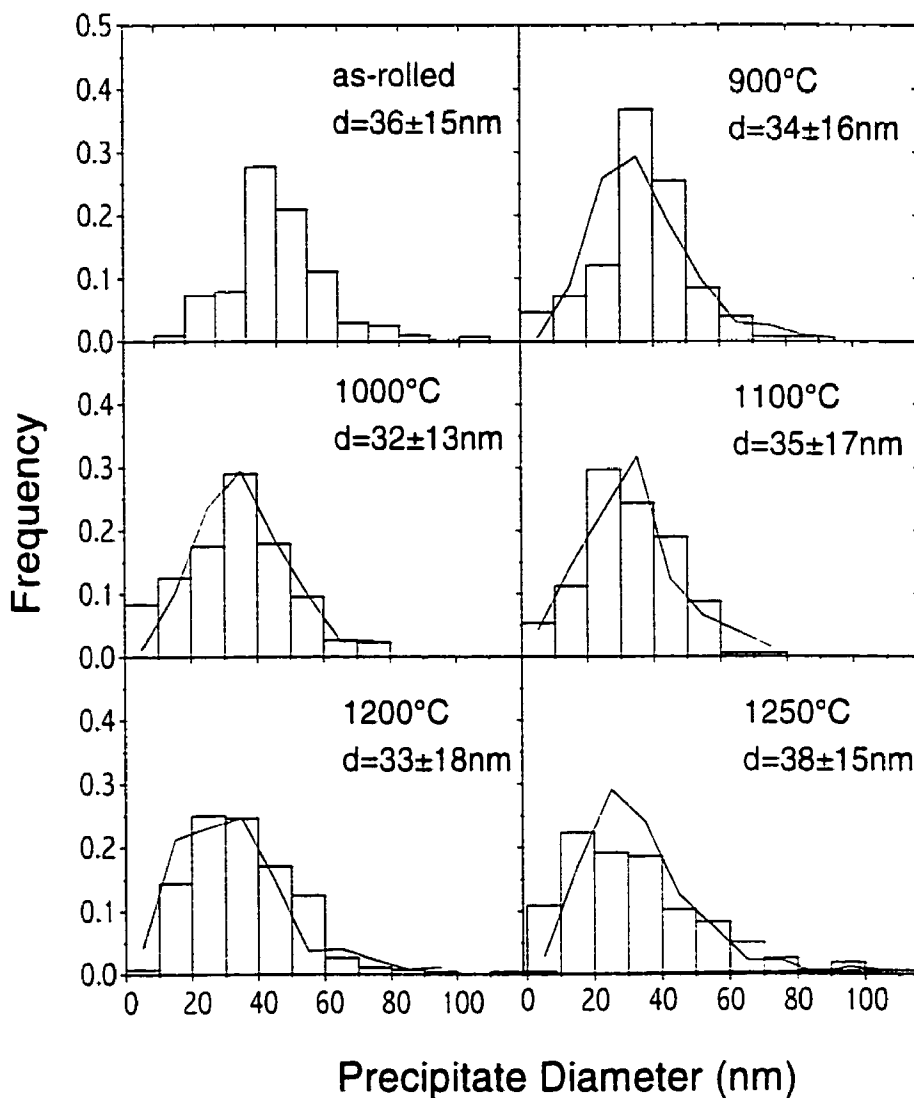


Figure 4.6a Measured precipitate size distributions (histograms) for as-rolled condition and after induction reheat with 6s hold (1541Nb). Solid lines are calculated with the precipitate evolution model given in §4.5.

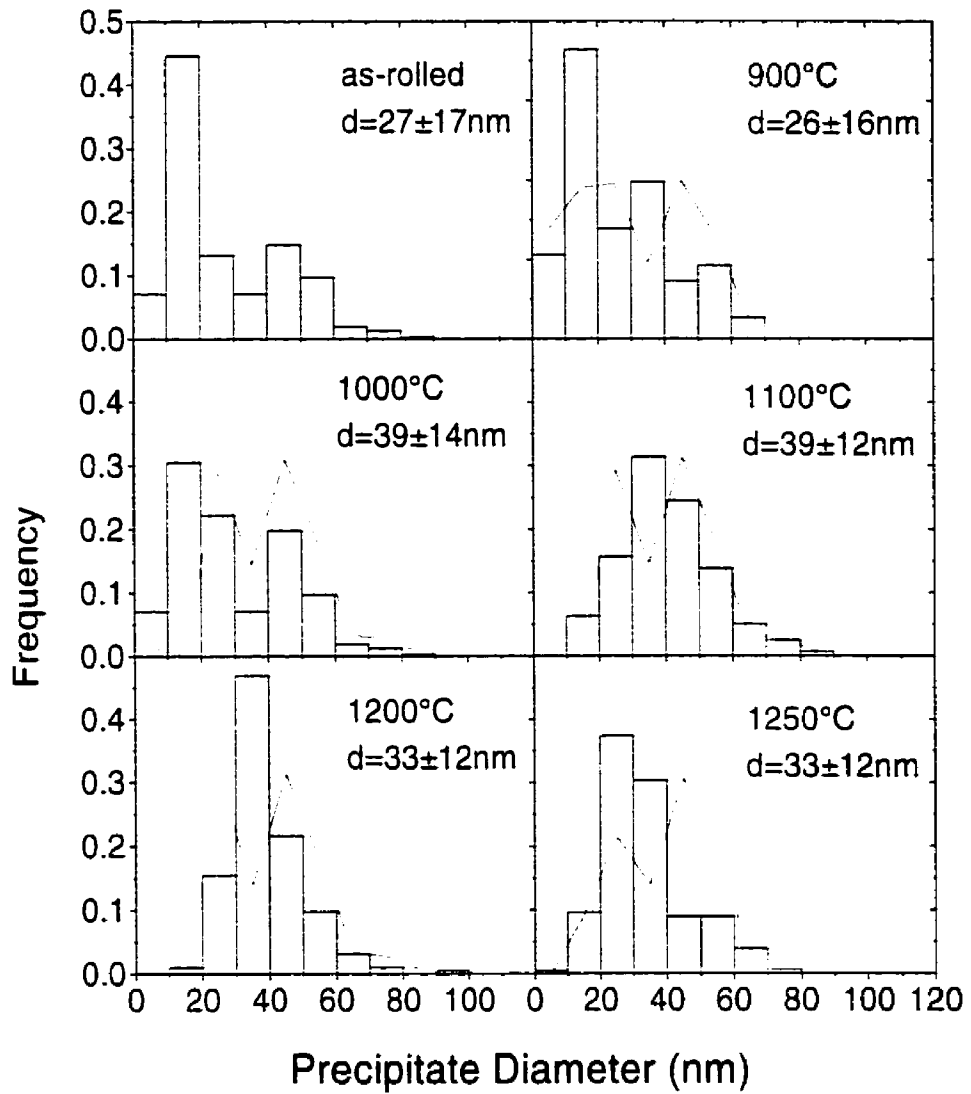


Figure 4.6b Measured precipitate size distributions (histograms) for as-rolled condition and after induction reheat with 6s hold (1541VTi). Solid lines are calculated with the precipitate evolution model given in §4.5.

The Ti/V ratio of the undissolved precipitates in 1541VTi increased with increasing temperature. This means that more V than Ti has dissolved into the matrix due to the high solubility of V(C,N). It is also expected that the C/N ratio of the carbonitrides decreased with increasing temperature. This tendency is predicted by solubility calculations, but could not be verified by the EDS used because of the capacity of the detector.

4.4 Discussion of Grain Growth and Precipitate Evolution During Induction Reheat

The grain growth behaviour of the steels studied can be divided into three stages: (1) Small and uniform grain sizes at low temperature. (2) Mixed grain sizes at intermediate temperature. At this stage, most of the grains remain small, while a small number of grains become unusually large compared with their neighbours. (3) Large but uniform grain sizes at high temperature. The grain growth mechanism changes from normal to abnormal grain growth first, and then changes back to normal grain growth at higher temperature. The temperature ranges for each stage are different for the steels studied, as is shown in Figure 4.4.

Compared with the well-studied grain growth during slow furnace reheat, the grain growth behaviour of microalloyed steels during induction reheat gives a similar pattern. The grain sizes after induction reheat are smaller because of the shorter heating cycle.

The precipitate evolution during induction heating is reflected by several aspects: (1) Density. A high density of precipitates was observed in the as-rolled bars and after reheat at low temperatures. It decreases with increasing reheat temperature. (2) Size distribution. Both small and large precipitates were observed at all temperatures, but the amount of small precipitates at low reheat temperatures is much higher than at high

temperatures. (3) Composition. A composition change was observed for the (Ti,V)(C,N) precipitates in 1541VTi. It was found that the Ti/V ratio increases with increasing reheat temperature, because Ti carbonitrides are more stable at high temperature (lower solubility). It is also expected that the N/C ratio increases with increasing temperature. (4) Shape. The change of shape was not obvious for each kind of precipitates during induction reheat.

The grain growth behaviour of microalloyed steels is closely related to the precipitate evolution during reheat. A high density of small precipitates was observed in the first stage. Under these conditions, the precipitate pinning is high enough to prevent all the grains from growing larger. At higher temperatures, the small precipitates gradually dissolve into and precipitate density decreases. Since the precipitates were not uniformly distributed, grain growth becomes faster in those areas where there is a low density of precipitates. These grains become much larger than the others and abnormal grain growth is observed. With increase of temperature, most of the precipitates dissolve. The grains grow larger with little pinning force. Therefore, normal grain growth is observed again at high temperatures.

Compared with conventional furnace reheat, the difference in precipitate evolution during induction reheat is mainly reflected by its size change. The mean precipitate diameter in 1541Nb was nearly unchanged during induction heating, and that in 1541VTi initially increased and then remained nearly unchanged with increasing temperature (Figure 4.6). It is well known, however, that mean precipitate sizes increase with temperature during conventional furnace reheat. This indicates that the precipitate evolution during induction reheat cannot be explained solely by particle coarsening.

which is the case for conventional furnace reheat.

It is interesting that the precipitate evolution during induction reheat is also different from a diffusion-controlled precipitate dissolution process. According to the precipitate dissolution model given by Agren (1990, Equation 2.20.), the mean precipitate sizes should decrease with increasing reheat temperature.

Clearly, the precipitate evolution of microalloyed steels during induction heating cannot be explained with the existing models. New models need to be established to understand the physical processes during induction reheat.

4.5 Modeling Precipitate Dissolution-Coarsening during Induction Heating

(A) Dissolution and coarsening of a distribution of precipitate sizes

Two types of phase transformations may happen for precipitates during induction heating: precipitate dissolution and coarsening. The relationship between precipitate dissolution and coarsening is illustrated in Figure 4.7, which shows the variations in the precipitate size and volume fraction as a function of holding time at a fixed temperature. Initially, precipitate dissolution dominates, with continuous decrease in both precipitate size and volume fraction. When the equilibrium volume fraction of precipitates is reached, precipitate coarsening becomes the controlling process. For conventional furnace reheat, the dissolution time is a small fraction of the total holding time, and it can be neglected. For induction reheat, however, the precipitate dissolution time has to be taken into account because of the rapid heating rate and short holding time.

For diffusion-controlled precipitate dissolution, Agren (1990) gave the following equation (Equation 2.20):

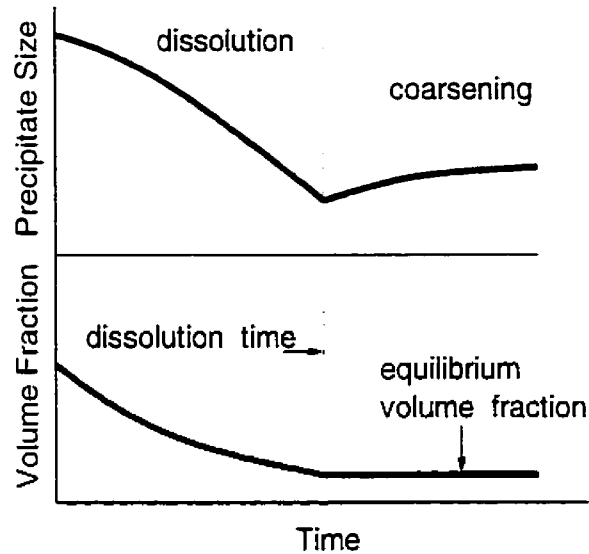


Figure 4.7 Schematic of the variation in precipitate size and volume fraction during dissolution and coarsening. (Up-quench is assumed followed by isothermal holding.)

$$\frac{\bar{r}_v}{\bar{r}_{v0}} = \left(\frac{r}{r_0} \right)^3 \quad [4.1]$$

This equation shows that the mean precipitate size decreases with increasing reheat temperature, which is not in agreement with the experimental observation in this study. The problem comes from the assumption behind Equation 4.1, i.e., all the precipitates are of the same size. It is well known that in almost all the materials precipitate sizes fall in a certain range. Considering this, a basic point is set for the modeling: *a group of precipitates of different sizes*. It will be seen that a series of modifications has been made based on this point.

For the dissolution of a distribution of precipitate sizes, it is assumed that each precipitate dissolves independently during induction heating. This means that no soft

impingement of diffusion fields occurs between neighboring precipitates. This is reasonable for microalloyed steels because of the low volume fraction of precipitates. The dissolution rate is given by Equation 2.13:

$$r_0^2 - r^2 = 2k_s D_m t \quad [4.2]$$

where D_m values are given in Table 2.5 for microalloy elements. k_s is calculated from solubility product data (Table 2.2).

In order to determine the volume fraction of precipitates during induction heating, Equation 4.1 needs to be modified for a distribution of precipitate sizes. The volume change for each precipitate has been considered individually; therefore, the change of volume fraction can be expressed as:

$$\frac{f_v}{f_{v0}} = \frac{\sum_{i=1}^m r(i)^3}{\sum_{i=1}^m r_0(i)^3} \quad [4.3]$$

It should be noted that the values of m and m' do not have to be the same because some precipitates dissolve completely.

Equation 4.2 implies that complete dissolution occurs at $t = r_0^2 / 2k_s D_m$. This is not always true since dissolution will stop when equilibrium is reached. If f_{vT} is the equilibrium volume fraction at temperature T , the dissolution time (t_d) from Equations 4.1 and 4.2 is:

$$t_d = \frac{1 - (f_{vT} / f_{v0})^{2/3}}{2k_s D_m} r_0^2 \quad [4.4]$$

The precipitate coarsening is assumed to occur when the holding time is longer than the dissolution time. For a distribution of precipitates, the widely-used LSW equation

(Equation 2.15) is no longer suitable since it can only be used for the change of mean precipitate size, while the present model considers a group of precipitates individually. A more fundamental equation given by Greenwood (1956) has been used (Equation 2.14):

$$\frac{dr}{dt} = \frac{2\gamma_i D_m V_M^2 X_w}{RT_r} \left(\frac{1}{\bar{r}} - \frac{1}{r} \right) \quad [4.5]$$

where $\gamma_i \approx 0.5 \text{ J} \cdot \text{mol}^{-1}$ according to Liu and Jonas (1988). V_M is calculated by the methods given in §2.5.

(B) Precipitate dissolution and coarsening during continuous heating

The above derivation assumes isothermal heating. For continuous heating, the induction heating cycle is divided into small time intervals of 0.01 second. Isothermal condition is assumed for each interval, and the evolution of precipitate sizes is calculated from Equations 4.1-4.5 by step-by-step numerical calculations. The procedure is illustrated in Figure 4.8, and the computer program is given in Appendix B.

Precipitate coarsening is taken into account if complete dissolution occurs during holding. The holding time is also divided into small intervals. The size change of each precipitate is calculated in each interval, and the change of precipitate size distribution during coarsening is determined by numerical methods.

The measured precipitate sizes in the as-rolled condition are input as initial precipitate sizes. The size of each precipitate is tracked during each time interval. The dissolved microalloy content from all the precipitates is monitored so that the equilibrium solubility is not exceeded. With this method, the precipitate evolution at any stage of an induction heating cycle can be computed.

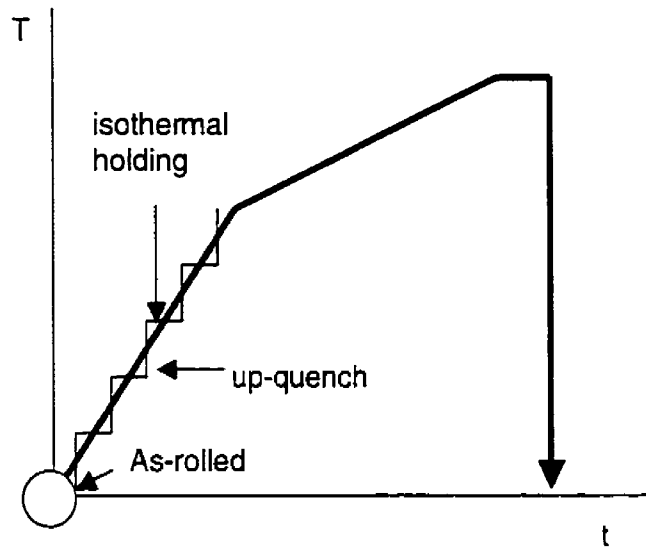


Figure 4.8 Schematic of calculation procedures. It is assumed that microstructural evolution occurs only during isothermal holding.

The starting temperature is not chosen as room temperature, since the solubility products in ferrite are not known for microalloy carbonitrides. The solubility product equations are no longer valid if extended to such low temperatures. Thus, the starting temperatures are selected as the temperatures where maximum volume fraction of precipitates is obtained (720°C for 1541Nb and 700°C for 1541VTi).

A group of empirical equations have been given for each type of carbides or nitrides (Table 2.2). The calculated solubility varies in a certain range for each type of binary carbides or nitrides, especially for TiN. It is difficult to determine which one is more accurate or more suitable for the materials used in this study. For the present modeling, the solubility product equations have been selected as the ones which give the intermediate values in each group except for TiN. It seems that most of the empirical equations overestimate the stability of TiN for microalloyed forging steels which have

much higher carbon and nitrogen contents. Therefore, the empirical equation which gives the maximum solubility has been used for TiN in this study. The following empirical equations have been used in this study:

$$\text{For NbC: } \lg[\text{Nb}][\text{C}] = 4.37 - 9290/T \quad [4.6a]$$

$$\text{For NbN: } \lg[\text{Nb}][\text{N}] = 4.04 - 10230/T \quad [4.6b]$$

$$\text{For TiC: } \lg[\text{Ti}][\text{C}] = 2.75 - 7500/T \quad [4.6c]$$

$$\text{For TiN: } \lg[\text{Ti}][\text{N}] = 0.322 - 8000/T \quad [4.6d]$$

$$\text{For VC: } \lg[\text{V}][\text{C}] = 6.72 - 9500/T \quad [4.6e]$$

$$\text{For VN: } \lg[\text{V}][\text{N}] = 3.46 - 8330/T \quad [4.6f]$$

(C) Precipitate evolution during induction heating

The precipitate sizes in the as-rolled samples are used as the initial condition. The modeled precipitate size distributions are superimposed on the measured histograms in Figure 4.6 (a,b). The agreement is excellent for 1541Nb and reasonable for 1541VTi.

The predicted variation in mean precipitate diameter and volume fraction with reheat temperature is shown in Figure 4.9 for 1541Nb. The volume fraction of precipitates decreases significantly with increasing temperature. The mean precipitate diameter does not change much with temperature (slight decrease at lower temperature because of precipitate dissolution, and then slight increase at high temperature due to precipitate coarsening). This result is in agreement with the experimental observations, which could not be explained by the previous models.

The effect of temperature on the dissolution time (i.e., the time to reach equilibrium) is shown in Figure 4.10 for 1541Nb. The dissolution time decreases quickly with

increasing temperature, and is less than a few seconds when $T \geq 1050^\circ\text{C}$. This means that the equilibrium solubility can be reached during rapid induction heating.

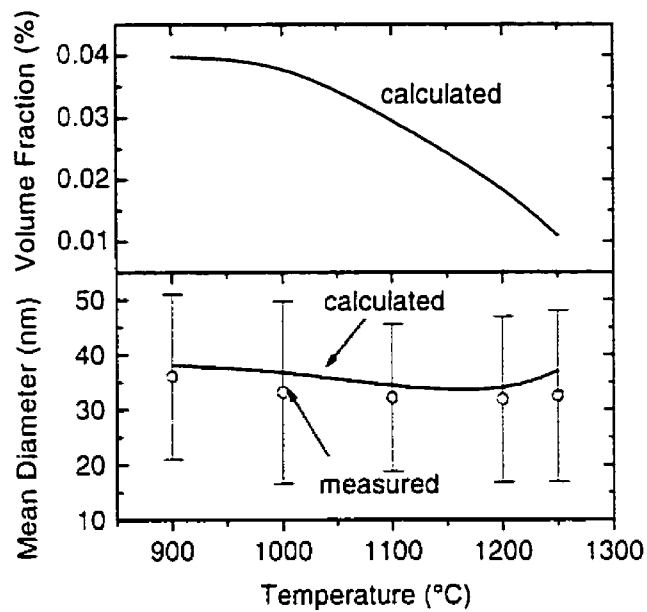


Figure 4.9 Effect of heating temperature on volume fraction and mean precipitate diameter for 6s hold (1541Nb).

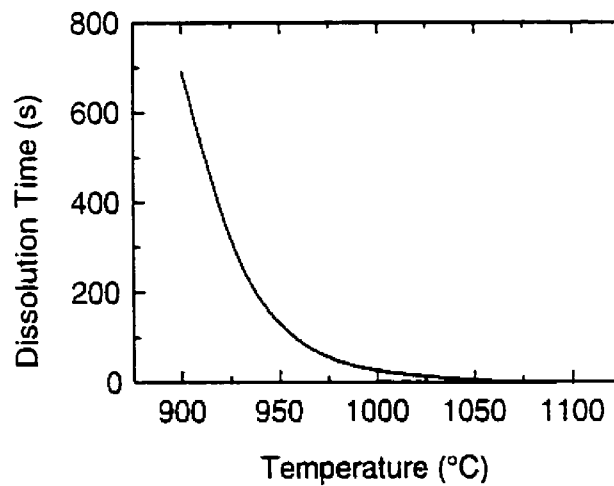


Figure 4.10 Effect of temperature on precipitate dissolution (1541Nb).

Figure 4.11 shows the computed variation in precipitate diameters for 1541Nb under continuous heating at $10^{\circ}\text{C}/\text{s}$. The dissolution rate increases with increasing temperature. Small precipitates dissolve at lower temperatures, while large precipitates become smaller with increasing temperature.

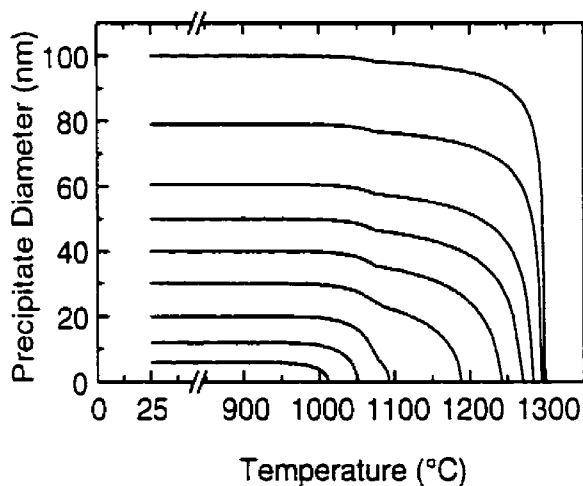


Figure 4.11 Variation of precipitate diameter with temperature during continuous heating (1541Nb).

The calculations become much more complex when applying this model to 1541VTi, because two types of precipitates (V-rich and Ti-rich) are present in the steel. Two assumptions have been examined:

(1) Assuming the precipitates in the as-rolled conditions are of the same composition that is given by the equilibrium solubility, and precipitate dissolution is controlled by the volume diffusion of Ti for all the precipitates.

(2) Assuming two types of precipitates are present in the as-rolled samples (both V-rich and Ti-rich); and dissolution of V-rich precipitates is controlled by diffusion of V and Ti-rich precipitates by Ti, respectively.

It is found that the calculation following the first assumption is very complex because

the equilibrium solubility of V and Ti of the precipitates are difficult to calculate. The computed results overestimate the stability of the small precipitates. In other words, the precipitates of smaller sizes remain undissolved until the temperature reaches 1200°C, while experiments show that these precipitates disappear when temperature reaches 1100°C.

For the second assumption, the difficulty comes from separating the V-rich and Ti-rich precipitates in the as-rolled condition. In this study, the precipitates are separated according to the observed precipitate size distributions. The bimodal distribution is sectioned at the cross point ($d=27\text{nm}$) of the two distributions. Those with smaller sizes are considered to be V-rich, and the remainder Ti-rich precipitates. The computed evolution of precipitate sizes following this assumption are shown in Figure 4.6b. This model successfully predicted the disappearance of the left distribution, and size change of the larger-diameter distribution with temperature.

4.6 A Modified Zener Equation for a Distribution of Precipitate Sizes

Considering the evolution of a distribution of precipitate sizes, rather than a uniform size, not only changes the precipitate dissolution and coarsening behavior, but also changes the pinning force on grain boundary migration (Figure 4.12). Thus the Zener equation needs to be modified to incorporate this factor. The following section gives a modified Zener equation to reflect the effect of a precipitate size distribution on precipitate pinning.

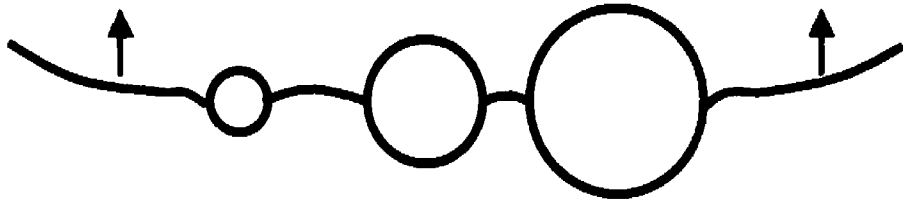


Figure 4.12 Schematic of Zener pinning from a group of precipitates of different sizes.

(A) Derivation of the Expression

(1) The pinning force from a single precipitate at a grain boundary: Following Zener's derivation (Smith, 1948), the maximum pinning force for a precipitate of radius r is:

$$F_z(r) = \pi r \gamma_{gb} \quad [4.7]$$

(2) Surface density of precipitates (N_v) on the grain boundary: The relationship between surface density, volume fraction and precipitate radius is given by (Ashby and Ebeling, 1966):

$$N_v = \frac{3f_v}{2\pi(\bar{r}^2 + \sigma^2)} \quad [4.8]$$

where \bar{r} and σ are the mean and standard deviation of the precipitate size distribution, respectively.

(3) Total pinning pressure from a distribution of precipitate sizes: The distribution of precipitate sizes can be divided into small groups (Figure 4.13). Considering a small group of mean radius r and frequency $\rho(r)$, the surface density for this group is:

$$N_v(r) = \rho(r)N_v \quad [4.9]$$

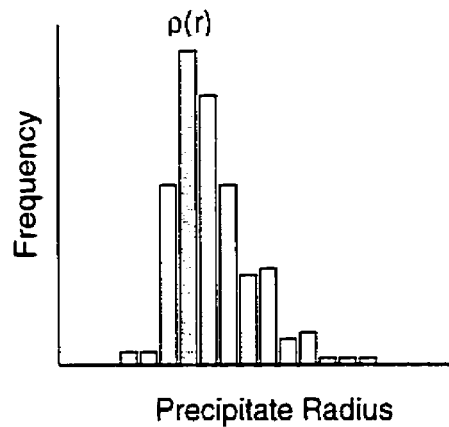


Figure 4.13 Schematic showing a small section in a distribution of precipitate sizes.

All the precipitates are considered to be the same size in each small group. The total pinning pressure from the group of size r is then:

$$P_z(r) = F_z(r) \cdot N_z(r) = \frac{3r\gamma_{gb}f_v\rho(r)}{2(\bar{r}^2 + \sigma^2)} \quad [4.10]$$

Similarly we can get the pinning pressure from other small groups of different sizes. The total pinning pressure from all the precipitates is then:

$$P_z = \frac{3\gamma_{gb}f_v}{2(\bar{r}^2 + \sigma^2)} \sum r\rho(r) \quad [4.11]$$

If all the precipitates are of the same size, i.e., $\sigma=0$, then Equation 4.11 reduces to Equation 2.32.

(4) Definition of equivalent precipitate size. A term "equivalent precipitate size (r_{eq})" is defined as:

$$r_{eq} = \frac{\bar{r}^2 + \sigma^2}{\sum r\rho(r)} \quad [4.12]$$

The physical meaning of r_{eq} is that if all the precipitates are of this size, the total pinning

pressure is equal to that from all the precipitates in the distribution at the same volume fraction level. Note that the related parameters, \bar{r} , σ , and $\rho(r)$, can be determined by experiment. With this definition, Equation 4.11 can be simplified as:

$$P_z = \frac{3f_v \gamma_{gb}}{2r_{eq}} \quad [4.13]$$

(5) Calculation of critical grain size. The driving pressure (P_z) for grain growth is given by Zener (Smith, 1948):

$$P_z = \frac{2\gamma_{gb}}{R} \quad [4.14]$$

where R is grain radius. Grain growth stops when the Zener pinning pressure is equal to the driving pressure. Therefore the critical grain size (R_c) is:

$$R_c = \frac{4(\bar{r}^2 + \sigma^2)}{3f_v \sum r\rho(r)} = \frac{4r_{eq}}{3f_v} \quad [4.15]$$

Considering the uncertainty of the coefficient (4/3), the more generalized form of Equation 4.15 is:

$$R_c = k_z \frac{r_{eq}}{f_v} \quad [4.16]$$

This is the modified Zener equation for a distribution of precipitate sizes. It can be found that with the definition of equivalent precipitate sizes, the simple form of the Zener equation remains unchanged, but its application has been extended. Again, if all the precipitates are of the same size ($r_{eq} = r$), Equation 4.16 reduces to the original Zener equation.

(B) Evaluating the Modified Zener Equation

Figure 4.14 gives a simple example of the effect of precipitate size distribution on Zener pinning. It is assumed that the precipitate size distribution of the right group is evenly $0.5r$, r and $1.5r$. The two groups have the same mean precipitate sizes, but the group of the uniform size gives larger pinning force.

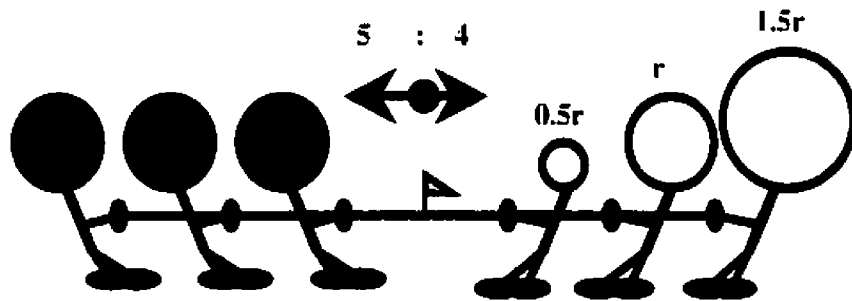


Figure 4.14 Schematic illustration of the effect of precipitate size distribution on pinning force.

(Volume fraction of precipitates is the same for both.)

In practice, the most common case likely to be encountered is that of a lognormal distribution of precipitate sizes (Herdan, 1960; Exner, 1972), which is given by (Liu *et al.*, 1993):

$$\rho(r) = \frac{1}{\sqrt{2\pi}\delta r} \exp\left[-\frac{(\ln r - \mu_r)^2}{2\delta_r^2}\right] \quad [4.17]$$

where μ_r and δ_r are the mean value and standard deviation of $\ln(r)$, respectively. They can be expressed as:

$$\bar{r} = \exp(\mu_r + 0.5\delta_r^2) \quad [4.18a]$$

$$\sigma^2 = \exp(2\mu_r + \delta_r^2)[\exp(\delta_r^2) - 1] \quad [4.18b]$$

Substituting Equations 4.17 and 4.18 into Equations 4.12 and 4.13, the equivalent precipitate size and total pinning pressure can be calculated.

With the above equations, the effect of precipitate size distribution on the equivalent precipitate size (therefore on the total pinning pressure) is determined, as is shown in Figure 4.15. It is assumed that all the distributions are of the same mean size ($\bar{r}=40\text{nm}$) but different standard deviations.

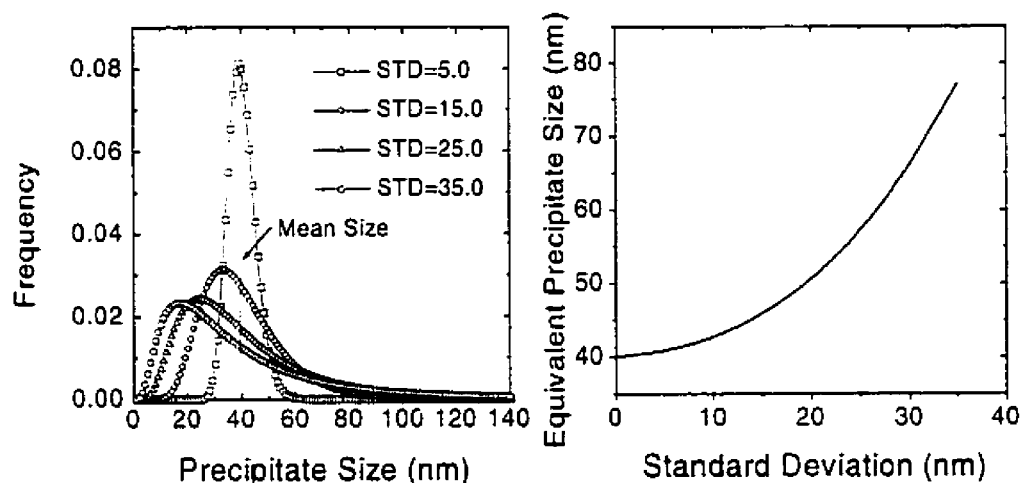


Figure 4.15 Effect of precipitate size distribution on equivalent precipitate size. The mean precipitate size is assumed to be 40nm for all the distributions.

It is found that the equivalent precipitate size increases with increasing standard deviation, although the mean precipitate size remains constant. The minimum equivalent precipitate size is obtained when the standard deviation is zero, i.e., all the precipitates are of the same size. Increased equivalent precipitate size means decreased pinning pressure according to Equation 4.14. Therefore, total pinning pressure is maximized when all the precipitates are of the same size, and it decreases with increasing variance of

precipitate sizes. This result implies that using the mean precipitate size in the Zener equation overestimates the pinning force from a distribution of precipitate sizes. The error may be as much as a fact of 2, depending on the precipitate size distribution.

4.7 Modeling Grain Growth during Induction Heating

The model of grain growth with precipitate pinning given by Andersen and Grong (1995, Eq.2.30) is used to predict grain growth during induction heating

$$\int_{D_0}^D \frac{dD}{(1/D - 1/D_c)^{n-1}} = M_0 \int_{t_0}^t \exp\left(-\frac{Q_{\text{eg}}}{RT}\right) dt \quad [4.19]$$

It has been assumed in this model that solute drag from microalloy elements is negligibly small. The effect of microalloy element is only reflected by precipitate pinning. Therefore, the grain growth data from C-Mn steels can be used for grain growth modeling. This makes Equation 4.19 suitable for different kinds of microalloyed steels. The data given by Grong (1997) are used for the calculations, where $Q_{\text{eg}} = 224\,000\text{J}\cdot\text{mol}^{-1}$; $M_0 = 2.14 \times 10^{10} \mu\text{m}^2\cdot\text{s}^{-1}$; $n = 2$.

The D_c value is calculated from the modified Zener equation (Equation 4.12 and 4.15). From the precipitate dissolution-coarsening model, the precipitate size distribution and volume fraction can be calculated, and the t_{eq} and f_v values are determined. The obtained f_v does not have to be equal to the equilibrium value since equilibrium may not always be reached during induction heating process. Then the critical grain diameter can be calculated with the modified Zener equation (Equation 4.16). The right-hand side of Equation 4.19 is calculated with the heating and holding parameters. Equation 4.19 can then be solved for D by numerical methods. The detailed calculation procedures are given

in Appendix C.

This model has been applied for the grain growth of 1541Nb and 1541VTi following the TRW heating cycle. The k_z value given by Hellman and Hillert (1975) has been used for calculation ($k_z = 4/9$). The calculated mean grain diameter as a function of reheat temperature and holding time are compared with the measured values in Figure 4.16. The modeled results agreed well with experimental observations.

It has been found that the predicted grain sizes would be much smaller than observations if the value suggested by Manohar *et al.* (1998) were used ($k_z = 0.17$). The reason may come from the grain size variation during induction reheat. From Gladman's approach, $k_z = 0.17$ corresponds to $Z_g = 1.7$. This value is smaller than the observed Z_g values during induction reheat. The actual values can be up to 3 for normal grain growth or higher for abnormal grain growth. This is close to the Hillert's model for the upper limit of normal grain growth ($k_z = 4/9$). Therefore, the prediction with Hillert's value gives better agreement.

Note that no scaling parameters have been introduced into the above models. The only data input for the modeling is the measured precipitate size distributions in the hot-rolled conditions. Even this requirement can be further simplified once the type of precipitate size distribution is known. For example, if the initial precipitate sizes follow a lognormal distribution, then the only initial input data are the mean and standard deviation of the precipitate sizes.

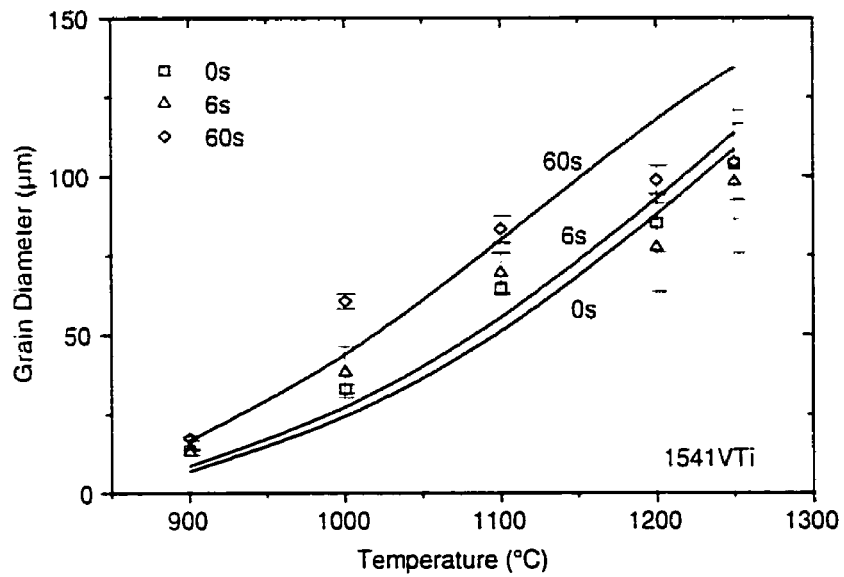
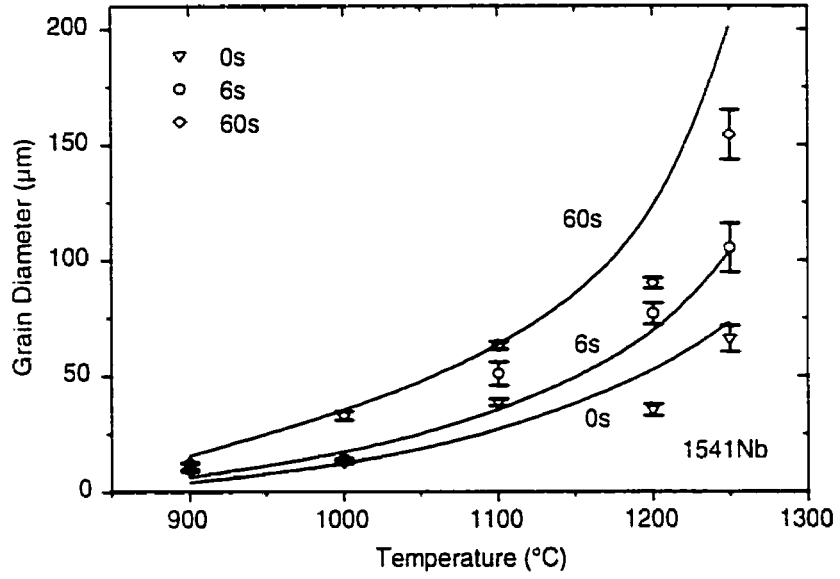


Figure 4.16 Variation in grain diameter with temperature and holding time (TRW heating cycle).

Data points are measured values and the lines are calculated from the grain growth model.

**Chapter 5. Effect of Initial Microstructure
On Grain Growth During
Induction Reheat**

5.1 Microstructures of As-Rolled Bar and After Preheat Treatment

The microstructure of 1141Nb in the as-rolled condition is shown in Figure 5.1a. It was composed of primary ferrite and pearlite. The pearlite colonies were large due to its large bar size (4 in. diameter) which results in slow cooling rate after hot-rolling. Intragranular ferrite was observed in some pearlite colonies. The elongated MnS inclusions were quite obvious in this steel because of its high sulfur content.

The microstructure in the 1250AC sample was a complex mixture of primary ferrite, Widmanstätten ferrite, bainite and pearlite, and the prior austenite grain size was very large (Figure 5.1b). The 1250Q samples had a complete martensite microstructure with a large prior austenite grain size (Figure 5.1c). The microstructure after 900AC was composed of refined and uniform primary ferrite + pearlite (Figure 5.1d).

5.2 Grain Growth During Induction Reheat

Typical austenite grain structures after reheat at different temperatures are shown in Figure 5.2 (a-d) for the 4 initial conditions, and the variation in the mean grain diameters is shown in Figure 5.3. The grain sizes were small and uniform when the reheat temperature was less than 1000°C, and the difference was small between the four initial microstructures. Abnormal grain growth was observed in the intermediate temperature range (1000-1200°C), especially for the 1250Q preheated samples. Grain sizes were large for reheat temperature higher than 1200°C. Compared with the hot-rolled condition, 1250Q produced the smallest grain size in the intermediate temperature range (1100°C), while 1250AC had distinctly larger grain sizes at high temperature (>1200°C).

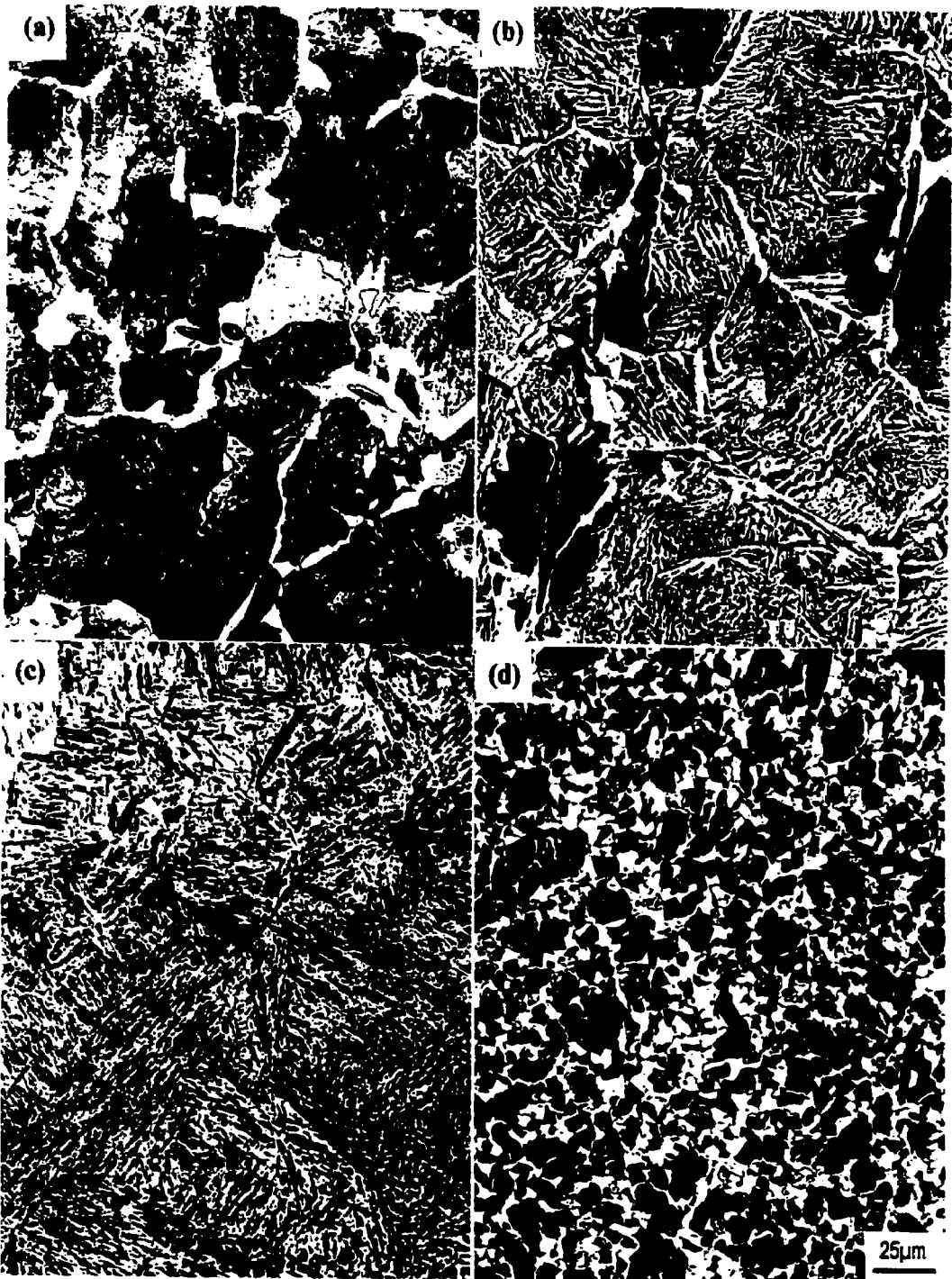
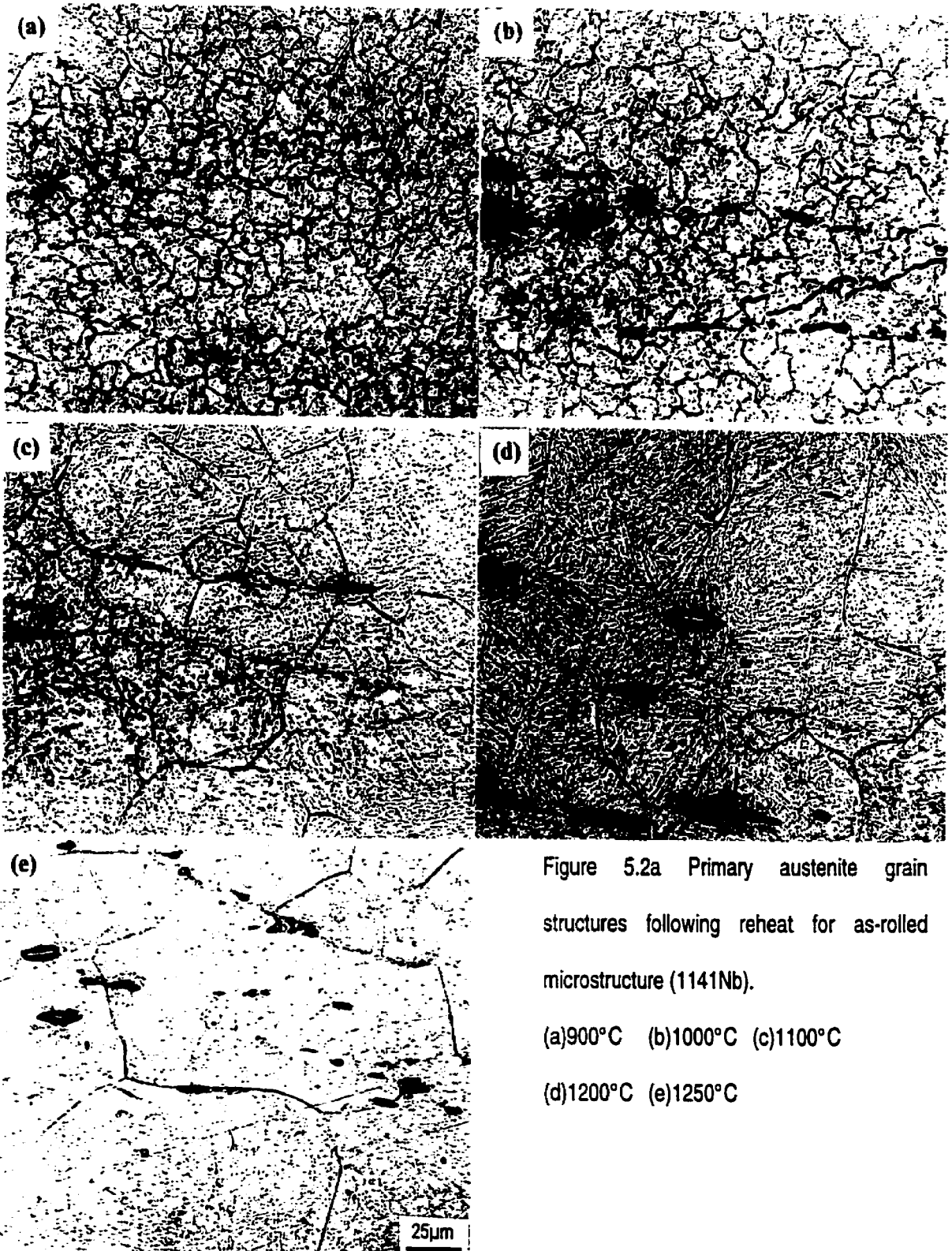
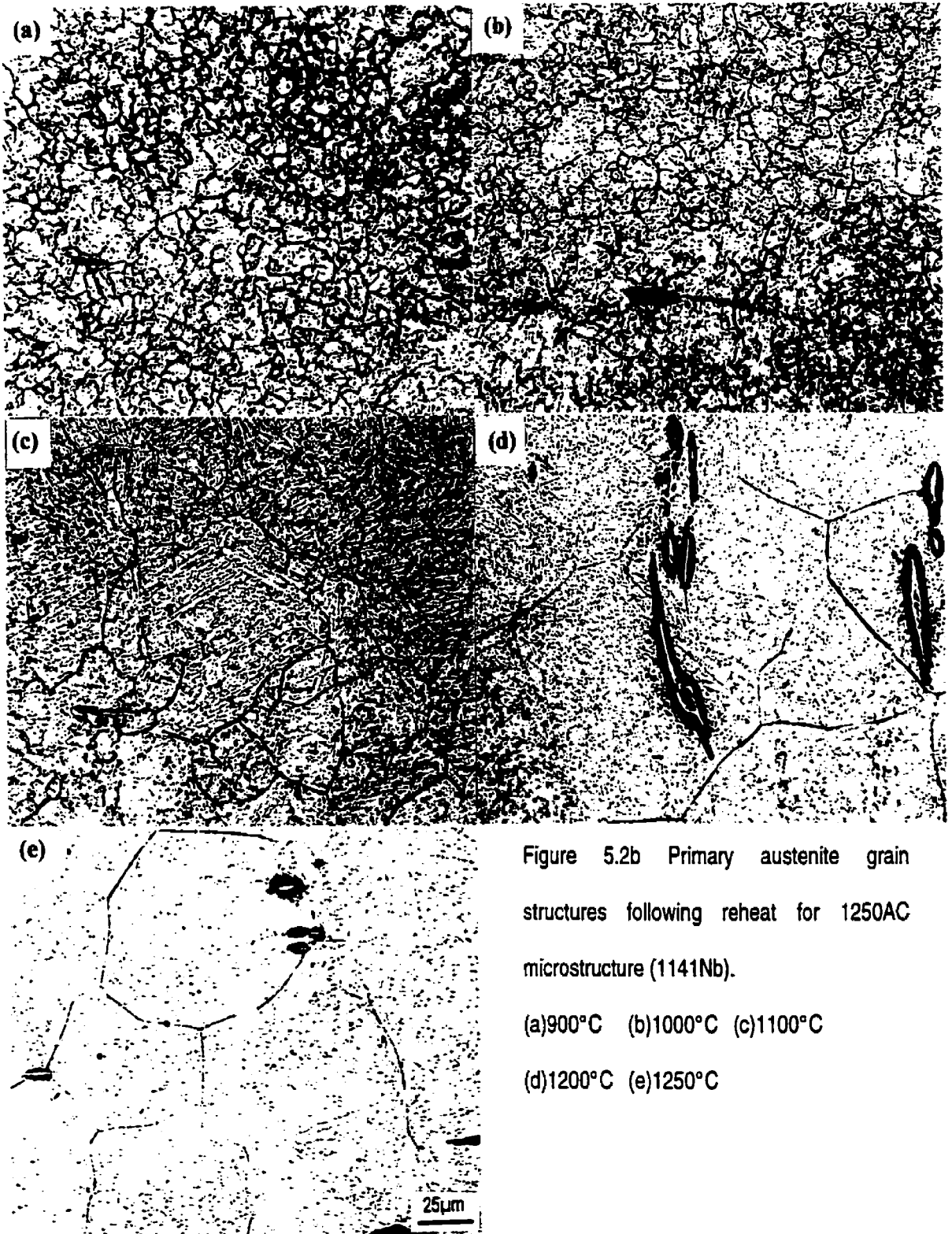


Figure 5.1 Initial microstructures of hot-rolled bar and after preheat treatment (1141Nb). (a) as-rolled: pearlite + ferrite; (b) 1250AC: pearlite + ferrite + Widmanstatten ferrite + bainite; (c) 1250Q: martensite; (d) 900AC: pearlite + ferrite (refined).





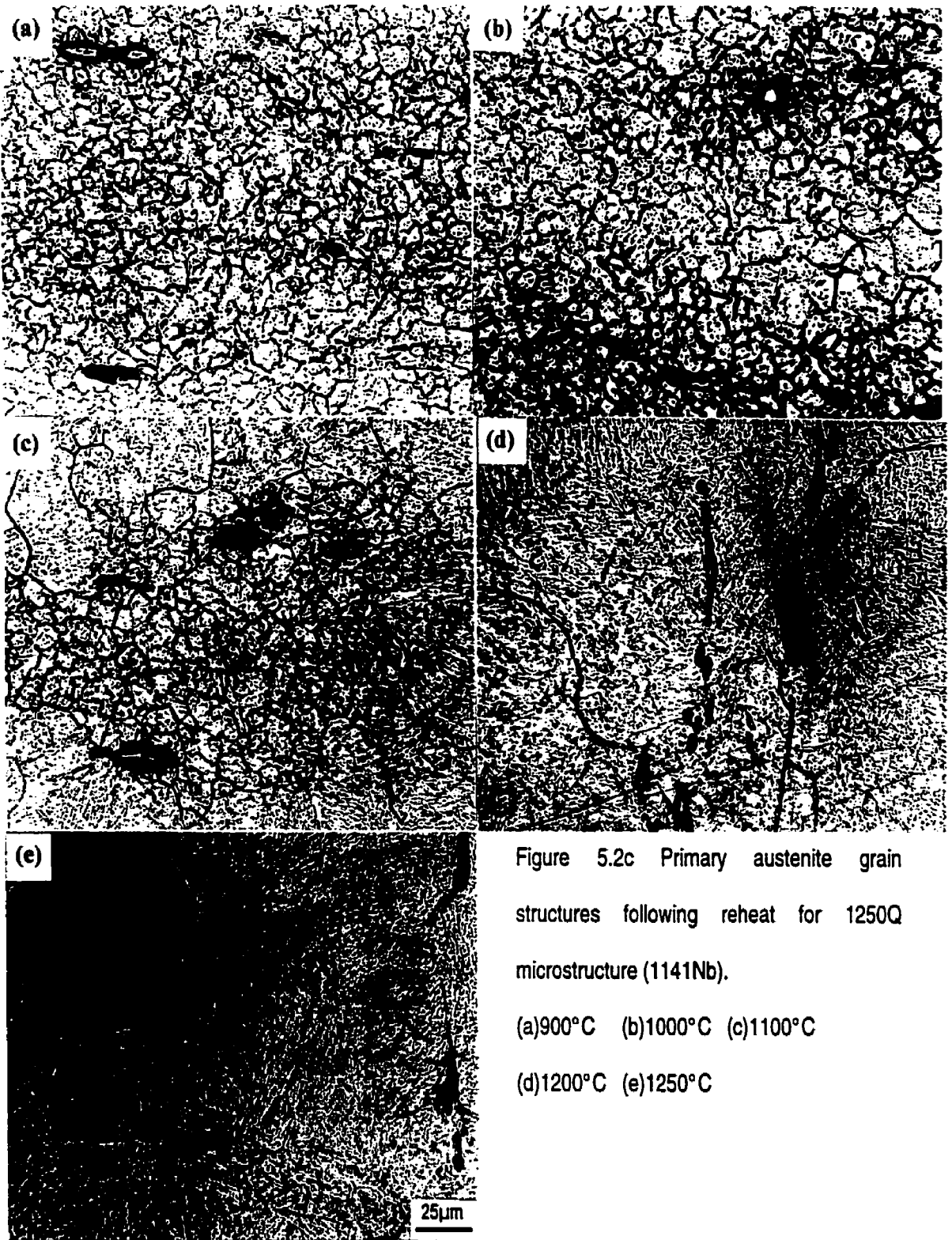
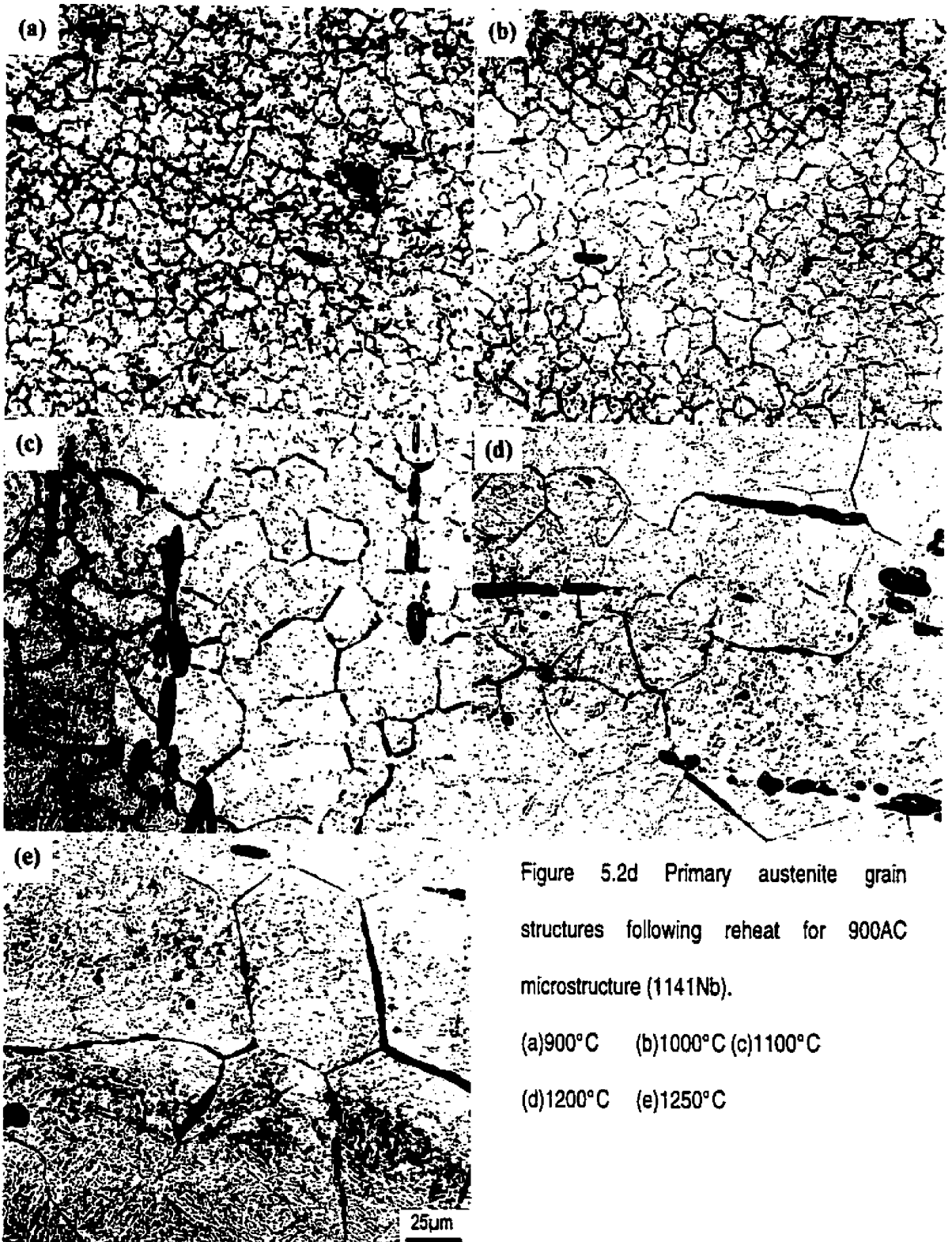


Figure 5.2c Primary austenite grain structures following reheat for 1250Q microstructure (1141Nb).

(a)900°C (b)1000°C (c)1100°C

(d)1200°C (e)1250°C



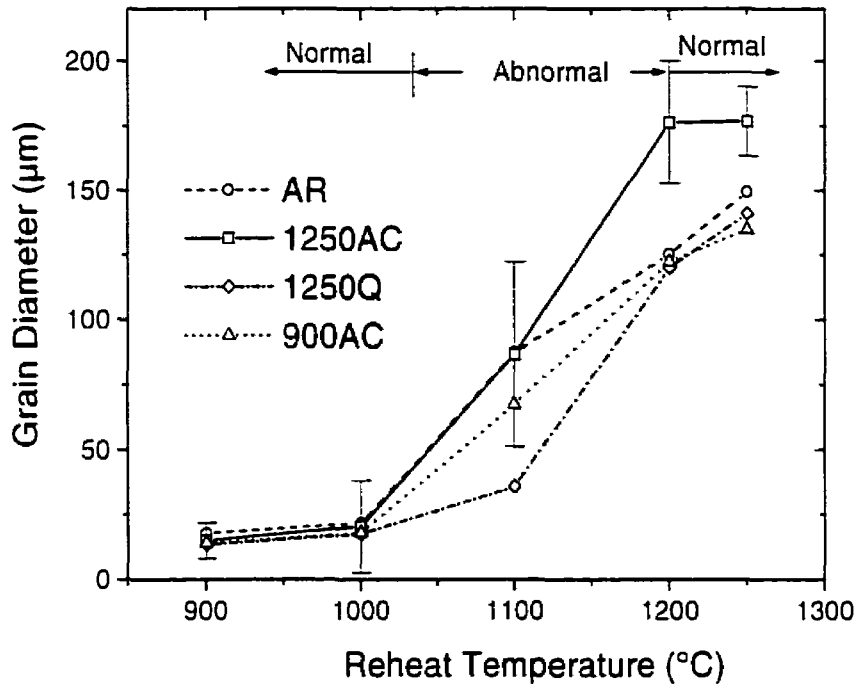


Figure 5.3 Variation in mean grain diameter with reheat temperature for four different initial microstructures.

5.3 Precipitate Evolution

Typical precipitate distributions of 1141Nb in the as-rolled bar are shown in Figure 5.4(a,b). Similar to the precipitates of 1541Nb, it contained a high density of small precipitates, both in primary ferrite and pearlite. Most precipitates were globular. The precipitates were not uniformly distributed in the microstructures. EDS analysis indicated that these precipitates were Nb-rich. They were thus taken to be Nb(C,N). Some large globular MnS precipitates were also found in the microstructure.

The density of precipitates decreased with increasing preheat temperature, indicating that some of the precipitates (especially small ones) had dissolved. After 1250°C preheat,

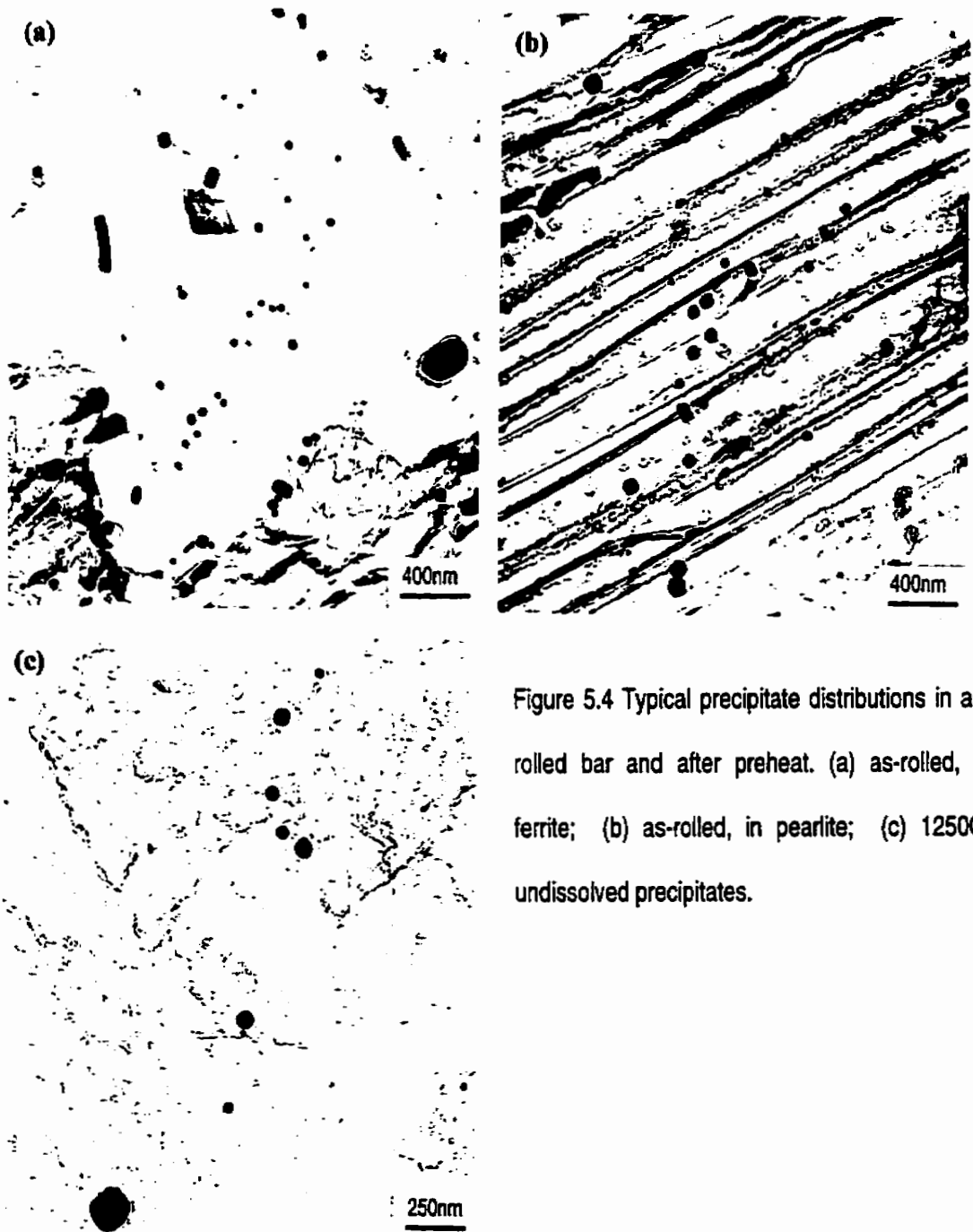


Figure 5.4 Typical precipitate distributions in as-rolled bar and after preheat. (a) as-rolled, in ferrite; (b) as-rolled, in pearlite; (c) 1250Q, undissolved precipitates.

only some large precipitates remained undissolved (Figure 5.4c).

Figure 5.5 (a-c) shows the precipitate evolution during preheat and reheat. The as-rolled sample had bimodal precipitate size distributions. With the increase of reheat temperature, the smaller precipitates shrank and finally disappeared when the temperature was higher than 1100°C, and bimodal distributions changed into unimodal. More large precipitates ($d > 200\text{nm}$) were observed when the reheat temperature was $> 1200^\circ\text{C}$, indicating that precipitate coarsening occurred when the temperature was high enough.

Unimodal precipitate distribution was found after 1250Q preheat, while bimodal distribution was observed after 1250AC. The change of precipitate distribution indicated that precipitation occurred during the slow cooling process of the preheat treatment, which produced a large amount of small precipitates.

The precipitate evolution of 1250AC samples during reheat was very similar to that of the as-rolled samples. The small-diameter peak disappeared with increasing reheat temperature, and the precipitate distributions changed from bimodal to unimodal. The only difference was the larger precipitate sizes in 1250AC samples.

The evolution of precipitate size distribution in 1250Q samples was unique compared with the others. The distribution at the initial condition was unimodal (rather than bimodal) with a peak at around 100nm (diameter). A large amount of small precipitates was found when reheated to 900°C and 1000°C (Figure 5.6), and the distributions changed to bimodal (Figure 5.5c). This shows that precipitation occurred in the super-saturated austenite during reheat. At higher reheat temperatures, the small diameter peak gradually decreases and disappeared, and the distribution changed back to unimodal. This shows that the precipitated small precipitates redissolved at higher temperatures.

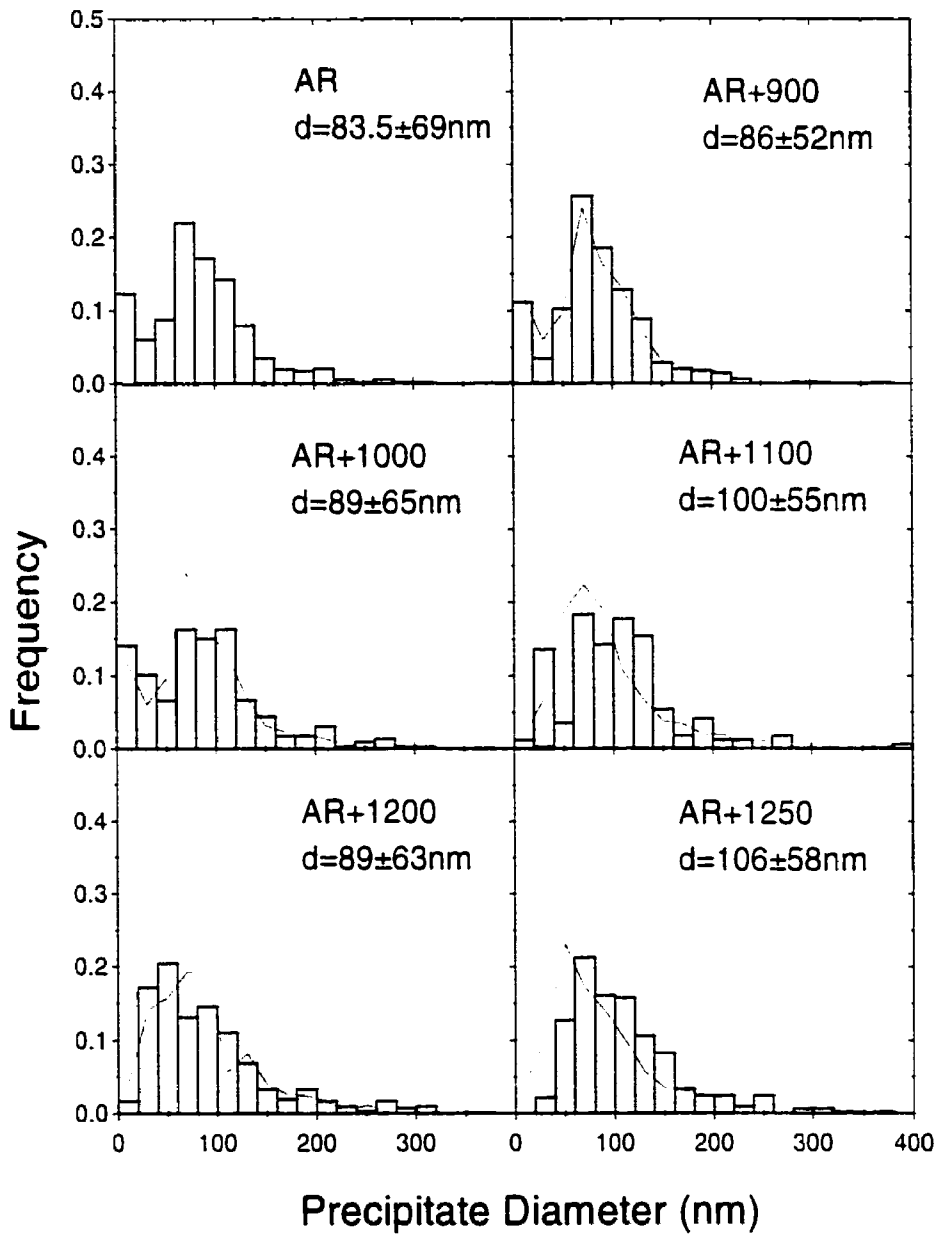


Figure 5.5a Evolution of precipitate size distributions during reheat for as-rolled conditions.

Histograms of experimental measurements are compared with model prediction.

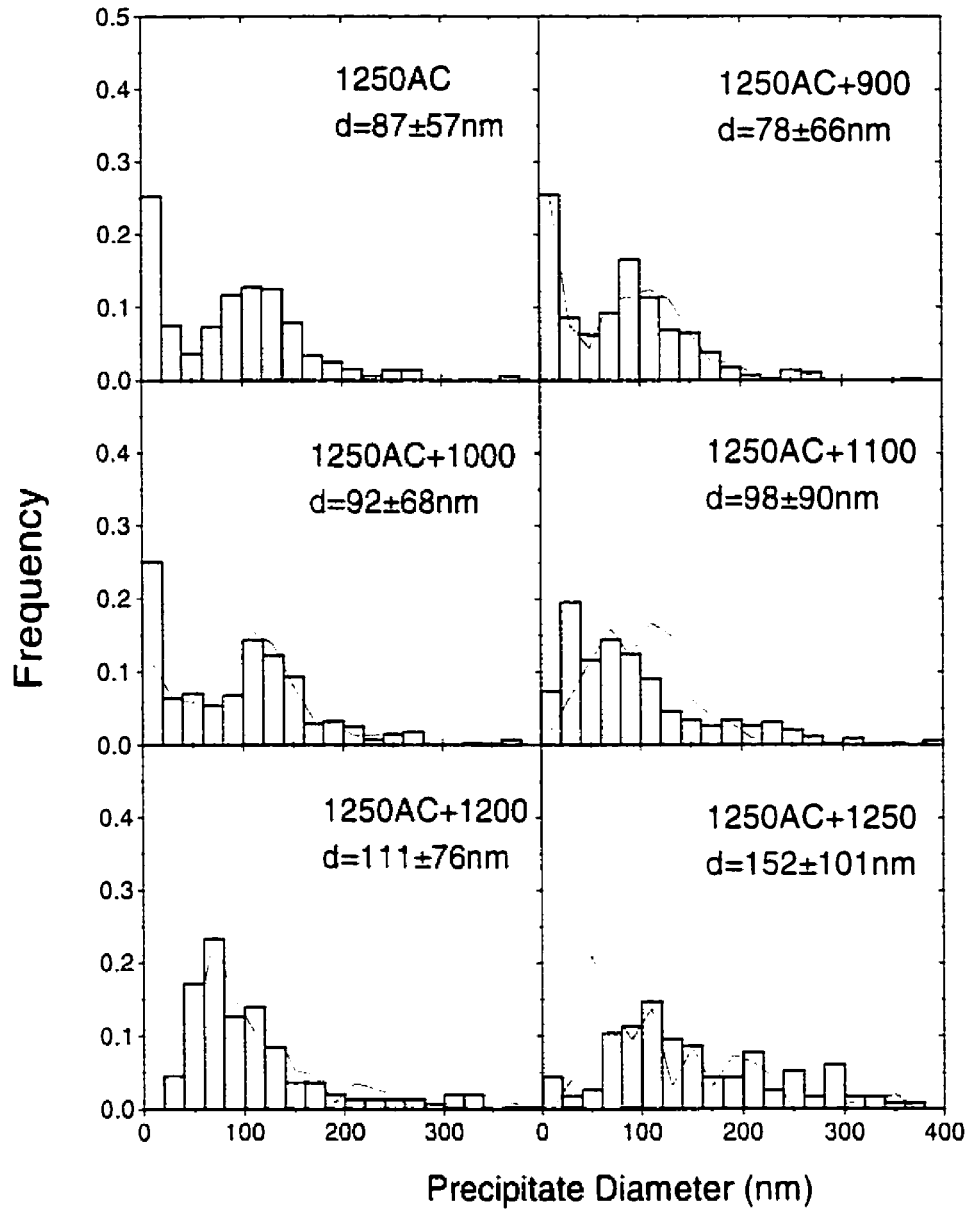


Figure 5.5b Evolution of precipitate size distributions during reheat for 1250AC conditions.

Histograms of experimental measurements are compared with model prediction.

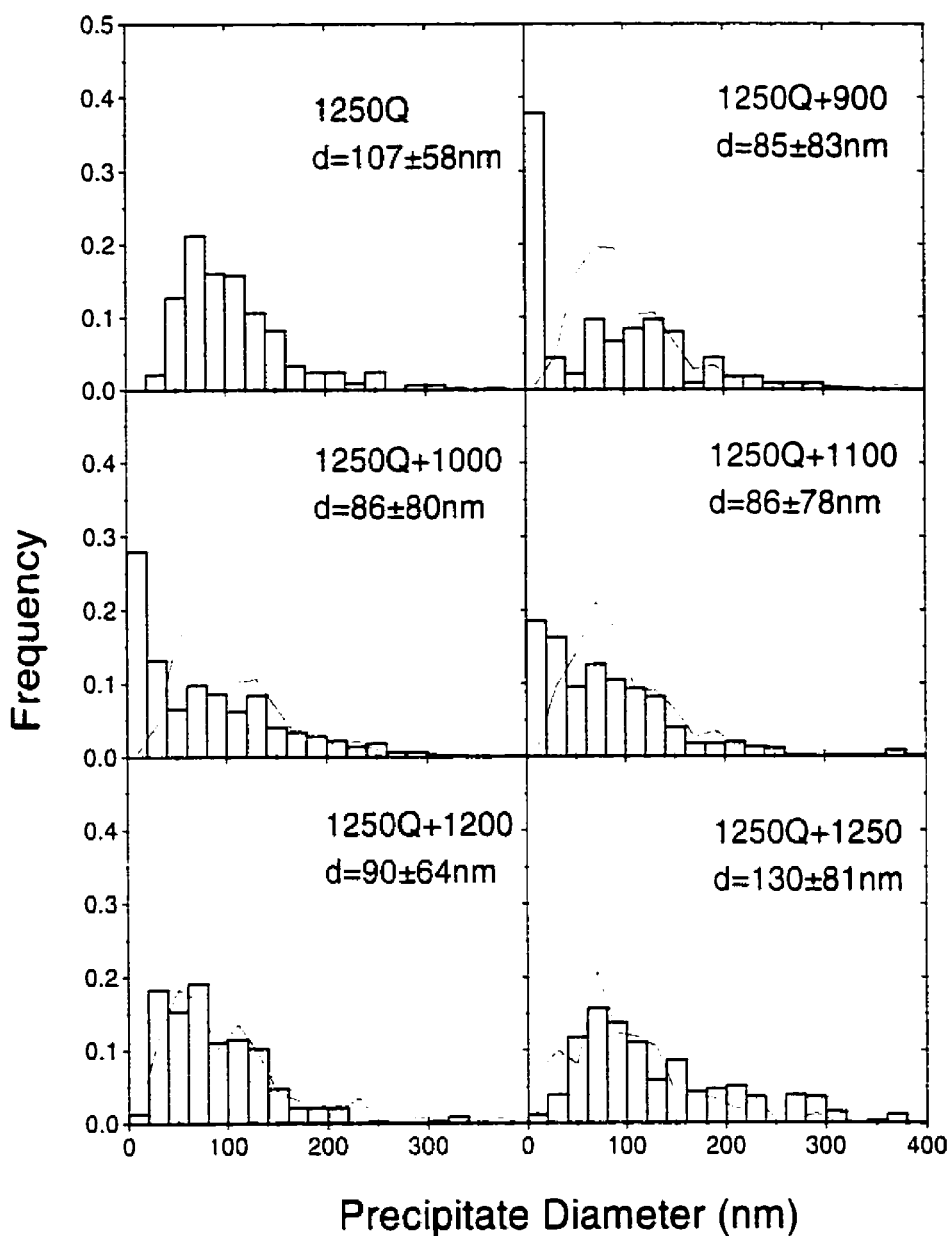


Figure 5.5c Evolution of Precipitate size distributions during reheat for 1250Q condition.

Histograms of experimental measurements are compared with model prediction.

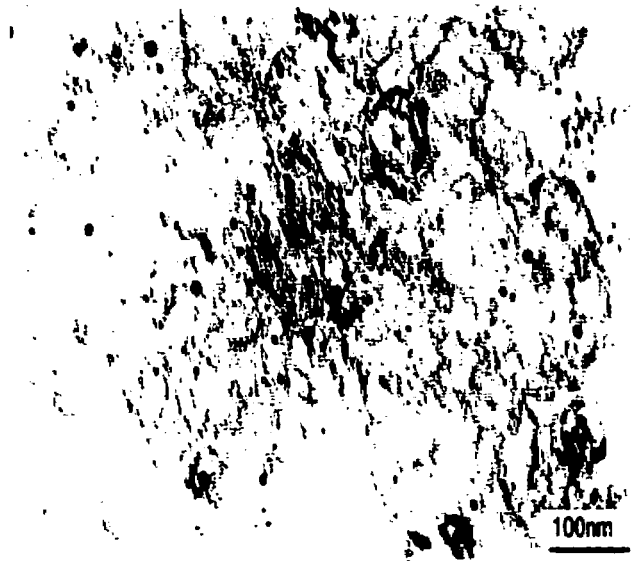


Figure 5.6 Large amount of reprecipitated precipitates after 1250Q+1000°C reheat.

5.4 Discussion

Figure 5.7 illustrates the precipitate evolution during the preheat and reheat cycles. Preheat treatments not only change the optical microstructures, but also the precipitate distributions. 1250Q changes precipitate size distribution from bimodal into unimodal and produces supersaturated austenite. The supersaturated austenite provides a chemical driving force for precipitation and favorable nucleation sites, therefore, reprecipitation occurs in a certain temperature range (900-1000°C) during induction reheat, which produces a large amount of small precipitates. The precipitate distribution changes from unimodal into bimodal. The high density of precipitates provide high pinning force on grain boundary migration, resulting in smaller grain sizes at the intermediate temperature range.

The supersaturation decreases with the process of precipitation and the increase of temperature. Finally, supersaturation does not exist and precipitate dissolution becomes

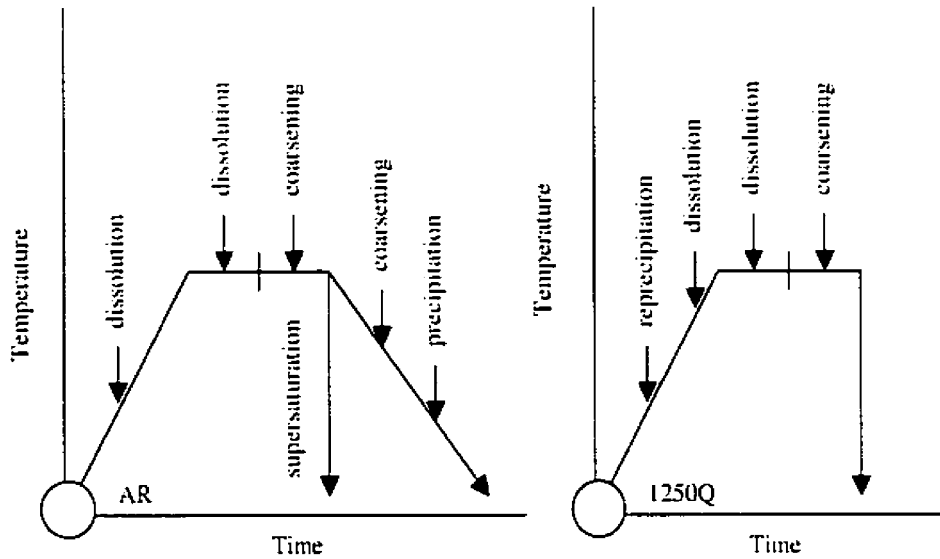


Figure 5.7 Schematic of precipitate evolution from different initial microstructures. (a) from as rolled condition, (b) from 1250Q.

the dominant mechanism during further induction reheat. The reprecipitated precipitates redissolve quickly because of their small size. Therefore, the precipitate distribution changes from bimodal into unimodal, and grain size increases quickly because of decreased precipitate pinning.

1250AC does not change the pattern of precipitate size distribution, but produces some coarsened precipitates, resulting in larger austenite size during reheat, especially at high temperatures. The precipitates in 900AC samples have not been measured because no significant change is expected from the as-rolled condition.

The precipitate dissolution-coarsening model given in §4.5 was also applied to the precipitate evolution of 1141Nb during induction reheat following a Welland Forge heating cycle. The precipitates measured in the as-rolled or preheated samples were used as initial conditions. The calculated precipitate size evolutions during induction reheat

were compared with the experimental measurements, as shown in Figure 5.5 (a-c). For AR and 1250AC samples, the calculations give good agreement with the observations, although both the materials and the heating cycle were different.

The model does not take reprecipitation into account during induction reheat, therefore, it does not predict the appearance of the reprecipitated carbonitrides in the 1250Q samples at intermediate temperatures. But it does predict the precipitate size distribution at temperatures higher than 1200°C when the reprecipitated precipitates redissolve.

The grain growth model given in §4.6 and §4.7 was also applied to the grain growth of 1141Nb following the Welland Forge cycle. The calculated mean grain diameters as a function of reheat temperature and holding time are compared with the measured values in Figure 5.8. The modeled results give good with experimental observations for the as-rolled and slowly cooled samples. It proves that 1250AC, which has larger precipitate sizes, would give coarsened grain sizes during reheat. Again, the reprecipitation was not included in this model. It does not predict the smaller grain sizes in the intermediate temperature range for the 1250Q pretreatment.

This study explained the interesting phenomenon observed by Welland Forge, as was mentioned in §1. The larger grain sizes following preheat + slow cooling treatment are the result of coarsened precipitate sizes during preheat cycle, while the smaller grain sizes following preheat + water quench treatment are caused by the reprecipitation from supersaturated austenite. Therefore, the unused billets after induction heating should be quenched to avoid coarsened grain sizes.

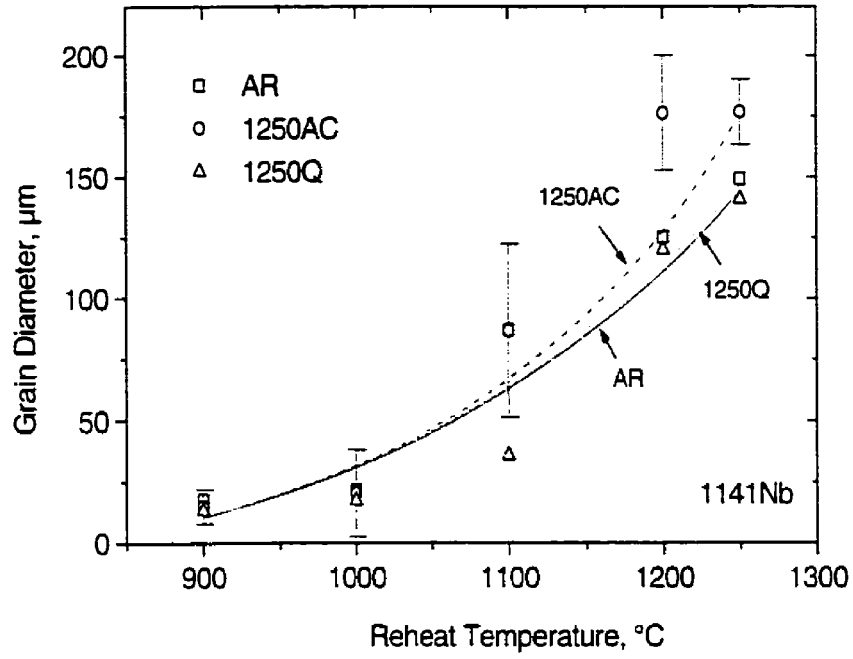


Figure 5.8 Variation in grain diameter with temperature and holding time (Welland Forge cycle).

Data points are measured values and the lines are calculated from the grain growth model.

Chapter 6. Recrystallization After Hot Deformation

6.1 Stress-strain curves during deformation

The true stress-true strain curves during deformation after various holding times at different temperatures are shown in Figures 6.1 and 6.2. Deformation stresses increased monotonically with deformation strain, showing that dynamic recrystallization did not occur during deformation. Generally, deformation stress decreased with increasing temperature and holding time. This pattern was followed until strain-induced precipitation occurred. Strain-induced precipitates caused significant precipitation strengthening, resulting in higher deformation stresses. This can be observed from the stress-strain curves of 1541Nb at 950°C (Figure 6.1c) and 1541VTi at 850°C (Figure 6.2c).

6.2 Recrystallization fraction and softening fraction

Figure 6.3 shows the softening fractions (closed symbols) and recrystallization fractions (open symbols) for various holding times and temperatures. The solid lines are fitted curves based on the softening data at each of the deformation temperatures. Rearranging the Avrami equation (Equation 2.32), we have

$$\log \ln \left(\frac{1}{1-f_s} \right) = \log B + k_n \log t \quad [6.1]$$

A linear curve can be obtained by plotting $\log \ln[1/(1-f_s)]$ vs. $\log t$, and the Avrami constant can be determined from the slope.

Typical S-type softening was observed at 950-900°C in 1541VTi, and 1050-1000°C in 1541Nb. The observed recrystallization fractions agree reasonably well with softening fractions at these temperatures, and the softening kinetics could be well described by the

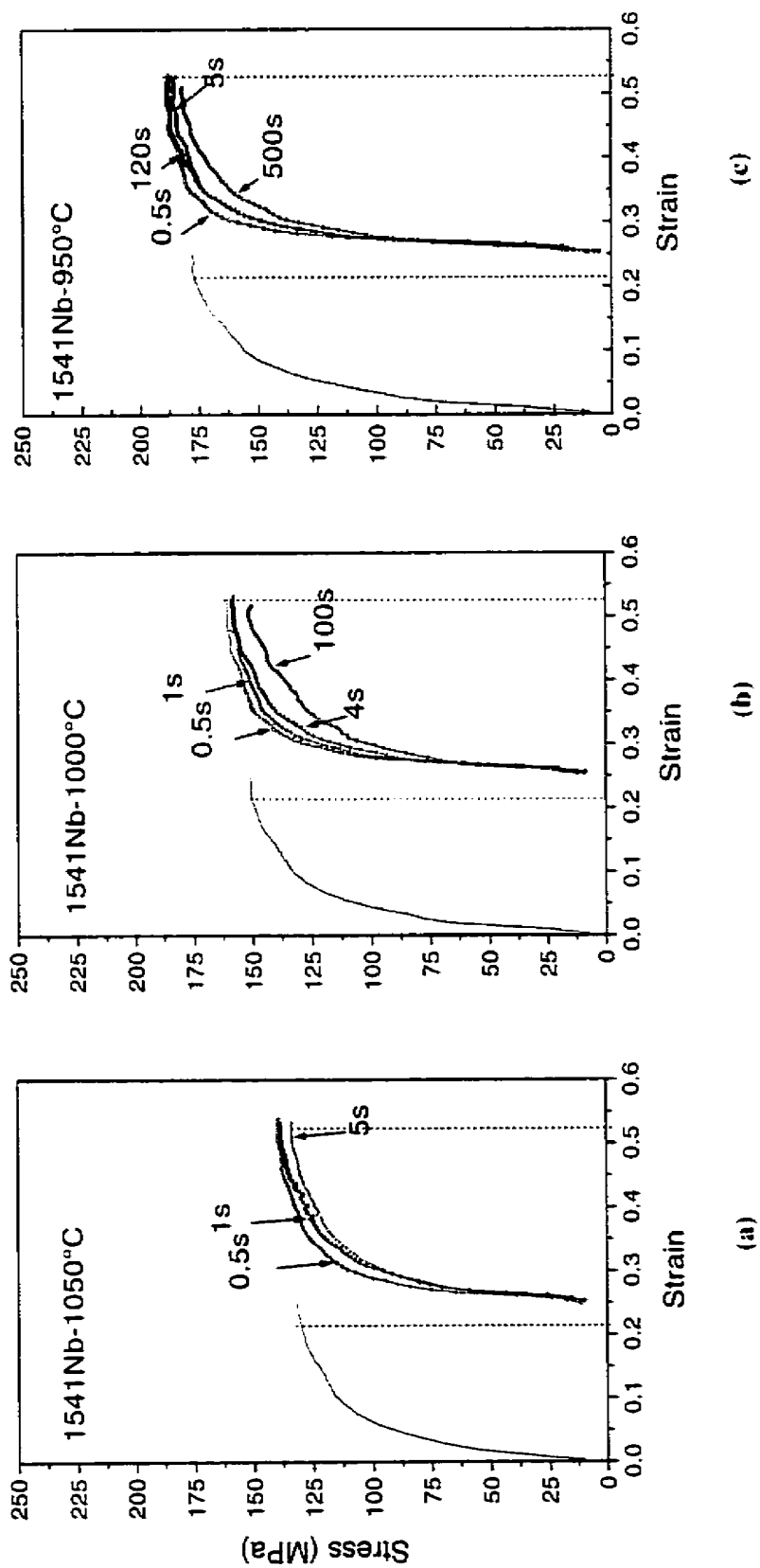


Figure 6.1 True stress-true strain curves for different temperatures and holding times (1541Nb).

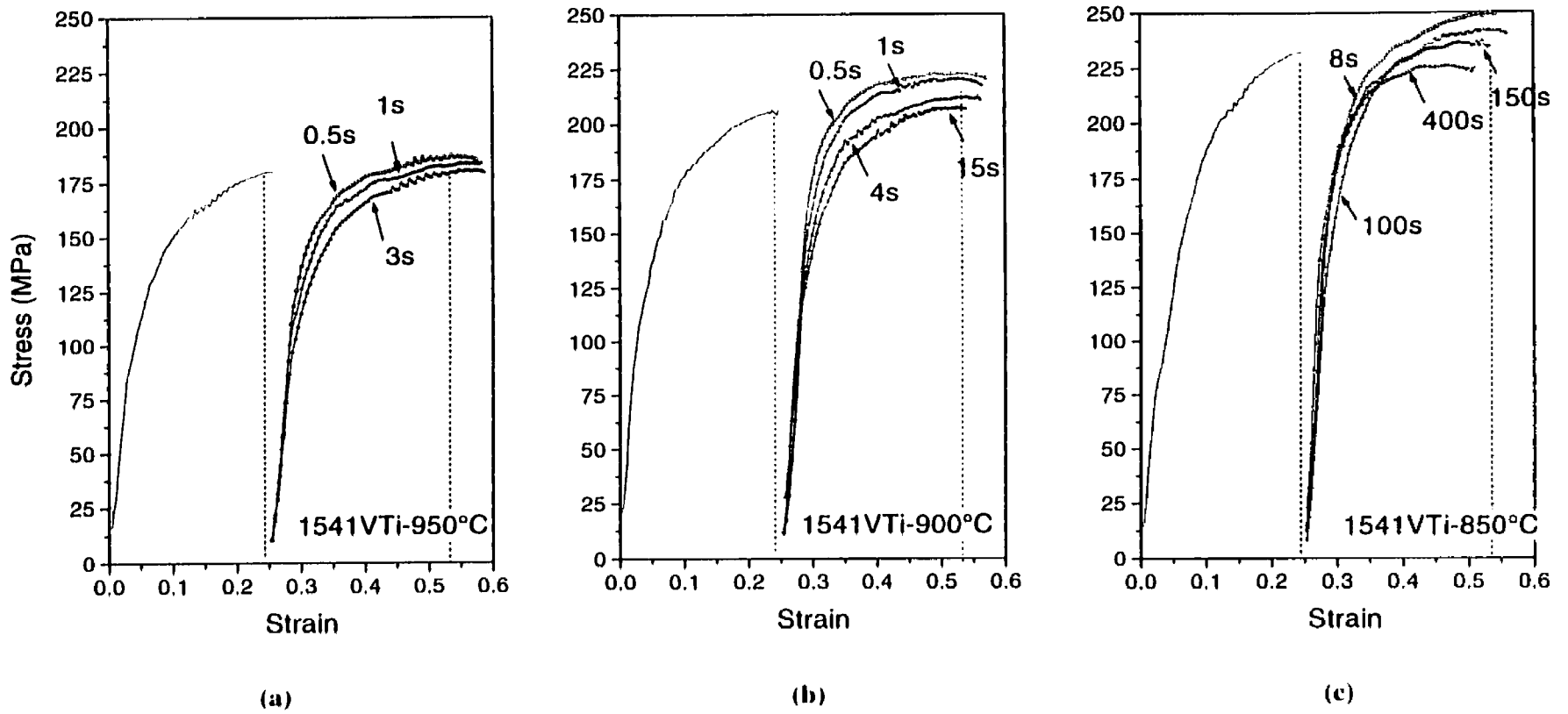


Figure 6.2 True stress-true strain curves for different temperatures and holding times (1541VTi).

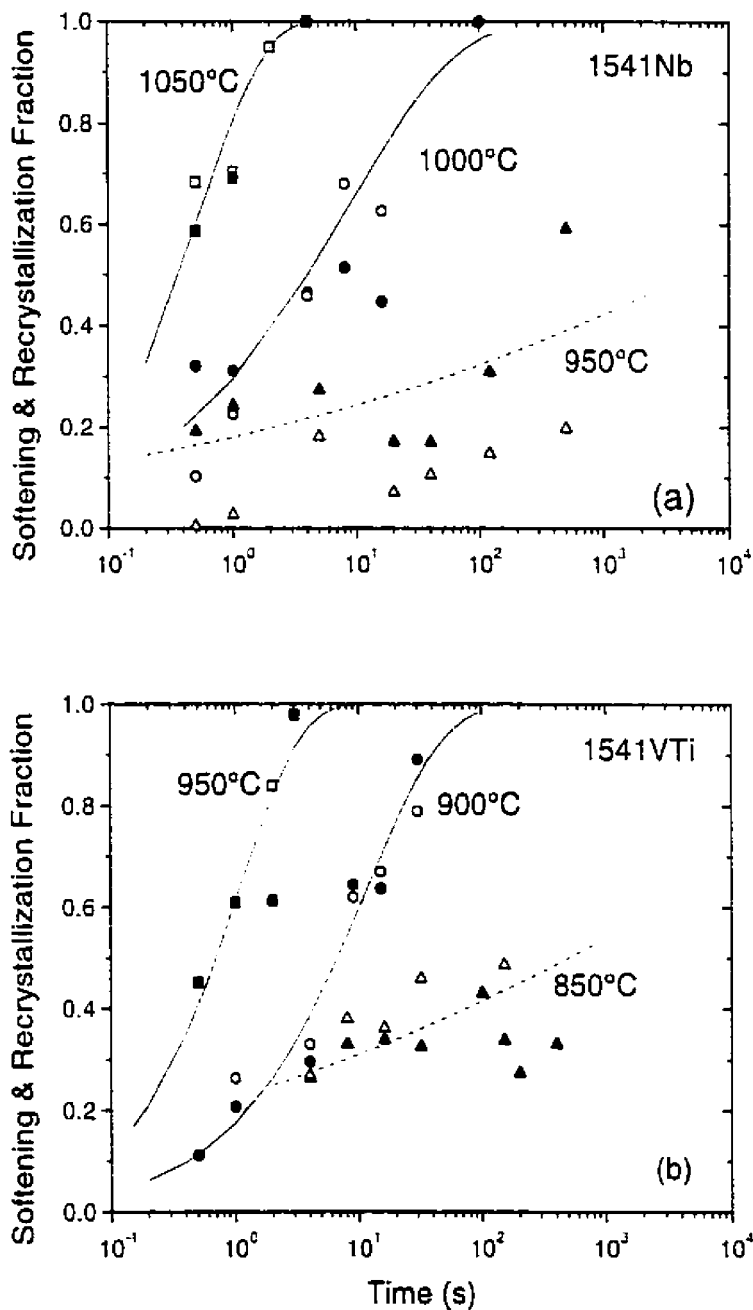


Figure 6.3. Softening fraction (closed symbols) and recrystallization fraction (open symbols) vs. interruption time from double-hit and single hit tests. The curves are plotted by fitting to the Avrami equation. (a) 1541Nb and (b) 1541VTi.

Avrami equation. A difference between the softening fraction and the recrystallization fraction was observed after deformation at lower temperatures. The softening fraction increased initially with longer holding time, but a decrease of softening fraction has been found after holding for a period. Typical S-type softening was no longer followed in this case, and could not be fitted to the Avrami equation. The discontinuous softening behavior after deformation at lower temperatures was associated with strain-induced precipitation.

It was also found that softening fractions could not be extended to zero (typically larger than 0.1). These phenomena indicated that some of the softening was provided by recovery rather than recrystallization.

6.3 Microstructural observation

The initial austenite grain sizes were 120 μm for 1541Nb after 1200 $^{\circ}\text{C}$ reheat, and 112 μm for 1541VTi after 1260 $^{\circ}\text{C}$ reheat.

The evolution of the austenite microstructure after deformation was determined from the quenched samples, which had been held for different times after the first deformation. Typical deformed microstructures are shown in Figures 6.4 and 6.5. In addition to pancaked austenite grains, deformation bands were observed in some large austenite grains. Recrystallized grains nucleated predominantly at austenite grain boundaries, especially in 1541Nb. The elongated MnS inclusions did not appear to have any effect on recrystallization.

Figure 6.6 shows the measured mean grain diameter plotted against the recrystallization fraction. Grain size initially decreased with increasing recrystallization

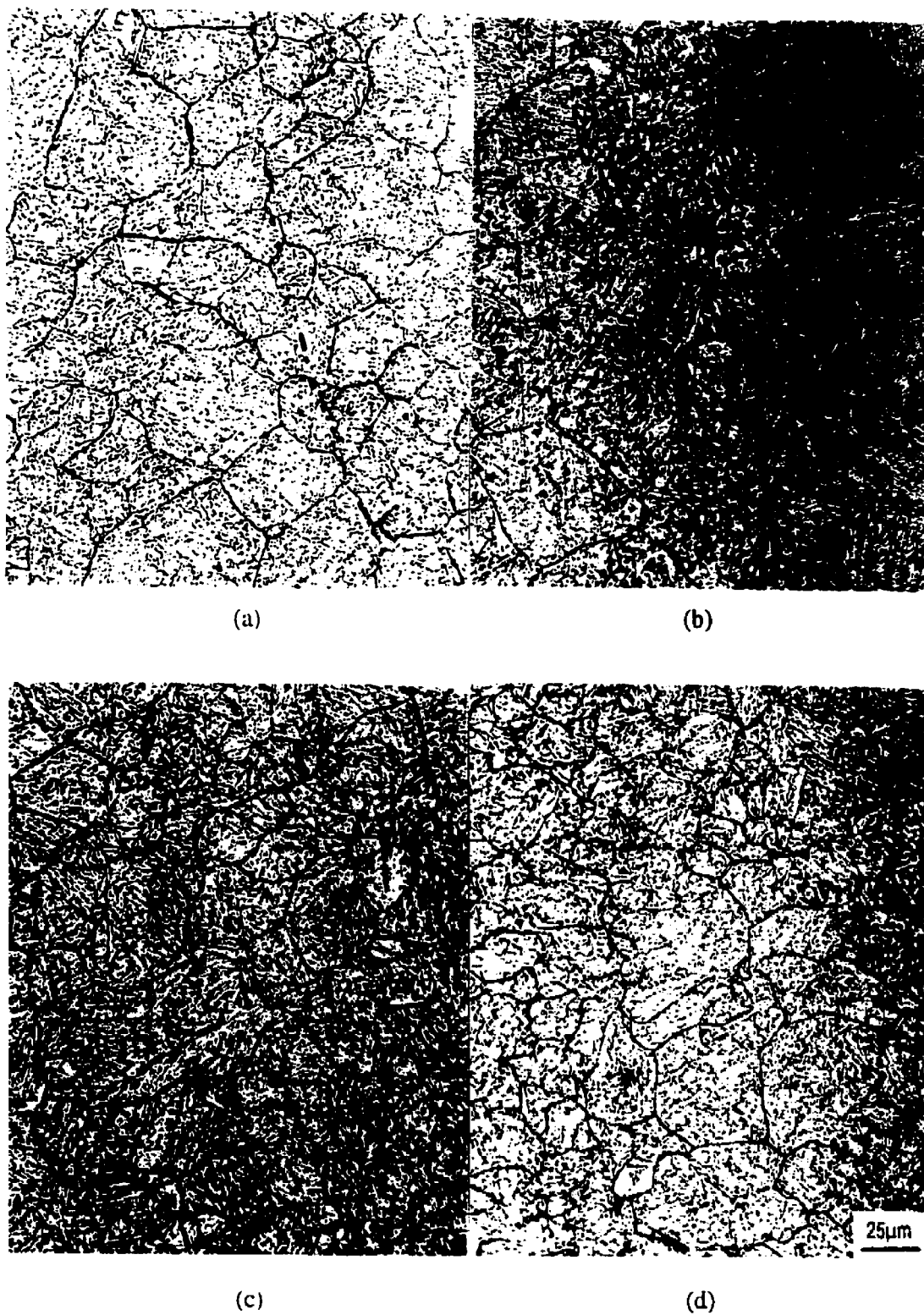
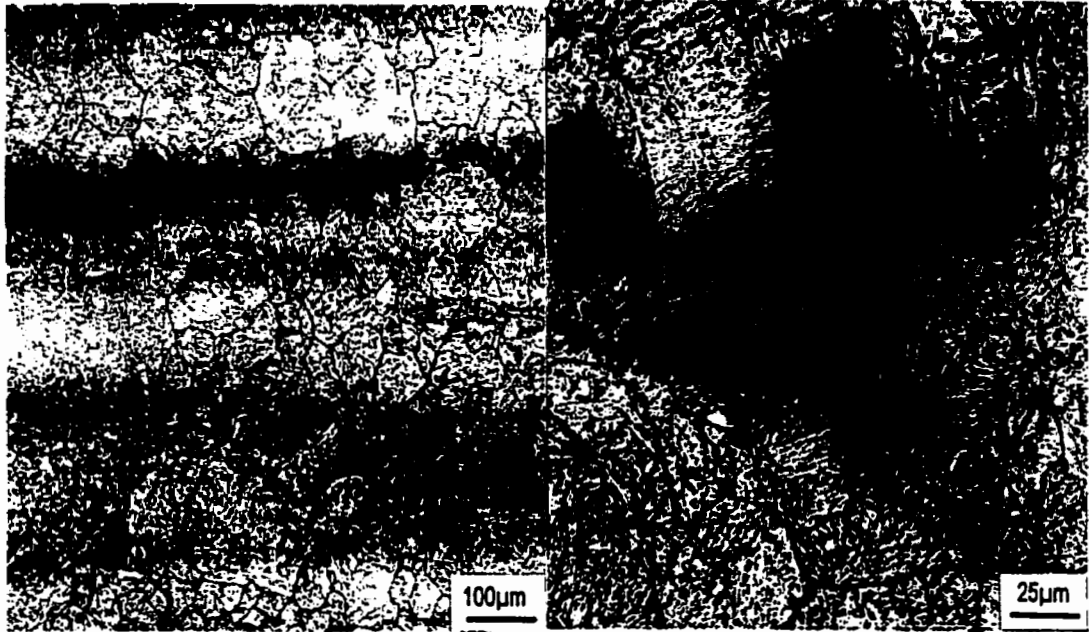
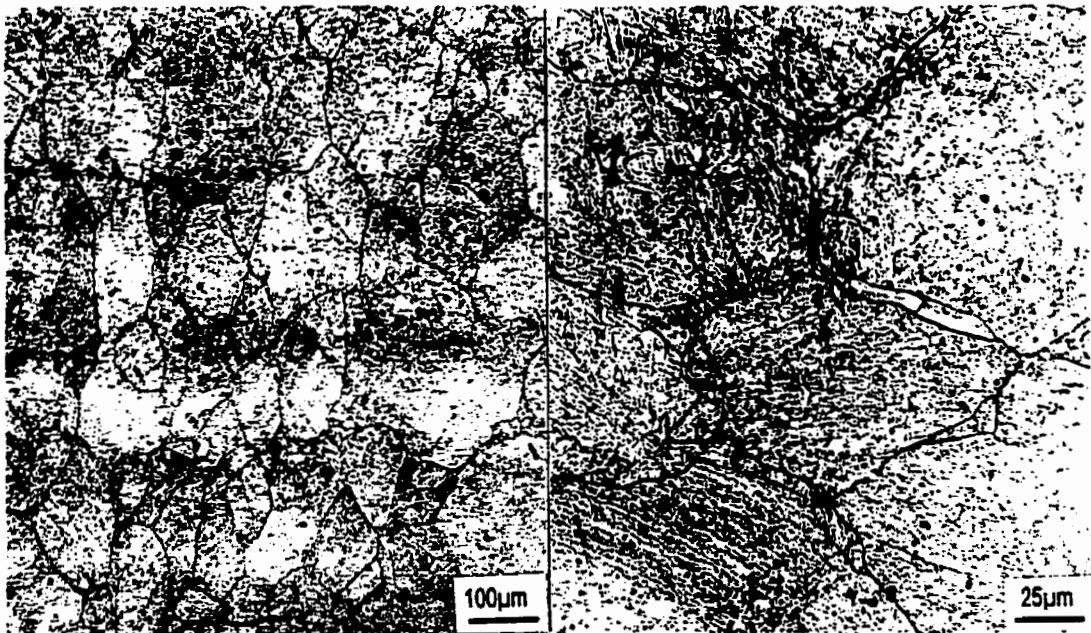


Figure 6.4. Typical austenite microstructure of 1541VTi after deformation at 900°C. (a) 0.5s hold, (b) 1s hold, (c) 4s hold and (d) 9s hold.



(a) 1541VTi, 850°C, 16s

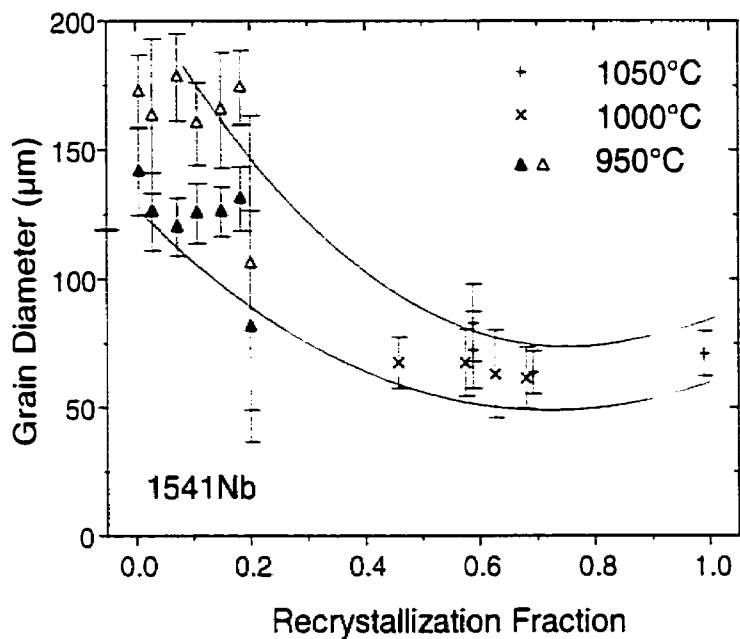
(b) 1541VTi, 850°C, 16s



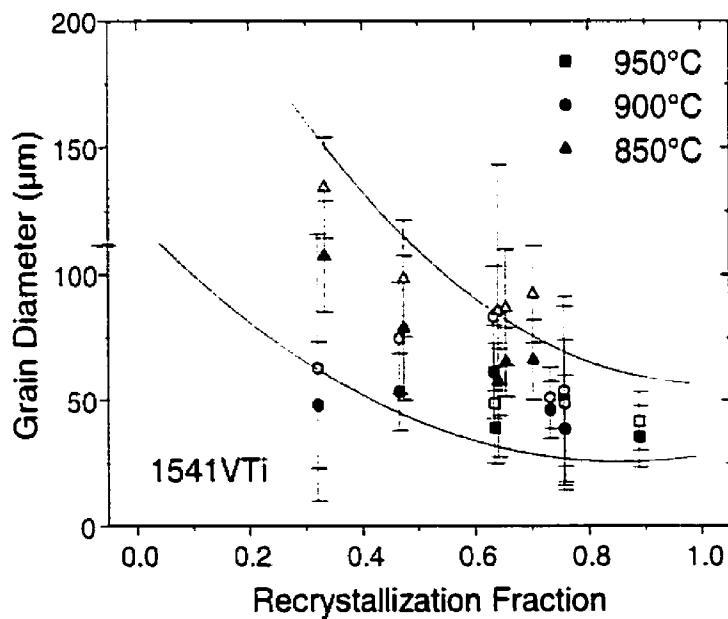
(c) 1541Nb, 950°C, 0.5s

(d) 1541Nb, 950°C, 0.5s

Figure 6.5 Typical austenite microstructure after hot deformation. (a) Partially recrystallized microstructure. (b) Deformation band. (c) Partially recrystallized microstructure. (d) Recrystallized grains along grain boundaries.



(a)



(b)

Figure 6.6 Variation of austenite grain sizes with recrystallization fraction. Solid and open symbols are measured from transverse and longitudinal directions respectively. (a) 1541Nb (b) 1541VTi.

fraction. This tendency continued until recrystallization was nearly finished. Then grain sizes slightly increased with increasing recrystallization. This was caused by the coarsening of the recrystallized grains.

The grain size for complete recrystallization (D_r) was determined by extending the measured curves to $f_r=1$. The values obtained were $\sim 35\mu\text{m}$ for 1541VTi and $\sim 60\mu\text{m}$ for 1541Nb, respectively. Comparing these values with the empirical equations for Ti-V and Nb steels (Table 2.8), it was found that they were close to the predictions given by Roberts *et al.* (1983) and Sellars and Whiteman (1979).

Typical precipitate distributions before and after deformation are shown in Figure 6.7. The precipitates in 1541VTi were mainly cuboids after reheat at 1260°C , which were shown by EDS to be Ti-rich, with a Ti/V ratio about 5.6. Large, globular precipitates were found in 1541Nb after 1200°C reheat.

A large amount of small ($<50\text{nm}$) globular precipitates was observed in those samples where strain-induced precipitation occurred, especially 1541Nb. For 1541VTi, EDS indicated that these precipitates were also mixed Ti and V, but the Ti/V ratio was about 1.8, lower than that after reheat.

Precipitate size distributions for various treatments are shown in Figure 6.8. The distributions were unimodal before strain-induced precipitation occurred. A large amount of small precipitates formed in 1541Nb during strain-induced precipitation, and the precipitate distribution changed into bimodal. Some smaller precipitates were also observed in 1541VTi during strain-induced precipitation, but the effect was not as large as in 1541Nb.

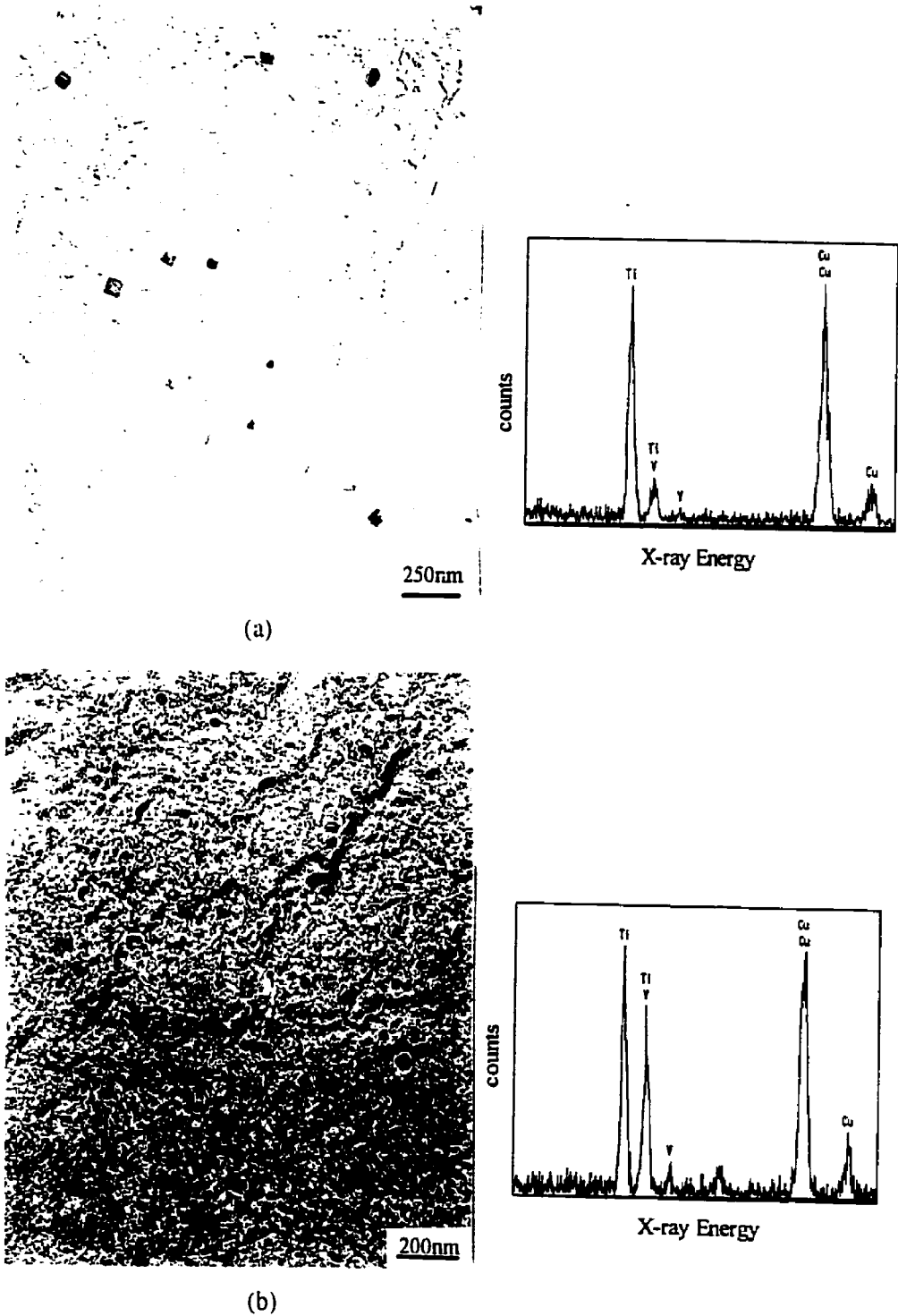


Figure 6.7 Precipitate distribution in 1541VTi. (a) Undissolved precipitates after 1260°C reheat, (b) strain-induced precipitates after deformation (150s hold at 850°C).

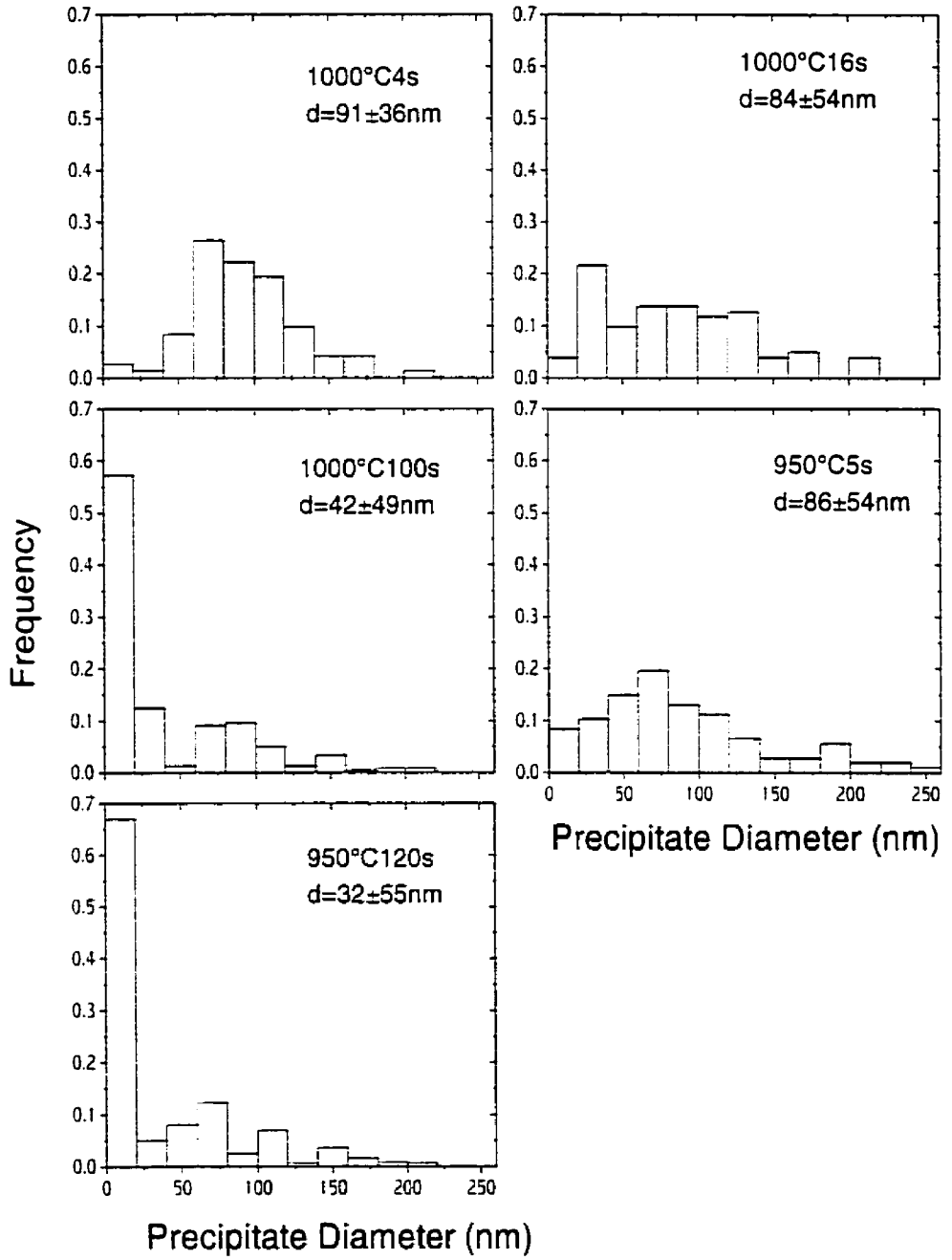


Figure 6.8a Typical precipitate size distributions after deformation (1541Nb).

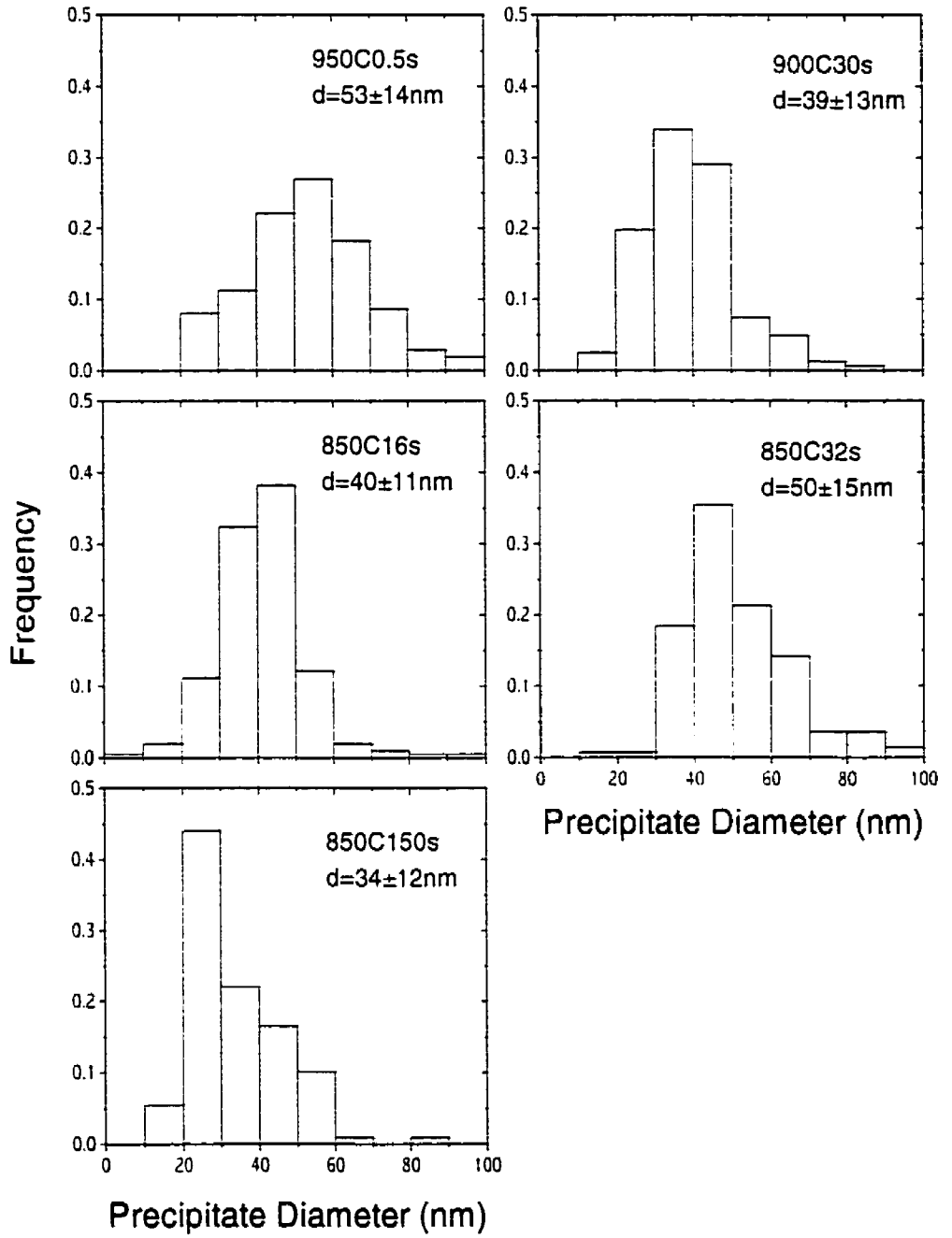


Figure 6.8b Typical precipitate size distributions after deformation (1541VTi).

6.4 Modeling Recrystallization Kinetics

The k_A values determined from equation 6.1 were 0.86, 0.68 and 0.16 respectively for 1541VTi at 950, 900 and 850°C, and 0.91, 0.49 and 0.15 for 1541Nb at 1050, 1000 and 950°C. It is seen that the Avrami constant decreases with decreasing temperature. This has been attributed to the segregation of microalloyed elements, which increases with decreasing temperature (Kwon and DeArdo, 1986; Medina *et al.*, 1994). The fitted curves following this method have been given in Figure 6.3.

The limitation of the fitted curves is that they have been done *individually* at each temperature. The only variable was time. The effects of temperature and composition were not taken into account. It is more desirable that a unified equation be developed which reflects the effects of composition, temperature and time, similar to the empirical equations given in Table 2.8.

From the Avrami equation (Equation 2.33), the recrystallization fraction can be given as

$$f_x = 1 - \exp\left\{\ln(1-X)\left(\frac{t}{t_x}\right)^{k_A}\right\} \quad [6.2]$$

The recrystallization kinetics can be determined after the determination of the two parameters, k_A and t_x .

The first step is to determine t_x . Following the suggestion given by Sellars *et al.* (1986, Equation 2.36)

$$t_{0.05} = t_{0.05}^{C-Mn} \exp\left\{[X]\left(\frac{p_2}{T} - q_2\right)\right\} \quad [6.3]$$

A linear curve is obtained by rearranging Equation 6.3. The values of the constants (p_2

and q_2) can be determined from the slope and intersection, as is shown in Figure 6.9. For this fitting, the recrystallization-start time of plain carbon steel ($t_{0.05}^{C-Mn}$) as given by Sellars *et al.* (Table 2.7) was used, and the solute concentration ($[X]$) was calculated from the solubility products. The obtained empirical equations for $t_{0.05}$ are:

$$\text{For 1541VTi: } t_{0.05} = t_{0.05}^{C-Mn} \exp\left\{[Ti]\left(\frac{1.26 \times 10^{18}}{T} - 12.060\right)\right\} \quad [6.4a]$$

$$\text{For 1541Nb: } t_{0.05} = t_{0.05}^{C-Mn} \exp\left\{[Nb]\left(\frac{3.56 \times 10^7}{T} - 3.150\right)\right\} \quad [6.4b]$$

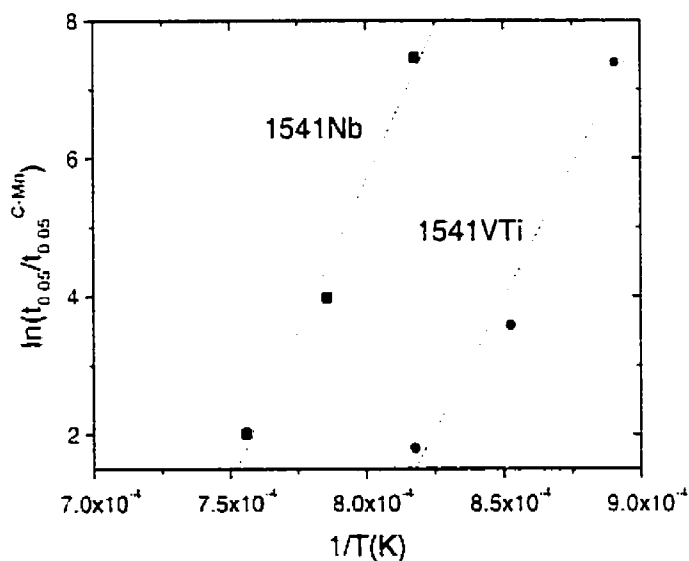


Figure 6.9 Determining the constant values in Equation 6.3.

The second step is to determine the Avrami constant k_A . It has been found that k_A varies with deformation temperature. Medina *et al.* (1994) suggested that this could be estimated by an exponential equation

$$k_A = q_3 \exp \frac{p_3}{RT} \quad [6.5]$$

where p_3 and q_3 are constants. Again, by using plotting $\ln k_A$ vs. $1/T$, a linear curve can be obtained and the values of the constants determined (Figure 6.10). The obtained empirical equations for k_A are:

$$\text{For 1541VTi: } k_A = 1.02 \times 10^3 \exp\left(-\frac{187,500}{RT}\right) \quad [6.6a]$$

$$\text{For 1541Nb: } k_A = 1.80 \times 10^9 \exp\left(-\frac{235,000}{RT}\right) \quad [6.6b]$$

With the constants determined above, the softening curves at different temperatures can be fitted, as is shown in Figure 6.11. The empirical equations predict recrystallization kinetics well in absence of strain-induced precipitation.

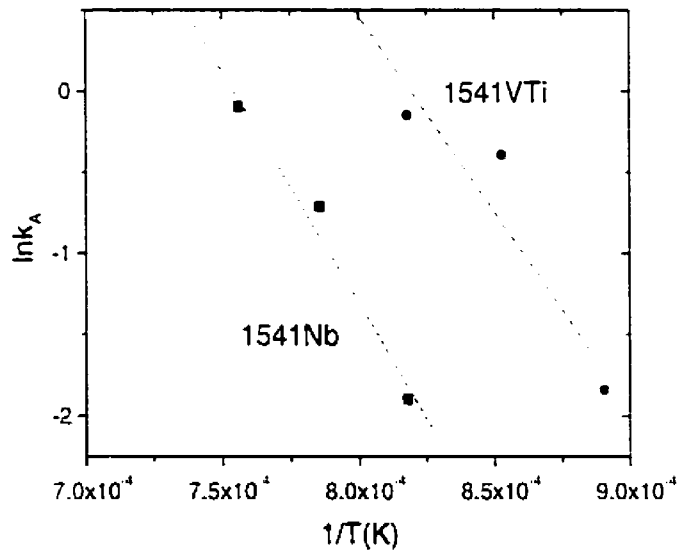


Figure 6.10 Determining the constant values in Equation 6.5.

6.5 Modeling Strain-Induced Precipitation

It is clear that strain-induced precipitation has a large effect on recrystallization behaviour when it occurs. A large amount of small precipitates increases the flow stress

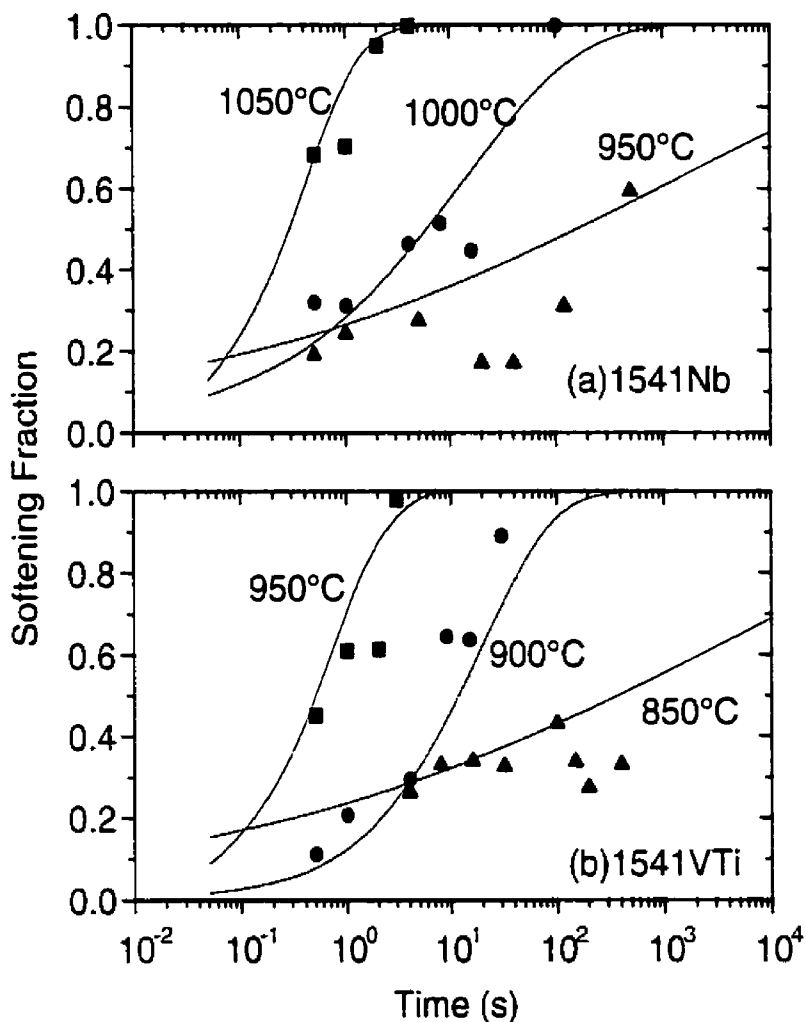


Figure 6.11 Softening fraction predicted by the unified model (lines) compared with experimental data. (a) 1541Nb and (b) 1541VTi.

by precipitate strengthening, and inhibits recrystallization softening by precipitate pinning. It is necessary to determine when strain-induced precipitation starts under a certain TMP condition. Obviously, it is a function of steel composition, deformation strain, and temperature.

For a given composition, the chemical driving force for carbide or carbonitride

precipitation can be determined from the supersaturation ratio of the alloy elements, as has been discussed in §2.6. In this study, this method has been further extended for complex carbonitrides like (Ti,V)(C,N). The derived chemical driving force for (Ti,V)(C,N) precipitation was given by:

$$\Delta G_{\text{chem}} = \frac{RT}{2V_m} \left\{ x \ln \frac{X_{\text{Ti}}^e}{X_{\text{Ti}}^0} + (1-x) \ln \frac{X_{\text{V}}^e}{X_{\text{V}}^0} + y \ln \frac{X_{\text{C}}^e}{X_{\text{C}}^0} + (1-y) \ln \frac{X_{\text{N}}^e}{X_{\text{N}}^0} \right\} \quad [6.7]$$

Where X_i^e and X_i^0 are the equilibrium and bulk concentrations of element i in austenite, respectively. V_m is the molar volume of the precipitate, and x and y are the atomic fraction of Ti and C in the precipitate $(\text{Ti}_x\text{V}_{1-x})(\text{C}_y\text{N}_{1-y})$. The detailed derivation is given in Appendix D.

The calculated chemical driving forces for Nb(C,N) precipitation in 1541Nb and (Ti,V)(C,N) precipitation in 1541VTi are given in Figure 6.12. It is found that the chemical driving force for Nb(C,N) precipitation increases with decreasing temperature. It is surprising, however, that the driving force for (Ti,V)(C,N) precipitation does not increase monotonically with decreasing temperature, but displays 2 extremes. This unexpected phenomenon has been attributed to the conventional assumption that the nucleus has the same composition as the bulk precipitate in equilibrium with the matrix at the holding temperature (Liu and Jonas, 1988). To modify this situation, it is suggested that the Ti content in the nucleus is the same as that in austenite during austenization. After this modification, the 2 extremes disappear and the chemical driving force for (Ti,V)(C,N) precipitation decreases monotonically with decreasing temperature.

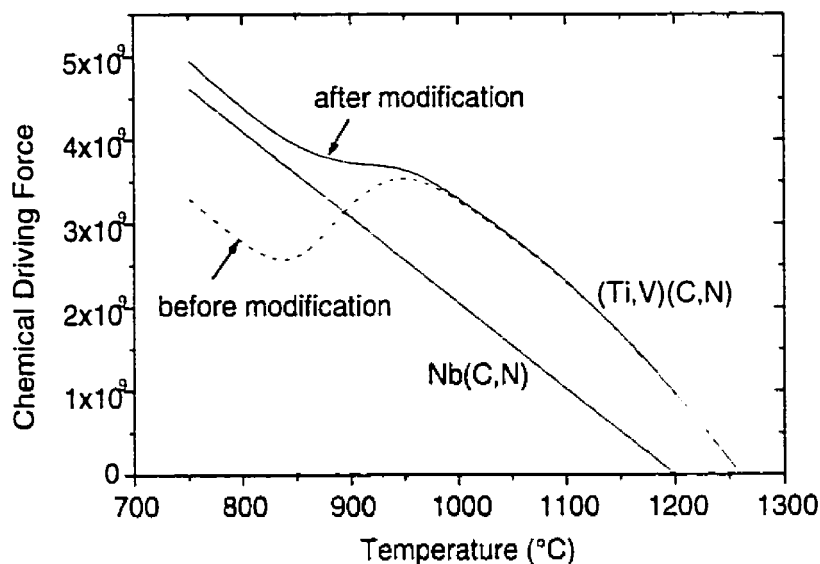


Figure 6.12 Chemical driving force of $(Ti,V)(C,N)$ in 1541VTi and $Nb(C,N)$ in 1541Nb. The solid and broken lines for 1541VTi are before and after modification, respectively.

The precipitation-start time was calculated with the classic nucleation theory. The basic procedure includes: (1) calculate the solute concentration at reheat and deformation temperatures from the solubility product, which has been discussed before; (2) calculate the chemical driving force, elastic energy and interfacial energy; (3) calculate the critical nucleus radius; (4) calculate nucleation rate of the precipitate; and finally (5) calculate the time for 5% precipitation, i.e., precipitation-start time. The method for step one was given in §2.1, while the others were discussed in §2.5. Detailed calculation procedures are given in Appendix E. The related constants for this model have been selected as: $b=2.5 \times 10^{-10} \text{ m}$, $\gamma_i=0.50 \text{ J/m}^2$, $r_d=2 \times 10^{-10} \text{ m}$ and $\xi=0.40$, which are typical values from the literature (Dutta and Sellars, 1987; Liu and Jonas, 1988; Militzer *et al.*, 1992). The calculated precipitation-start time ($t_{0.05}^p$) are shown in Figure 6.13 by the dashed lines.

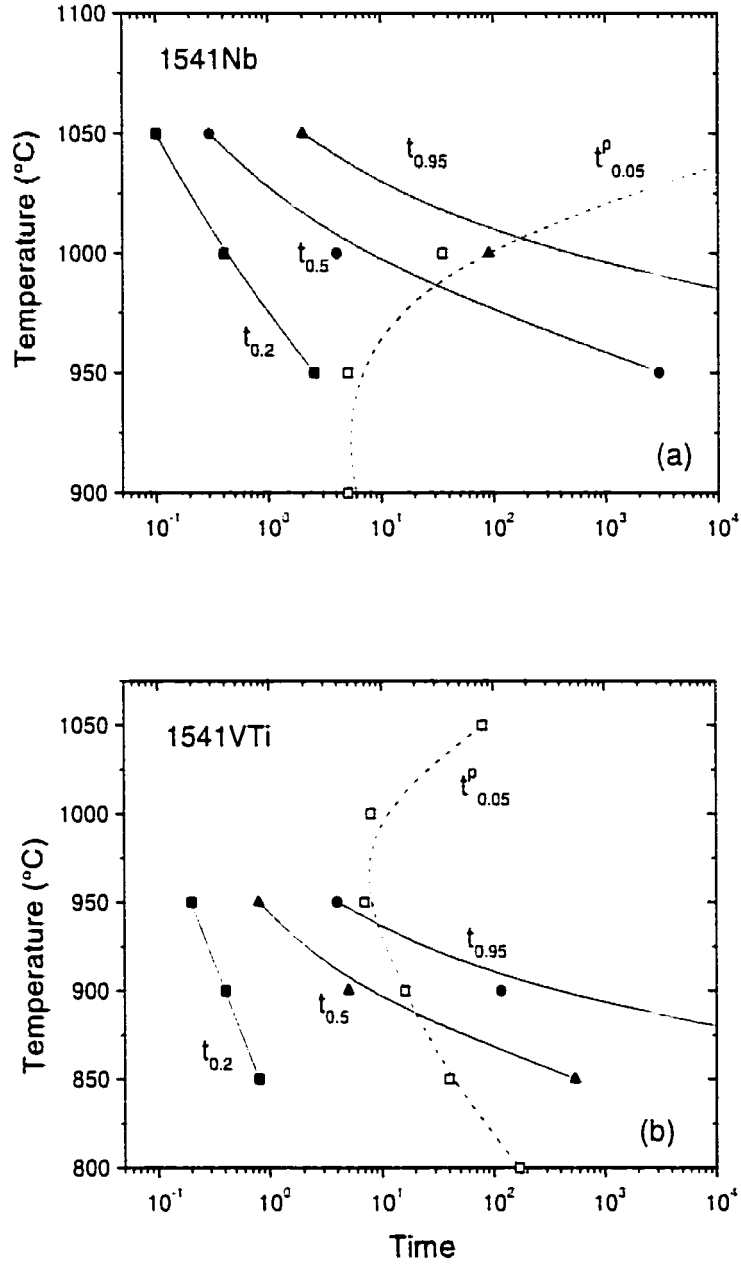


Figure 6.13 Static recrystallization curves and the start time for strain-induced precipitation. $t_{0.2}$, $t_{0.5}$ and $t_{0.95}$ refer to 20%, 50% and 95% softening time. $t_{0.05}^p$ refers to precipitation-start time. (a) 1541Nb and (b) 1541VTi.

The shortest precipitation time is at about 950°C for both 1541VTi and 1541Nb, with a $t_{0.05}$ approximately 10 seconds. At 950°C, the recrystallization rate for 1541VTi is much faster than precipitation, and recrystallization finishes before precipitation occurs. At 900°C, precipitation occurs after recrystallization is almost complete. At 850°C, precipitation occurs after a small amount of recrystallization occurs. It can be expected that the effect of strain-induced precipitation on recrystallization is none at 950°C, small at 900°C, and strong at 850°C in 1541VTi.

Similar precipitation behaviour is found for 1541Nb. Strain-induced precipitation has little, intermediate and strong effect on recrystallization at 1050, 1000 and 950°C, respectively. These predictions give good agreement with experimental observations.

Chapter 7. Summary

The main objective of this study was to model microstructural evolution of microalloyed forging steels during induction heating and thermomechanical processing.

A group of microalloyed forging steels have been used for the experiments: 1541Nb, 1541VTi, 1541Al and 1141Nb. Three experiments have been performed: (1) Precipitate dissolution and grain growth during induction heating; (2) Effect of initial microstructures on grain growth during induction reheat; and (3) Recrystallization and strain-induced precipitation after hot deformation. The effects of temperature and time on grain growth, precipitate sizes and recrystallization kinetics have been determined.

An important contribution of this study is the treatment for a distribution of precipitate sizes. Based on this, two physical models have been proposed: (1) A precipitate dissolution-coarsening model; and (2) A modified Zener equation for a distribution of precipitates.

These two models have been applied to precipitate size evolution and grain growth during induction heating. The precipitate sizes for as-rolled and preheated conditions have been used as the only input data. A series of precipitate size distributions and grain sizes have been predicted from the models and compared with experimental observations. It has been found that these models remain valid for many different microalloy elements, initial conditions and heating cycles.

Empirical equations have been determined for recrystallization kinetics in the absence of strain-induced precipitation. The effects of temperature, time and microalloy content have been incorporated in these equations, which broadens their application scope. It is also found that the starting point of strain-induced precipitation can be predicted by classic nucleation theory.

The following conclusions can be drawn from this study:

(1) Grain growth of microalloyed forging steels is influenced by steel composition and heating conditions. 1541VTi has the lowest grain growth rate during induction heating, while 1541Al has the highest. Grain sizes increase with increasing temperature and holding time.

(2) Grain growth of microalloyed forging steels during induction heating can be described as: small, uniform grain sizes at lower temperature; abnormal grain growth at intermediate temperature, and large but normal grain sizes at higher temperature.

(3) Precipitate evolution during induction heating is different from furnace heating. Precipitate density decreases during induction heating, and bimodal precipitate size distribution changes into unimodal at high temperature because some of the precipitates (especially small ones) dissolve into matrix. The precipitate size evolution cannot be explained by the existing theories based on mean sizes.

(4) Different initial microstructures give similar grain sizes at low reheat temperature, but different grain sizes are found when the temperature is higher. Compared with the as-rolled condition, the preheat + quench treatment results in smaller grain sizes at intermediate temperature because reprecipitation occurs in the supersaturated austenite in this temperature range. The preheat + slow cooling treatment gives larger grain sizes at high reheat temperature due to precipitate coarsening during the preheat cycle.

(5) The recrystallization kinetics of microalloyed forging steels can be described by the Avrami equation before strain-induced precipitation occurs. The precipitation-start time can be predicted by classic nucleation theory.

(6) Precipitate evolution during induction heating can be well described by the

precipitate dissolution-coarsening model proposed in this study. This model is based on diffusion theory but modified to incorporate the effect of precipitate size distribution and equilibrium solubility. This model shows that precipitate dissolution is the controlling mechanism during rapid induction heating.

(7) The Zener equation has been modified for a distribution of precipitate sizes. It is found that using the mean precipitate size usually overestimates the actual pinning pressure from a group of precipitates of different sizes. The difference may be up to a factor of 2, depending on precipitate size distributions.

(8) A grain growth model has been developed based on the modified Zener equation. Starting from the initial precipitate size distribution in the bar stock, this model predicts the mean grain diameter at all stage of the heating cycle, and gives a good agreement with measured values.

The following topics needs further investigation in future studies:

(1) Application of the derived models in other continuous heating cycles: The models established in this study are not limited to induction heating, although they were derived initially for induction heating process. Actually, they may be suitable for other kind of continuous heating cycles of microalloyed steels, such as continuous annealing or welding, because of the similar physical mechanisms.

(2) The effects of temperature and strain distributions on microstructural evolution: A typical forging operation involves non-uniform temperature and strain distributions. Their effects have not been considered in this study. The temperature and strain distributions are well described by existing finite element models. It would be worthwhile to combine

the established physical models with the finite element models to give better prediction of microstructural evolution during forging operations.

(3) The method to determine recrystallization fraction: Direct measurement of recrystallization fraction by metallography is difficult. Several methods are available to measure softening fraction from the stress-strain curves of double-hit recrystallization test, including back extrapolation method, 0.2% offset method, 5% offset method, and mean flow stress method. Each method has been supported by some experimental observations, however, they give different results when applied to one set of stress-strain curves. It is not clear which method gives the most reliable results. A method based on the areas under stress-strain curves has been used in this study because of its sound physical meaning. However, the difference between softening fraction and recrystallization is observed when the effect of recovery is not negligible. More work needs to be done to determine the contributions to softening by recrystallization and by recovery.

(4) Physical modeling of recrystallization: So far, most of the models on recrystallization kinetics are still based on fitting the Avrami equation, while physical models have been established for most other transformations. More generic models need to be developed.

Chapter 8. References

1. Aaron H.B. and Kotler G.R., 1971. "Second Phase Dissolution". Metallurgical Transactions, Vol.2, 393-408.
2. Aaron H.B., Fainstein D. and Kotler G.R., 1970. "Diffusion-Limited Phase Transformations: A Comparison and Critical Evaluation of the Mathematical Approximation". J. Appl. Phys., Vol.41, 4404-4409.
3. Aaronson H.I. and Lee .K., 1986. "The Kinetic Equations of Solid-Solid Nucleation Theory", Lectures on the Theory of Phase Transformations. Edited by Aaronson H.I., TMS, New York, 83-115.
4. Adrian H., 1992. "Thermodynamic Model for Precipitation of Carbonitrides in High Strength Low Alloy Steels Containing up to Three Microalloying Elements with or without Additions of Aluminum". Materials Science and Technology, Vol.8, 406-420.
5. Agren J., 1982. "Computer Simulations of Diffusion-Controlled Precipitation and Dissolution of Carbide Particles in Steel". Materials Science and Engineering, Vol.55, 135-141.
6. Agren J., 1990. "Kinetics of Carbide Dissolution". Scandinavia Journal of Metallurgy, Vol.19, 2-8.
7. Akbay T., Reed R.C. and Atkinson C., 1994. "Modelling Reaustenisation from Ferrite/Cementite Mixtures in Fe-C Steels". Acta Metallurgica Materialia, Vol.47, 1469-1480.
8. Akben M.G. and Jonas J.J., 1984. "Influence of Multiple Microalloy Additions on Flow Stress and Recrystallization Behavior of HSLA Steels", HSLA Steels, Technology and Applications, American Society for Metals, Metals Park, U.S.A.,

- 149-161.
9. Akselsen O.M., Grong ϕ ., Ryum N. and Christensen N., 1986. "HAZ Grain Growth Mechanism in Welding of Low Carbon Microalloyed Steels". *Acta Metallurgica*, Vol.34, 1807-1815.
 10. Almaguer S., Colas R., Garcia L.G. and Yescas M.A., and Munoz D., 1997. "A Model for Predicting Austenitic Grain Size during Forging". *Proceeding of Materials Solution '97 on Accelerated Cooling/Direct Quenching Steels*. Indianapolis, USA, 217-221.
 11. Anderson I. and Grong ϕ ., 1995. "Analytical Modelling of Grain Growth in Metals and Alloys in the Presence of Growth and Dissolving Precipitates-I. Normal Grain Growth. *Acta Metallurgica*, Vol.43, 2673-2688.
 12. Andrade H.L., Akben M.G. and Jonas J.J., 1983. "Effect of Molybdenum, Niobium, and Vanadium on Static Recovery and Recrystallization and on Solute Strengthening in Microalloyed Steels". *Metallurgical Transactions*, 1967-1977.
 13. Anelli E., 1992. "Application of Mathematical Modelling to Hot Rolling and Controlled Cooling of Wire Rods and Bars". *ISIJ International*, Vol.32, 440-449.
 14. Ashby M.F., 1992. "Physical Modeling of Materials Problem". *Materials Science and Technology*, Vol. 8, 102-111.
 15. Ashby M.F. and Easterling K.E., 1982. "A First Report on Diagram for Grain Growth in Welds". *Acta Metallurgica*, Vol.30, 1969-1978.
 16. Ashby M.F. and Ebeling R., 1966. "On the Determination of the Number, Size, Spacing, and Volume Fraction of Spherical Second-Phase Particles from Extraction Replicas". *Transactions of The Metallurgical Society of AIME*, Vol.236, 1396-

1404.

17. Avrami M., 1939. "Kinetics of Phase Change (I) - General Theory". *Journal of Chemical Physics*, Vol.7, 1103-1113.
18. Avrami M., 1940. " Kinetics of Phase Change (II) – Transformation-Time Relations for Random Distribution of Nuclei". *Journal of Chemical Physics*, Vol.8, 212-224.
19. Baragar D., 1999. Private communication.
20. Beck P.A., Kremer J.C. and Demer L., 1948. "Grain Growth in High Purity Aluminum". *Transactions of The Metallurgical Society of AIME*, Vol.175, 555.
21. Beck P.A., Kremer J.C., Demer L., and Holzworth M.L., 1948. "Grain Growth in High-Purity Aluminum and in an Aluminum-Magnesium Alloy". *Transactions of The Metallurgical Society of AIME*, Vol.175, 372-400.
22. Beynon J.H. and Sellars C.M., 1992. "Modeling Microstructure and Its Effects During Multipass Hot Rolling". *ISIJ International*, Vol.32, 359-367.
23. Cabrera J.M., Al Omar A., Jonas J.J. and Prado J.M., 1997. "Modeling the Flow Behavior of a Medium Carbon Microalloyed Steel under Hot Working Conditions". *Metallurgical and Materials Transactions*, 28A, 2233-2244.
24. Campbell P.J., Hodgson P.D., Lee M. and Gibbs R.K., "Modeling of Microstructural Changes during the Hot Rolling of C-Mn Steels". *THERMEC-88*, Vol. 2, Tokyo, Japan, 761-768.
25. Carsi M., Lopez V., Penalba F. and Ruano O.A., 1996. "The Strain Rate as a Factor Influencing the Hot Forming Simulation of Medium Carbon Microalloyed Steels". *Materials Science and Engineering*, Vol.A216, 155-160.
26. Choquet P., Lamberterie B.de, Perdrix C. and Biauxser H., 1987. "FAST: A New

- Model for Accurate Prediction of Rolling Force Application on the Solmer Hot Strip Mill". The Science and Technology of Flat Rolling: 4th Int. Steel Rolling Conf., Deauville, France, B.5.1-B.5.6.
27. Cruz-Rivera J.J., Cabanas-Moreno J.G. and Umemoto M., 1996. "A Comparative Study of Observed and Predicted Austenite Microstructures during Hot Rolling of a Medium Carbon Steel". ISIJ International, Vol.36, 300-309.
 28. Cuddy L.J. and Raley J.C., 1983. "Austenite Grain Coarsening in Microalloyed Steels". Metallurgical Transactions, Vol.14A, 1989-1995.
 29. Delgado H.E., Ramakrishnan R.I. and Howson T.E., 1994. "Improving Manufacturing by Cost-Effective process Modeling". JOM, Vol. 46, 21-23.
 30. Duggirala R., 1990. "Using the Finite Element Method in Metal-Forming Processes", JOM, Vol.42, 24-27.
 31. Dutta B. and Sellars C.M., 1987. "Effect of Composition and Process Variables on Nb(C,N) Precipitation in Niobium Microalloyed Austenite". Materials Science and Technology, Vol.3, 197-206.
 32. Dutta B., Valdes E. and Sellars C.M., 1992. "Mechanism and Kinetics of Strain Induced Precipitation of Nb(CN) in Austenite". Acta Metallurgica Materialia, Vol.40, 653-662.
 33. Exner H.E., 1972. "Analysis of Grain- and Particle-Size Distributions in Metallic Materials". International Metallurgical Reviews, Vol.17, 25-42.
 34. Feng B., Chandra T. and Dunne D.P., 1989. "Effect of Alloy Nitride Particle Size Distribution on Austenite Grain Coarsening in Ti and Ti-Nb Bearing HSLA Steels". Materials Forum, Vol.13, 139-146.

35. Fernandez A.I., Lopez B. and Rodriguez-Ibabe J.M., 1999. "Relationship Between the Austenite Recrystallized Fraction and the Softening Measured from the Interrupted Torsion Test Technique". *Scripta Metallurgica*, Vol.40, 543-549.
36. García de Andres C., Caballero, F.G., Capdevila C., and Bhadeshia H.K.D.H., 1998. "Modeling of Kinetics and Dilatometric Behavior of Non-isothermal Pearlite-to-Austenite Transformation in An Eutectoid Steel". *Scripta Materialia*, Vol. 39, 791-796.
37. Gegel H.L., Malas J.C., Doraivelu S.M. and Shende V.A., 1988. "Modeling Techniques Used in Forging Process Design". *ASM Handbook*, Vol.14. ASM International, USA, 417-438.
38. Gladman T. and Dulieu D., 1974. "Grain Size Control in Steels". *Metal Science*, Vol.8, 167-176.
39. Gladman T. and Pickering F.B., 1967. "Grain Coarsening of Austenite". *Journal of Iron and Steel Institute*, Vol.205, 653-664.
40. Gladman T., 1997. *The Physical Metallurgy of Microalloyed Steels*. The Institute of Materials, Cambridge, UK, 176.
41. Gordon P., 1955. "Microcalorimetric Investigation of Recrystallization of Copper". *Transactions of The Metallurgical Society of AIME*, Vol. 203, 1043-1052.
42. Grong ϕ , 1997. *Metallurgical Modeling of Welding*, 2nd Edition, Institute of Materials, London, 301-386.
43. Hannerz N.E. and Kazinczy F.De., 1970. "Kinetics of Austenite Grain Growth in Steel". *Journal of Iron and Steel Institute*, Vol.208, 475-481.
44. Hansen S.S., Vander Sander J.B. and Cohen M., 1980. "Niobium Carbonitride

- Precipitation and Austenite Recrystallization in Hot-Rolled Microalloyed Steels". Metallurgical Transactions, Vol.11A, 387-402.
45. Hellman P. and Hillert M., 1975. "On the Effect of Second-Phase Particles on Grain Growth". Scandinavian Journal of Metallurgy, Vol.4, 211-219.
 46. Herdan G., 1960. Small particle Statistics, Butterworths, London. 81-86.
 47. Hillert M. and Staffansson L.I., 1970. "The Regular Solution for Stoichiometric Phases and Ionic Melts". Acta Chemica Scandinavica, Vol.24, 3618-3626.
 48. Hodgson P.D. and Gibbs R.K., 1992. "A Mathematical Model to Predict the Mechanical Properties of Hot Rolled C-Mn and Microalloyed Steels". ISIJ International, Vol.32, 1329-1338.
 49. Howson T.E. and Delgado H.E., 1989. "Computer Modeling Metal Flow in Forging", JOM, Vol. 41, 32-34.
 50. Hu H. and Rath B.B., 1970. "Time Exponent in Isothermal Grain Growth". Metallurgical Transactions, Vol.1, 3181-3184.
 51. Hudd R.C., Jones A. and Kale M.N., 1971. "A Method for Calculating the Solubility and Composition of Carbonitride Precipitates in Steel with Particular Reference to Niobium Carbonitride". Journal of Iron and Steel Institute, Vol.209, 121-125.
 52. Humphreys F.J., 1992. "Modelling Mechanisms and Microstructures of Recrystallization". Materials Science and Technology, Vol.8, 135-143.
 53. Ion J.C., Easterling K.E. and Ashby M.F., 1984. "A Second Report on Diagrams of Microstructure and Hardness for Heat Affected Zones in Welds". Acta Metallurgica, Vol.32, 1949-1962.

54. Irvine K.J., Pickering F.B. and Gladman T., 1967. *Journal of Iron and Steel Institute*, Vol.205, 161.
55. Johansen T.H., Christensen N. and Augland B., 1967. *Transactions of The Metallurgical Society of AIME*, Vol.239, 1651.
56. Johnson W.A. and Mehl R.F., 1939. "Reaction Kinetics in Processes of Nucleation and Growth". *Transactions AIME*, Vol.135, 416-458.
57. Kaspar P. and Mahmoud N., 1991. "Austenite Grain Growth during Hot Forging of Medium Carbon Engineering Steels with or without V-Ti Microalloying". *Materials Science and Technology*, Vol.7, 249-254.
58. Kunze J., 1982. "Solubility Product of Titanium Nitride in γ -Iron". *Metal Science*, Vol.16, 217-218.
59. Kurtz S.K., 1980. "Microstructure and Normal Grain Growth in Metals and Ceramics. Part I. Theory" and "Part II. Experiment". *Journal of Applied Physics*, Vol.51, 5725-5754.
60. Kuziak R.M., and Cheng Y.W., 1996. "Microstructural Evolution in Microalloyed Medium-Carbon Forging Steels during Thermomechanical Processing". *International Conference on Processing, Microstructure and Properties of Microalloyed and Other Modern High Strength Low Alloy Steels*. Iron and Steel Society, Warrendale, USA, 51-64.
61. Kuziak R., Glowacki M. and Pietrzyk M., 1996. "Modelling of Plastic Flow, Heat Transfer and Microstructural Evolution during Rolling of Eutectoid Steel Rod". *Journal of Materials Processing Technology*, Vol.60, 589-596.
62. Kuziak R., Pietrzyk M. and Cheng Y., 1996. "Optimization of the Ferrite-Pearlite

- Microstructure of Vanadium Treated Medium-Carbon Steels by Means of Mathematical Modeling of Forging Process". *Microalloyed Bar and Forging Steels*, Edited by Van Tyne C.J., Krauss G. and Matlock D.K., TMS, 241-253.
63. Kuziak R., Pietrzyk M. and Chenot J.L., 1994. "Die Shape Design and Evaluation of Microstructure Control in the Closed-Die Axisymmetric Forging by Using FORGE2 Program". *ISIJ International*, Vol.34, 755-760.
 64. Kwon O., 1992. "A Technology for the Prediction and Control of Microstructural Changes and Mechanical Properties in Steel". *ISIJ International*, Vol.32, 350-358.
 65. Kwon O. and DeArdo A.J., 1986. "Niobium Carbonitride Precipitation and Static Softening in Hot-Deformed Niobium Microalloyed Steels". *HSLA Steels: Metallurgy and Applications*, ASM International, Metals Park, USA, 287-298.
 66. Kwon O., Lee K.J., Kang K.B., Ryu J.H. and Chang R.W., 1990. "Evaluation of the Recrystallization/Precipitation Interaction in Thermomechanical Processed Microalloyed Steels". *Recrystallization '90*, Ed. Chandra T., TMS, Warrendale, USA, 843-848.
 67. Lee K.J., 1999. "Recrystallization and Precipitation Interaction in Nb-Containing Steels". *Scripta Metallurgica*, Vol.40, 837-843.
 68. Liu W.J., Hawbolt E.B. and Samarasekera I.V., 1993. "A Multi-Particle Model for Predicting the Size Distribution of Precipitates in Microalloyed Austenite". *Modeling of Coarsening and Grain Growth*, Edited by Pande C.S. and Marsh S.P., TMS, Chicago, USA, 101-110.
 69. Liu W.J. and Jonas J.J., 1988. "Nucleation kinetics of Ti carbonitride in microalloyed austenite". *Metallurgical Transactions*, Vol.19, 1403-1414.

70. Loberg B., Nordgren A., Strid J. and Easterling K.E., 1984. "The Role of Alloy Composition on the Stability of Nitrides in Ti-Microalloyed Steels during Weld Thermal Cycles". *Metallurgical Transactions*, Vol.15A, 33-41.
71. Majta J., Lenard J.G., Pietrzyk M., 1996. "A Study of the Effect of the Thermo-mechanical History on the Mechanical Properties of a High Niobium Steel". *Materials Science and Engineering*, Vol.A208, 249-259.
72. Manohar P.A. and Chandra T., 1999. "A Mathematical Model to Predict Austenite Grain Size in Ti-Bearing Microalloyed Steels". *The Fourth International Conference on Recrystallization and Related Phenomena*. Edited by Sakai T. and Suzuki H.G., The Japan Institute of Metals, Tokyo, 769-774.
73. Manohar P.A., Dunne D.P., Chandra T. and Killmore C.R., 1996. "Grain Growth Predictions in Microalloyed Steels". *ISIJ International*, Vol.16, 194-200.
74. Manohar P.A., Ferry M. and Chandra T., 1998. "Five Decades of the Zener Equation". *ISIJ International*, Vol.38, 913-924.
75. Martin J.W. and Doherty R.D., 1976. *Stability of Microstructure in Metallic Systems*, Cambridge University Press, New York, USA, 173-197.
76. Matsuda S. and Okumura N., 1978. "Effect of Distribution of Ti Nitride Precipitate Particles on the Austenite Grain Size of Low Carbon and Low Alloy Steels". *Transaction ISIJ*, Vol.18, 198-205.
77. Medina S.F. and Fabregue P., 1991. "Activation Energy in the Static Recrystallization of Austenite". *Journal of Materials Science*, Vol.26, 5427-5432.
78. Medina S.F. and Mancilla J.E., 1993. "Determination of Static Recrystallization Critical Temperature of Austenite in Microalloyed Steels". *ISIJ International*,

- Vol.33, 1257-1264.
79. Medina S.F. and Mancilla J.E., 1994. "Static Recrystallization of Austenite and Strain Induced Precipitation Kinetics in Titanium Microalloyed Steels". *Acta Metallurgica Materialia*, Vol.12, 3945-3951.
 80. Medina S.F. and Quispe A., 1999. "Recrystallization Kinetics at Lower Temperatures than SRCT in Microalloyed Steels". The fourth International Conference on Recrystallization and Related Phenomena, Edited by Sakai T. and Suzuki H.G., The Japan Institute of Metals, Tokyo, 733-738.
 81. Medina S.F., Mancilla J.E. and Hernandez C.A., 1994. "Static Recrystallization of Hot Deformed Austenite and Induced Precipitation Kinetics in Vanadium Microalloyed Steels". *ISIJ International*, Vol.34, 689-696.
 82. Medina S.F., Mancilla J.E. and Hernandez C.A., 1993. "Influence of vanadium on the Static Recrystallization of Austenite in Microalloyed Steels". *Journal of Materials Science*, Vol.28, 5317-5324.
 83. Militzer M., Giunelli A., Hawbolt B. and Ray Meadowcroft T., 1996. "Austenite Grain Growth Kinetics in Al-Killed Plain Carbon Steels". *Metallurgical and Materials Transactions*, Vol.27A, 3399-3409.
 84. Militzer M., Sun W.P. and Jonas J.J., 1992. "A New Model for the Prediction of Precipitation Start Time". International Conference on Processing, Microstructure and Properties of Microalloyed and Other Modern High Strength Low Alloy Steels. Iron and Steel Society, Warrendale, USA, 271-280.
 85. Nes E., Ryum N. and Hunderi O., 1985. "On the Zener Drag". *Acta Metallurgica*, Vol.33, 11-22.

86. Okaguchi S. and Hashimoto T., 1992. "Computer Model for Prediction of Carbonitride Precipitation during Hot Working in Nb-Ti Bearing HSLA Steels". *ISIJ International*, Vol.32, 283-290.
87. Park S.H. and Jonas J.J., 1992. "Mathematical modeling of CCP (Continuous-Cooling-Precipitation) Diagrams". *Mathematical Modelling of Hot Rolling of Steel*, The Canadian Institute of Mining and Metallurgy, Montreal, Canada, 446-456.
88. Patterson B.R. and Liu Y., 1992. "Relationship Between Grain Boundary Curvature and Grain Size". *Metallurgical Transactions*, Vol.23A, 2481-2482.
89. Penalba F. and Carsi M., 1995. "Influence of Titanium on the Static Recrystallization of a Medium Carbon Microalloyed Steel". *Journal of Materials Science*, Vol.30, 1750-1753.
90. Pickering F.B., 1994. "Titanium Nitride Technology". *35th Mechanical Working and Steel Processing Conference Proceedings*, ISS, Warrendale, Vol.31, 477-491.
91. Pietrzyk M., Glowacki M. and Lenard J.G., 1994. "Numerical Simulation of the Evolution of the Microstructure in Closed-Die Forging". *Journal of Materials Processing Technology*, Vol.42, 217-226.
92. Pietrzyk M., Kedzieski Z., Glowacki M., Kusiak H. and Sinczak J., 1994. "Validation of the Thermomechanical Microstructural Model for Closed-Die Forging". *Steel Research*, Vol.65, 94-99.
93. Prikryl M., Kroupa A., Weatherly G.C. and Subramanian S.V., 1996. "Precipitation Behavior in a Medium Carbon, Ti-V-N Microalloyed Steel". *Metallurgical and Materials Transactions*, Vol.27A, 1149-1165.
94. Puskar J.D., Dykhuizen R.C., Robino C.V., Burnett M.E. and Kelley J.B., 1999.

- "Austenite Formation Kinetics During Rapid Heating in a Microalloyed Steel". 41st MWSP Conf. Proc., ISS, Vol.37, 625-635.
95. Rath B.B. and Hu H., 1969. Transactions of The Metallurgical Society of AIME, Vol.245, 1243 and 1577.
 96. Rios P.R., 1991. "Method for the Determination of Mole Fraction and Composition of a Multicomponent F.C.C. Carbonitride". Materials Science and Engineering, Vol.A142, 87-94.
 97. Rios P.R. and Schneider P.L., 1990. "Effect of Previous Heat Treatment on the Grain Growth of Austenite". Recrystallization '90. Edited by Chandra T., TMS, 1990, 331-336.
 98. Roberts W., Sandberg A., Siwecki T. and Werlefors T., 1983. "Prediction of Microstructure Development during Recrystallization Hot Rolling of Ti-V Steels". Conference Proceedings, HSLA Steels, Technology and Applications, American Society for Metals, Metals Park, USA, 67-84.
 99. Saito Y., 1997. "Modelling of Microstructural Evolution in Thermomechanical Processing of Structural Steels". Materials Science and Engineering, Vol.A223, 134-145.
 100. Saito Y., Shiga C. and Enami T., 1988. "Computer Simulation of Carbonitride Precipitation in High Strength Low Alloy (HSLA) Steel". Thermomec '88. The Iron and Steel Society of Japan, Tokyo, 753-760.
 101. Schacht E. and Richter J., 1998. "Experiences with Etching Reagents to Show Former Austenite Grain Boundaries in Steels". Praktique Metallography, Vol.35, 384-395.

102. Sellars C.M., 1979. "The Physical Metallurgy of Hot Working". Conference Proceedings, Hot Working and Forming Processes, Sheffield, England, 3-15.
103. Sellars C.M., 1986. "Options and Constraints for Thermomechanical Processing of Microalloyed Steel". Proceeding of HSLA Steels: Metallurgy and Applications, ASM International, Metals Park, USA, 73-81.
104. Sellars C.M. and Whiteman J.A., 1979. "Recrystallization and Grain Growth in Hot Rolling". Journal of Metal Science, Vol.13, 187-194.
105. Senuma T. and Yada H., 1986. "Microstructural Evolution of Plain Carbon Steels". Annealing Processes-Recovery, Recrystallization and Grain Growth, 7th Riso Int. Symp. on Metallurgy and Materials Science, Ed.Hansen N. et al., Riso, Roskilde, Denmark, 547-552.
106. Simpson P.G., 1960. Introduction Heating-Coil and System Design, McGraw-Hill Book Company Inc., 30-69.
107. Speer J.G. and Michael J.R. and Hansen S.S., 1987. "Carbonitride Precipitation in Niobium/Vanadium Microalloyed Steels". Metallurgical Transactions, Vol.18A, 211-222.
108. Strid J. and Easterling K.E., 1985. "On the Chemistry and Stability of Complex Carbides and Nitrides in Microalloyed Steels". Acta Metallurgica, Vol.33, 2057-2074.
109. Suehiro M., Sato K., Yada H., Senuma T., Shigefuji H. and Yamashita Y., 1988. "Mathematical Model for Predicting Microstructural Changes and Strength of Low Carbon Steels in Hot Strip Rolling". Thermomec '88, Toyako, 791-798.
110. Suzuki S., Weatherly G.C. and Houghton D.C., 1987. "The Response of Carbo-

- nitride Particles in HSLA Steels to Weld Thermal Cycles". *Acta Metallurgica*, Vol.35, 341-352.
111. Trivedi R.K., 1986. Lectures on the theory of Phase Transformations, Edited by Aaronson H.I., TMS, New York, 51.
112. Wang G.R., Lau T.W., Weatherly G.C. and North T.H., 1989. "Weld Thermal Cycles and Precipitation Effects in Ti-V-Containing HSLA Steels", *Metallurgical Transactions*, Vol.20A, 2093-2100.
113. Wang Z., Ishikawa T., Yukawa N., Kono A. and Tozawa Y., 1999. "Computer Simulation and Control of Microstructure and Mechanical Properties in Hot Forging". *Annals of the CIRP*, Vol.48, 187-190.
114. Yamamoto S., Ouchi C. and Osuka T., 1982. "the effect of Microalloying elements on the recovery and recrystallization in deformed austenite". *Thermomechanical Processing of Microalloyed Austenite*, Edited by DeArdo A.J., Tatz G.A. and Wrayeds P.J., TMS-AIME, Warrendale, 613-639.
115. Yong Q.L., Ma M.T. and Wu B.R., 1989. *Microalloyed Steels - Physical and Mechanical Metallurgy*, Mechanical Industry Press (in Chinese).
116. Yoshie A., Fujioka M., Watanabe Y. and Morikawa H., 1992. *ISIJ International*, Vol.32, 395.
117. Yoshie A., Fujioka M., Watanabe Y., Nishioka K. and Morikawa H., 1992. "Modelling of Microstructural Evolution and Mechanical Properties of Steel Plates Produced by Thermo-Mechanical Control Process". *ISIJ International*, Vol.32, 395-404.
118. Yoshie A., Fujita T., Fujioka M., Okamoto K. and Morikawa H., 1996.

- "Formulation of Flow Stress of Nb Added Steels by Considering Work-hardening and Dynamic Recovery". ISIJ International, Vol.36. 467-473.
119. Yoshie A., Fujita T., Fujioka M., Okamoto K. and Morikawa H., 1996. "Formulation of the Decrease in Dislocation Density of Deformed Austenite Due to Static Recovery and Recrystallization". ISIJ International, Vol.36. 474-480.
120. Yoshie A., Morikawa H., Onoe Y. and Itoh K., 1987. "Formulation of Static Recrystallization of Austenite in Hot Rolling Process of Steel Plate". Transactions ISIJ. Vol.27. 425-431.
121. Zou H.L. and Kirkaldy J.S., 1991. "Carbonitride Precipitate Growth in Titanium/Niobium Microalloyed Steels". Metallurgical Transactions, Vol.22A, 1511-1524.
122. Zou H.L. and Kirkaldy J.S., 1992. "Thermodynamic Calculation and Experimental Verification of the Carbonitride-Austenite Equilibrium in Ti-Nb Microalloyed Steels". Metallurgical Transactions. Vol.23A. 651-657.

Appendix A. Calculation of Equilibrium Solubility of Complex Carbonitrides

A.1 Nb(C,N) type of carbonitrides

The calculation method for solubility of Nb(C,N) type of precipitates was suggested by Hudd *et al.* (1971). A group of 2 equations have been derived as follows:

$$yK_{NbC} = [Nb] \left\{ C_0 - y(Nb_0 - [Nb]) \frac{M_C}{M_{Nb}} \right\} \quad [\text{A.1a}]$$

$$(1-y)K_{NbN} = [Nb] \left\{ N_0 - (1-y)(Nb_0 - [Nb]) \frac{M_N}{M_{Nb}} \right\} \quad [\text{A.1b}]$$

where y is the atomic fraction of carbon in the carbonitride. There are 2 unknowns, $[Nb]$ and y , in the 2 equations. Their values can be easily solved with numerical methods. The following computer program has been written with Maple V. The numbers at the beginning of each line is not required by the program, but used only for easy understanding.

- 1) **# input Nb, C and N contents in the steel and the reheat temperature.**
- 2) Nb0:=0.038: C0:=0.41: N0:=0.0053: Temp:=900+273:
- 3) **# input materials constants (mole weight and density)**
- 4) MNb:=92.91: MC:=14.01: MN:=12.01:
- 5) gammaFe:=8.0: gammaNbC:=7.84: gammaNbN:=8.41:
- 6) **# input solubility product data**
- 7) KNbC:=10^(4.37-9290/Temp):
- 8) KNbN:=10^(4.04-10230/Temp):

9) # build the equation

10) $\text{Coeff4} := -\text{MN} * \text{MC};$

11) $\text{Coeff3} := 2 * \text{Nb0} * \text{MN} * \text{MC} - \text{C0} * \text{MC} * \text{MNb} - \text{N0} * \text{MN} * \text{MNb};$

12) $\text{Coeff2} := \text{MNb} * \text{MN} * \text{KNbN} + \text{N0} * \text{Nb0} * \text{MN} * \text{MNb} - \text{Nb0} * \text{Nb0} * \text{MC} * \text{MN}$
 $+ \text{MNb} * \text{MC} * \text{KNbC} + \text{C0} * \text{Nb0} * \text{MC} * \text{MNb};$

13) $\text{Coeff1} := \text{N0} * \text{KNbC} * \text{MNb} * \text{MNb} - \text{KNbN} * \text{Nb0} * \text{MN} * \text{MNb} - \text{Nb0} * \text{MNb} * \text{MC} * \text{KNbC}$
 $+ \text{C0} * \text{KNbN} * \text{MNb} * \text{MNb};$

14) $\text{Coeff0} := -\text{KNbC} * \text{KNbN} * \text{MNb} * \text{MNb};$

15) $\text{Eq} := \text{Coeff4} * \text{Nbswt}^4 + \text{Coeff3} * \text{Nbswt}^3 + \text{Coeff2} * \text{Nbswt}^2 + \text{Coeff1} * \text{Nbswt}$
 $+ \text{Coeff0} = 0;$

16) # solve the equation to get the required data

17) $\text{solution} := \text{fsolve}(\{\text{Eq}\}, \{\text{Nbswt}\}, \{\text{Nbswt} = 0 \dots \text{Nb0}\});$

18) $\text{assign}(\%);$

19) $x := \text{Nbswt} * \text{C0} * \text{MNb} / (\text{MNb} * \text{KNbC} + \text{Nbswt} * (\text{Nb0} - \text{Nbswt}) * \text{MN});$

20) $\text{Nbppt} := \text{Nb0} - \text{Nbswt};$

21) $\text{Cppt} := x * \text{Nbppt} * \text{MN} / \text{MNb};$

22) $\text{Cswt} := \text{C0} - \text{Cppt};$

23) $\text{Nppt} := (1 - x) * (\text{Nb0} - \text{Nbswt}) * \text{MC} / \text{MNb};$

24) $\text{Nswt} := \text{N0} - \text{Nppt};$

25) $f\text{NbC} := \text{Cppt} * (1 + \text{MNb} / \text{MC}) * \text{gammaFe} / \text{gammaNbC};$

26) $f\text{NbN} := \text{Nppt} * (1 + \text{MNb} / \text{MN}) * \text{gammaFe} / \text{gammaNbN};$

27) $f := f\text{NbC} + f\text{NbN};$

28) #reset the variables for next calculation.

- 29) unassign('f','x','Cppt','Cswt','Nppt','Nswt','fNbC','fNbN','Temp');
- 30) unassign('Coeff4','Coeff3','Coeff2','Coeff1','Coeff0');
- 31) unassign('KNbC','KNbN','Nbswt','Nbppt');

A.2 (Nb,V)(C,N) type of Carbonitrides

For the solubility of (Nb,V)(C,N) type carbonitrides, the regular solution model proposed by Hillert and Staffansson (1970) was used by Speer *et al.* (1987) to express the free energy of the (Nb,V)(C,N) with the free energies of the binary compounds:

$$G_{\text{Nb,V,C,N}} = xyG_{\text{NbC}}^0 + x(1-y)G_{\text{NbN}}^0 + (1-x)yG_{\text{VC}}^0 + (1-x)(1-y)G_{\text{VN}}^0 - T^1S^m + {}^E G^m \quad [\text{A.2}]$$

where x , y are the atomic fractions of Ti and C in the carbonitride. G_{NbC}^0 , G_{NbN}^0 , G_{VC}^0 and G_{VN}^0 are the molar free energies of the pure binary compounds. ${}^1S^m$ is the ideal molar entropy of mixing. ${}^E G^m$ is the excess molar free energy of mixing. According to Timkin (Speer *et al.*, 1987), the ideal entropy of mixing is:

$${}^1S^m = -R[x \ln x + (1-x) \ln(1-x) + y \ln y + (1-y) \ln(1-y)] \quad [\text{A.3}]$$

The excess molar free energy of mixing is expressed using regular solution model:

$${}^E G^m = x(1-x)y\Omega_{\text{NbV}}^{\text{C}} + x(1-x)(1-y)\Omega_{\text{NbV}}^{\text{N}} + xy(1-y)\Omega_{\text{CN}}^{\text{Nb}} + (1-x)y(1-y)\Omega_{\text{CN}}^{\text{V}} \quad [\text{A.4}]$$

where $\Omega_{\text{NbV}}^{\text{C}}$, $\Omega_{\text{NbV}}^{\text{N}}$, $\Omega_{\text{CN}}^{\text{Nb}}$, $\Omega_{\text{CN}}^{\text{V}}$ are regular solution parameters.

A group of three equations have been derived by following these assumptions:

$$y \ln \frac{xyK_{NBC}}{[Nb][C]} + (1-y) \ln \frac{x(1-y)K_{NbN}}{[Nb][N]} + \frac{\Omega_{CN}}{RT} [y(1-y)] = 0 \quad [\text{A.5a}]$$

$$x \ln \frac{xyK_{NBC}}{[Nb][C]} + (1-x) \ln \frac{y(1-x)K_{VC}}{[V][C]} + \frac{\Omega_{CN}}{RT} [(1-y)^2] = 0 \quad [\text{A.5b}]$$

$$x \ln \frac{x(1-y)K_{NbN}}{[Nb][N]} + (1-x) \ln \frac{(1-x)(1-y)K_{VN}}{[V][N]} + \frac{\Omega_{CN}}{RT} y^2 = 0 \quad [\text{A.5c}]$$

The required mass balance equations are:

$$Nb_0 = f\left(\frac{x}{2}\right) + (1-f)[Nb] \quad [\text{A.5d}]$$

$$V_0 = f\left(\frac{1-x}{2}\right) + (1-f)[V] \quad [\text{A.5e}]$$

$$C_0 = f\left(\frac{y}{2}\right) + (1-f)[C] \quad [\text{A.5f}]$$

$$N_0 = f\left(\frac{1-y}{2}\right) + (1-f)[N] \quad [\text{A.5g}]$$

where Ω_{CN} is regular solution parameter. $[Nb]$, $[V]$, $[C]$ and $[N]$ are the equilibrium mole fractions of each species in austenite. f is the *mole fraction* of precipitates at equilibrium. Nb_0 , V_0 , C_0 and N_0 are mole fractions of these elements in the steel.

There are seven equations from Equations A.5(a-g) and seven unknowns ($[Nb]$, $[V]$, $[C]$, $[N]$, f , x and y). It has been found that this group of equations are very difficult to solve, since negative values are often passed into the logarithm during numerical calculation. The initial values have to be selected carefully to get convergence.

This problem can be solved by programming with Maple V. The complex numerical calculations are handled by the internal mathematics library. Therefore, the calculation procedures are significantly simplified. The initial values are generally not necessary. The results of an example of calculation is given in Figure A.1 for 1541VTi.

- 1) # This program is based on the methodology developed by Speer *et al.* (1987).
- 2) # **Input the desired reheat temperature.**
- 3) $T:=1000+273;$
- 4) # the molar weight of Nb,V,Ti,C,N,Fe.
- 5) $M_{Nb}:=92.91; M_V:=50.95; M_{Ti}:=47.90; M_C:=12.01; M_N:=14.01; M_{Fe}:=55.85;$
- 6) #Regular solution parameter LCN and gas constant R.
- 7) $LCN:=-4260; R:=8.314;$
- 8) # **the Nb,V and Ti composition(wt%) in the steel.**
- 9) $Ti0wt:=0.014; V0wt:=0.114; C0wt:=0.4; N0wt:=0.009;$
- 10) # **convert wt% into at%.**
- 11) $C0:=C0wt*M_{Fe}/(100*M_C);$
- 12) $N0:=N0wt*M_{Fe}/(100*M_N);$
- 13) $V0:=V0wt*M_{Fe}/(100*M_V);$
- 14) $Ti0:=Ti0wt*M_{Fe}/(100*M_{Ti});$
- 15) # **solubility product(in wt%) of NbC, VC and TiC respectively.**
- 16) $K_{VCwt}:=10^{(6.72-9500/T)};$
- 17) $K_{TiCwt}:=10^{(2.75-7500/T)};$
- 18) # **solubility product(in wt%) of NbN, VN, and TiN respectively.**
- 19) $K_{VNwt}:=10^{(3.46-8330/T)};$
- 20) $K_{TiNwt}:=10^{(0.322-8000/T)};$
- 21) # **convert solubility product from wt% into at%.**
- 22) $K_{VC}:=\frac{(M_{Fe}/100)^2}{(M_V*M_C)*K_{VCwt}};$
- 23) $K_{TiC}:=\frac{(M_{Fe}/100)^2}{(M_{Ti}*M_C)*K_{TiCwt}};$

- 24) $KVN := (MFe/100)^2 / (MV * MN) * KVNwt;$
- 25) $KTiN := (MFe/100)^2 / (MTi * MN) * KTiNwt;$
- 26) # Nbeq, Veq, Ceq, Neq are the molar content of Nb, V, C, N in austenite respective.
f is the molar fraction of carbonitride. The stoichiometry of the carbonitride is $Nb_x V_{1-x} C_y N_{1-y}$.
- 27) #Eq1~Eq7 are the set of equations with 7 unknowns (Nbeq, Veq, Ceq, Neq, x, y, f).
- 28) Eq1: $y * \ln(x * y * KTiC / (Tieq * Ceq)) + (1-y) * \ln(x * (1-y) * KTiN / (Tieq * Neq))$
 $+ LCN/R/T * y * (1-y) = 0;$
- 29) Eq2: $x * \ln(x * y * KTiC / (Tieq * Ceq)) + (1-x) * \ln(y * (1-x) * KVC / (Veq * Ceq))$
 $+ LCN/R/T * (1-y)^2 = 0;$
- 30) Eq3: $x * \ln(x * (1-y) * KTiN / (Tieq * Neq)) + (1-x) * \ln((1-x) * (1-y) * KVN / (Veq * Neq))$
 $+ LCN/R/T * y * y = 0;$
- 31) Eq4: $Tieq = (Ti0 - f * x / 2) / (1-f);$
- 32) Eq5: $Veq = (V0 - f * (1-x) / 2) / (1-f);$
- 33) Eq6: $Ceq = (C0 - f * y / 2) / (1-f);$
- 34) Eq7: $Neq = (N0 - f * (1-y) / 2) / (1-f);$
- 35) # substitute Eq4~Eq7 into Eq1, Eq2 and Eq3 respectively. Three equations will be obtained: Eq8, Eq9 and Eq10, with 3 unknowns(f, x, y).
- 36) Eq8: $= \text{subs}(Tieq = (Ti0 - f * x / 2) / (1-f), Veq = (V0 - f * (1-x) / 2) / (1-f), Ceq = (C0 - f * y / 2) / (1-f),$
 $Neq = (N0 - f * (1-y) / 2) / (1-f), Eq1);$
- 37) Eq9: $= \text{subs}(Tieq = (Ti0 - f * x / 2) / (1-f), Veq = (V0 - f * (1-x) / 2) / (1-f), Ceq = (C0 - f * y / 2) / (1-f),$
 $Neq = (N0 - f * (1-y) / 2) / (1-f), Eq2);$

```

38) Eq10:=subs(Tieq=(Ti0-f*x/2)/(1-f),Veq=(V0-f*(1-x)/2)/(1-f),Ceq=(C0-f*y/2)/(1-f),
    Neq=(N0-f*(1-y)/2)/(1-f),Eq3);
39) # Solve Eq8~Eq10 to get the values of f, x and y. The solution ranges are
    specified to ensure the correct answer. Otherwise, negative solutions may come
    out. The specified ranges are also helpful to shorten the calculating time.
40) solution:=fsolve({Eq8,Eq9,Eq10},{f,x,y},{f=0..0.01,x=0..1,y=0..1}); assign(%);
41) # To get the molar fractions of Nb, V, C, N in austenite.
42) Tieq=(Ti0-f*x/2)/(1-f); assign(%);
43) Veq=(V0-f*(1-x)/2)/(1-f); assign(%);
44) Ceq=(C0-f*y/2)/(1-f); assign(%);
45) Neq=(N0-f*(1-y)/2)/(1-f); assign(%);
46) # Change the molar fraction into weight percent.
47) Tieqwt:=Tieq*100*MTi/MFe;
48) Veqwt:=Veq*100*MV/MFe;
49) # Cswt, Nswt are the weight percent of C, N in solution.
50) Ceqwt:=Ceq*100*MC/MFe;
51) Neqwt:=Neq*100*MN/MFe;
52) # Reset the variables for the next calculation.
53) unassign('f','x','y','Nbeq','Veq','Tieq','Ceq','Neq');
54) unassign('C0','N0','Nb0','V0','Ti0','T','R','LCN');
55) unassign('KNbC','KVC','KTiC','KNbN','KVN','KTiN');

```

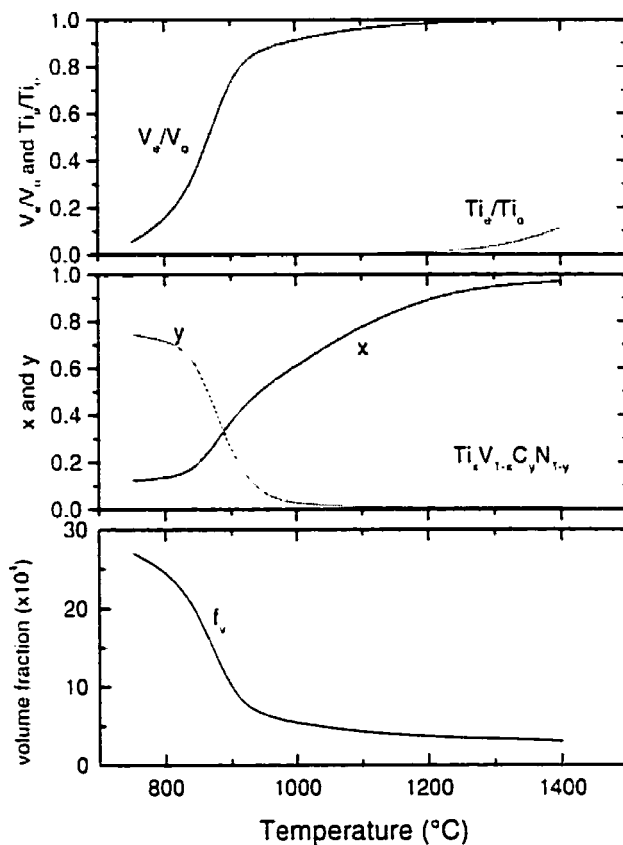


Figure A.1 Equilibrium solubility of V and Ti, volume fraction of precipitates, atomic fraction of Ti and C in precipitates, at different temperatures (1541VTi). Where V_e and Ti_e are dissolved V and Ti respectively. V_0 and Ti_0 are the total V and Ti contents in the steel. x and y are the atomic fractions of Ti and C in the carbonitride.

A.3 $(M_1, \dots, M_n)(C, N)$ Type of Carbonitrides.

For more complex carbonitrides like $(M_1, \dots, M_n)(C, N)$, Rios (1991) further extended the regular solution model to calculate the solubility of multi-component carbonitride. It has been shown that:

$$[C] = \frac{x}{\sum \frac{M_{0i} / K_{MCi}}{1 - 2f + f([C]/K_{MCi} + [N]/K_{MNi})}} \quad [\text{A.6a}]$$

$$[N] = \frac{1 - y}{\sum \frac{M_{0i} / K_{MNi}}{1 - 2f + f([C]/K_{MCi} + [N]/K_{MNi})}} \quad [\text{A.6b}]$$

$$f = \frac{C_0 + N_0 - [C] - [N]}{1 - 2([C] + [N])} \quad [\text{A.6c}]$$

$$yf = C_0 - (1 - 2f)[C] \quad [\text{A.6d}]$$

$$(1 - y)f = N_0 - (1 - 2f)[N] \quad [\text{A.6e}]$$

where f is the molar fraction of carbonitride, y is the atomic fractions of carbon in the complex carbonitride. K_{MCi} and K_{MNi} are the molar solubility products of binary carbides and nitrides. $[C]$ and $[N]$ are the equilibrium molar fractions of carbon and nitrogen in austenite. M_{0i} is molar fraction of the microalloy element in the steel.

Substituting A.6(c-e) into A.6(a and b) results in a group of two equations with two unknowns, $[C]$ and $[N]$. Their values can be solved easily with numerical methods, then the other unknowns can be obtained.

- 1) # This program is based on the methodology developed by R.P. Rios (1991).
- 2) # the molar weight of Nb, V, Ti, C, N, Fe.
- 3) MNb:=92.91: MV:=50.95: MTi:=47.90: MC:=12.01: MN:=14.01: MFe:=55.85:
- 4) # the Nb,V and Ti contents(wt%) in the steel.
- 5) X01wt:=0.18: X02wt:=0.21: X03wt:=0.0: C0wt:=0.57: N0wt:=0.018:
- 6) # Input the desired reheat temperature.

- 7) $T:=1200+273$;
- 8) **# solubility product(in wt%) of NbC, VC and TiC respectively.**
- 9) $KC1wt:=10^{(4.37-9290/T)}$;
- 10) $KC2wt:=10^{(6.72-9500/T)}$;
- 11) $KC3wt:=10^{(2.75-7500/T)}$;
- 12) **# solubility product(in wt%) of NbN, VN, and TiN respectively.**
- 13) $KN1wt:=10^{(4.04-10230/T)}$;
- 14) $KN2wt:=10^{(3.46-8330/T)}$;
- 15) $KN3wt:=10^{(0.322-8000/T)}$;
- 16) **# convert solubility product from wt% into at%.**
- 17) $KC1:=(MFe/100)^2/(MNb*MC)*KC1wt$;
- 18) $KC2:=(MFe/100)^2/(MV*MC)*KC2wt$;
- 19) $KC3:=(MFe/100)^2/(MTi*MC)*KC3wt$;
- 20) $KN1:=(MFe/100)^2/(MNb*MN)*KN1wt$;
- 21) $KN2:=(MFe/100)^2/(MV*MN)*KN2wt$;
- 22) $KN3:=(MFe/100)^2/(MTi*MN)*KN3wt$;
- 23) **# convert wt% into at%.**
- 24) $C0:=C0wt*MFe/(100*MC)$;
- 25) $N0:=N0wt*MFe/(100*MN)$;
- 26) $X01:=X01wt*MFe/(100*MNb)$;
- 27) $X02:=X02wt*MFe/(100*MV)$;
- 28) $X03:=X03wt*MFe/(100*MTi)$;
- 29) **# f is the molar fraction of carbonitride. y and fN are the atomic fractions of carbon**

and nitrogen respectively in the interstitial lattice of the complex carbonitride. Cs and Ns are the atomic fractions of carbon and nitrogen respectively in solution in austenite.

- 30) Eq1:=f=(C0+N0-Cs-Ns)/(1-2*(Cs+Ns));
- 31) Eq2:=y=(C0-(1-2*f)*Cs)/f;
- 32) subs(f=(C0+N0-Cs-Ns)/(1-2*Cs-2*Ns),Eq2); simplify(%);
- 33) Eq3:=1-y=(N0-(1-2*f)*Ns)/f;
- 34) subs(f=(C0+N0-Cs-Ns)/(1-2*Cs-2*Ns),Eq3); simplify(%);
- 35) Eq4:=Cs=y/(X01/(KC1*(1-2*f+f*(Cs/KC1+Ns/KN1)))+X02/(KC2*(1-2*f+f*(Cs/KC2+Ns/KN2)))+X03/(KC3*(1-2*f+f*(Cs/KC3+Ns/KN3))));
- 36) Eq6:=subs(f=(C0+N0-Cs-Ns)/(1-2*Cs-2*Ns),y = -(-C0+2*C0*Ns+Cs-2*Cs*N0)/(C0+N0-Cs-Ns),1-y = (N0-2*Cs*N0-Ns+2*C0*Ns)/(C0+N0-Cs-Ns),Eq4);
- 37) Eq5:=Ns=(1-y)/(X01/(KN1*(1-2*f+f*(Cs/KC1+Ns/KN1)))+X02/(KN2*(1-2*f+f*(Cs/KC2+Ns/KN2)))+X03/(KN3*(1-2*f+f*(Cs/KC3+Ns/KN3))));
- 38) Eq7:=subs(f=(C0+N0-Cs-Ns)/(1-2*Cs-2*Ns),y = -(-C0+2*C0*Ns+Cs-2*Cs*N0)/(C0+N0-Cs-Ns),(1-y) = (N0-2*Cs*N0-Ns+2*C0*Ns)/(C0+N0-Cs-Ns),Eq5);
- 39) # Solve Eq.6 and 7 to get the Cs and Ns and other parameters.**
- 40) solution2:=fsolve({Eq6,Eq7},{Cs,Ns},{Cs=0..1,Ns=0..1}); assign(%);
- 41) f=(C0+N0-Cs-Ns)/(1-2*(Cs+Ns)); assign(%);
- 42) y = -(-C0+2*C0*Ns+Cs-2*Cs*N0)/(C0+N0-Cs-Ns); assign(%);
- 43) 1-y = (N0-2*Cs*N0-Ns+2*C0*Ns)/(C0+N0-Cs-Ns); assign(%);

- 44) # X1, X2, X3 is the atomic fraction of Nb,V,Ti in austenite.
- 45) $X1:=X01/(1-2*f+f*(Cs/KC1+Ns/KN1));$
- 46) $X2:=X02/(1-2*f+f*(Cs/KC2+Ns/KN2));$
- 47) $X3:=X03/(1-2*f+f*(Cs/KC3+Ns/KN3));$
- 48) # f1, f2, f3 is the atomic fraction of Nb,V, Ti in the substitutional lattice.
- 49) $f1:=(X01-(1-2*f)*X1)/f;$
- 50) $f2:=(X02-(1-2*f)*X2)/f;$
- 51) $f3:=(X03-(1-2*f)*X3)/f;$
- 52) # X1wt, X2wt, X3wt are the weight percent of Nb, V, Ti in austenite.**
- 53) $X1wt:=X1*100*MNb/MFe;$
- 54) $X2wt:=X2*100*MV/MFe;$
- 55) $X3wt:=X3*100*Ti/MFe;$
- 56) # Cswt, Nswt are the weight percent of C, N in solution.**
- 57) $Cswt:=Cs*100*MC/MFe;$
- 58) $Nswt:=Ns*100*MN/MFe;$
- 59) #Reset the variables for next calculation.
- 60) unassign('f','y','Cs','Ns');
- 61) unassign('C0','N0','X01','X02','X03');
- 62) unassign('KC1','KN1','KC2','KN2','KC3','KN3');

Appendix B. Calculation of Precipitate Evolution during Induction Heating

The calculation of precipitate dissolution and coarsening is based on a numerical method. The continuous heating cycle has been sectioned into a number of small intervals. Isothermal condition is assumed in each interval. The change of precipitate size is recorded and upgraded in each interval by the rule of additivity. The dissolution-coarsening model has been discussed in §4.5.

Dissolution should stop when equilibrium solubility is reached. The volume fraction change following precipitate dissolution is monitored during each step of the calculation, so that the equilibrium solubility is not exceeded.

The precipitates measured in the as-rolled or as-preheated condition have been used as the initial precipitate size distribution. More than 300 precipitate diameters have been input for a calculation. The size of each precipitate is tracked at each step of the calculation, therefore, the precipitate size distribution can be obtained. The starting temperature is 720°C for 1541Nb and 700°C for 1541VTi. According to the solubility calculations, the maximum volume fractions of precipitate are obtained at these temperatures.

The following program has been used for 1541Nb. It is written in Turing language. This is a small, simple and user-friendly software developed by the University of Toronto.

- 1) **% Composition of the steel (1541Nb)**
- 2) const Nb0:real:=0.036
- 3) const C0:real:=0.40
- 4) const N0:real:=0.005
- 5) **% reheat temperature and temperature for starting calculation.**
- 6) var Vreheat:real % reheat rate(C/sec)
- 7) var Tr:real:=700+273. % assume it is the room temp.
- 8) const T0:real:=720+273. % temp. for starting calc.
- 9) var Treheat:real:=1260+273. % reheat temp.
- 10) **% Materials constants**
- 11) const MNb:real:=92.91 % atomic weight of Nb
- 12) const MC:real:=14.01 % atomic weight of N
- 13) const MN:real:=12.01 % atomic weight of C
- 14) const R:real:=8.314
- 15) const gammaFe:=8.0 % density of Fe(austenite)
- 16) const gammaNbC:=7.84
- 17) const gammaNbN:=8.41
- 18) **Variables for calculations.**
- 19) var Nbswt,Cswt,Nswt:real % Nb/C/N content in solution
- 20) var x:real % atomic fraction of C in ppt.
- 21) var Nbppt, Cppt, Nppt:real % Nb/C/N content in ppt
- 22) var fNbC, fNbN:real % volume fraction of NbC and NbN
- 23) var step:real % step by step integration.

```

24) var f0:real          % volume fraction of NbCN at room temp.
25) var CNbi, CNbm :real % Nb conc. at interphase, matrix and ppt.
26) var CNbppt:=MNb/(MNb+MN/2+MC/2) % 1/2 is used for simplification.
27) var D:real          % Diffusion coefficient of V in austenite.
28) var f:real          % volume fraction of NbCN.
29) var k:real          % supersaturation ratio
30) var T:real:=T0      % Tr:room temperature.
31) % Input experimental data. All the data are saved in file "AS1541Nb.txt".
32) % This file should be saved in the folder where Turing is saved (C:\winoot\).
33) var fileName:string:="AS1541Nb.txt"
34) var fileNo:int      % used for the opened file.
35) var N:int:=440
36) var r, r0, r_tmp:array 1..N of real % r_tmp used for save r(i) values.
37) var r0_sum:real:=0
38) % it is assumed that  $f/f_0=(r1^3+r2^3+...)/(r01^3+r02^3+...)$ 
39) % r0_sum is used to save  $(r01^3+r02^3+...)$ 
40) open: fileNo, fileName, get
41)   for i:1..N
42)     %exit when eof
43)     get : fileNo, r0(i)
44)     r0(i):=r0(i)/10**7
45)     r(i):=r0(i)
46)     r0_sum:=r0_sum+r(i)**3

```

```

47)     end for
48) close: fileNo
49) % Solve equation for equilibrium solubility of Nb. Bisection method is used to
      calculate the results. The initial value of [Nb]sol (NbLeft and NbRight) are
      assumed to start the calculation. The required range of error is Epsilon<=0.00001.
50) function Sol_Nb(var T:real):real
51) var NbLeft, NbRight, Z:real %Z is required for the iteration method.
52) var Epsilon:real:=0.000001
53) var Coeff0,Coeff1,Coeff2,Coeff3,Coeff4:real
54) NbLeft:=0.0
55) NbRight:=Nb0
56) var KNbC,KNbN:real % solubility product of NbC/NbN
57) KNbC:=10**((4.37-9290/T) % log[Nb][C]= 4.37-9290/T
58) KNbN:=10**((4.04-10230/T) % log[Nb][N]=4.04-10230/T
59) Coeff4:=-MN*MC
60) Coeff3:=2*Nb0*MN*MC-C0*MC*MNb-N0*MN*MNb
61) Coeff2:=MNb*MN*KNbN+N0*Nb0*MN*MNb-
      Nb0*Nb0*MC*MN+MNb*MC*KNbC+C0*Nb0*MC*MNb
62) Coeff1:=N0*KNbC*MNb*MNb-KNbN*Nb0*MN*MNb-
      Nb0*MNb*MC*KNbC+C0*KNbN*MNb*MNb
63) Coeff0:=-KNbC*KNbN*MNb*MNb
64) % Start Calculation
65) loop

```

```

66)     Nbswt:=(NbLeft+NbRight)/2
67)     Z:=Nbswt**4*Coeff4+Nbswt**3*Coeff3+Nbswt**2*Coeff2+Nbswt*Coeff1
        +Coeff0
68)     exit when abs(NbRight-Nbswt)<=Epsilon
69)     if Z<0 then
70)         NbLeft:=Nbswt
71)     else
72)         NbRight:=Nbswt
73)     end if
74) end loop
75) result Nbswt
76) end Sol_Nb

77) % Calculate equilibrium volume fraction
78) function Vol_Fract(var T:real):real
79) var Nbswt:=Sol_Nb(T)
80) x:=Nbswt*C0*MNb/(MNb*KNbC+Nbswt*(Nb0-Nbswt)*MN)
81) Nbppt:=Nb0-Nbswt
82) Cppt:=x*Nbppt*MN/MNb
83) Nppt:=(1-x)*(Nb0-Nbswt)*MC/MNb
84) fNbC:=Cppt*(1+MNb/MC)*gammaFe/gammaNbC
85) fNbN:=Nppt*(1+MNb/MN)*gammaFe/gammaNbN
86) result fNbC+fNbN
87) end Vol_Fract

```



```

88) % calculate the supersaturation ratio, k.
89) function SatuRatio(var T:real):real
90)   CNbi:=Sol_Nb(T)
91)   CNbm:=Sol_Nb(Tr)
92)   k:=2*(CNbi-CNbm)/(CNbppt-CNbi)
93)   result k
94) end SatuRatio

95) % calculate diffusion rate, D.
96) function Diffusion(var T:real): real
97)   D:=530*exp(-344600/(R*T))
98)   result D
99) end Diffusion

100) % Precipitate dissolution during heating (and holding).
101) f0:=Vol_Fract(Tr)
102) var time_diss, t_hold, t_held:real
103) var r_sum:real
104) t_hold:real:=60
105) put "holding time=", t_hold
106) var count:int:=0
107) var k1, D1, f1:real
108) loop
109)   k1:=SatuRatio(T)
110)   D1:=Diffusion(T)

```

```
111)    f1:=Vol_Fract(T)
112)    r_sum:=0
113)    if T<=870+273 then
114)        Vreheat:=21
115)    elseif T<Treheat then
116)        Vreheat:=10
117)    else
118)        Vreheat:=0
119)    end if
120)    if T<=1000 then
121)        step:=0.1
122)    elseif T<=1200 then
123)        step:=0.1
124)    else
125)        step:=0.01
126)    end if
127)    T:=T+Vreheat*step
128)    %exit when T>Treheat
129)    if T>=Treheat then
130)        T:=Treheat
131)        count:=count+1
132)        t_held:=count*step
133)        exit when t_held>=t_hold
```

```

134)     end if
135)     for i:1..N
136)         %N value should not be changed in all the calculation. otherwise the
           equation lose its meaning. In another word, the application of equation
           fv/fvo=(r/ro)^3 depends on the prerequisite, i.e., N is constant.
137)         r_tmp(i):=r(i)
138)         if r(i)>0 then
139)             time_diss:=r(i)**2/(k1*D1)
140)             if time_diss>step then
141)                 r(i):=sqrt(r(i)**2-k1*D1*step)
142)             else
143)                 r(i):=0
144)             end if
145)         end if
146)     end for
147)     for i:1..N
148)         if r(i)>0 then
149)             r_sum:=r_sum+r(i)**3
150)         end if
151)     end for
152)     f:=f0*(r_sum/r0_sum)
153)     if ( T>=Treheat and f<f1 ) then
154)         put "dissolution complete. t="t_held

```

```

155)         exit
156)     end if
157)     for i:1..N
158)         if f<f1 then
159)             %f:=f0*(1-(r0(i)**3-r(i)**3)/r0_sum)
160)             r(i):=r_tmp(i)
161)         end if
162)     end for
163) end loop
164) put "T=" .T-273
165) % Precipitate coarsening during holding.
166) const int_erg:=0.5/10**7 %j/cm^2
167) var V_NbCN, Nb_mol:real
168) var V_aust:=7.1 %cm^3/mol
169) var delta_r:array 1..N of real
170) var r_mean:real
171) V_NbCN:=x*13.5+(1-x)*12.7 %cm^3/mol
172) Nb_mol:=Sol_Nb(Treheat)*55.6/92.9 %mole conc.
173) var D_Nb:real
174) D_Nb:=Diffusion(Treheat) % in cm^2
175) var count_N:int
176) var sum_r:real
177) if T>=Treheat and t_held<t_hold then % coarsening happens.

```

```
178)    loop
179)        sum_r:=0
180)        count_N:=0
181)        for i:1..N
182)            if r(i)>0 then
183)                count_N:=count_N+1
184)                sum_r:=sum_r+r(i)
185)            end if
186)        end for
187)        r_mean:=sum_r/count_N
188)        t_held:=t_held+step
189)        exit when t_held>=t_hold
190)        for i:1..N
191)            if r(i)>0 then
192)                delta_r(i):=2*int_erg*D*(V_NbCN**2)*Nb_mol/(R*Treheat*r(i))
                                     *(1/r_mean-1/r(i))*step
193)                r(i):=r(i)+delta_r(i)
194)                if r(i)<0 then
195)                    r(i):=0
196)                end if
197)            end if
198)        end for
199)    end loop
```

```
200) end if
201) for i:1..N
202)     %put "r(",i,")=",r(i)*10**7
203) end for
204) put "f=",f, " f0=", f0
205) % Set group number and span
206) var M:=30    % number of groups
207) var grp:array 1..M of real
208) var grp_span:real:=2.5    % span between groups
209) for i:1..M
210)     grp(i):=0.
211) end for
212) % Determine Number of precipitates left after dissolution and coarsening
213) var N_eff:=0
214) for i:1..N
215)     if r(i)>0 then
216)         N_eff:=N_eff+1
217)     end if
218) end for
219) put "N_eff=",N_eff
220) % Determine mean precipitate sizes after dissolution and coarsening
221) var sum_r3:real:=0.
222) var r_avg:real
```

```

223) for i:1..N
224)     if r(i)>0 then
225)         sum_r3:=sum_r3+r(i)
226)     end if
227) end for
228) r_avg:=sum_r3/N_eff
229) put "r_avg=" .r_avg*10**7:8:2

230) % Determine standard deviation of precipitate sizes.
231) var sum_r2:real:=0.
232) var r_stdev:real
233) for i:1..N
234)     exit when i>N_eff
235)     if r(i)>0 then
236)         sum_r2:=sum_r2+(r(i)-r_avg)**2
237)     end if
238) end for
239) r_stdev:=sqrt(sum_r2/(N_eff-1))
240) put "r_stdev=" . r_stdev*10**7:8:2

241) % Calculate precipitate size distribution.
242) for i:1..N
243)     for j:1..M
244)         if r(i)>(j-1)*grp_span/10**7 and r(i)<=j*grp_span/10**7 then
245)             grp(j):=grp(j)+1

```

```

246)         end if
247)     end for
248) end for
249) var frq:array 1..M of real
250) var grp_size:array 1..M of real
251) var sum_r_frq:real:=0
252) var r_eq:real
253) put "  d". " ". "Frequency"
254) for i:1..M
255)     frq(i):=grp(i)/N_eff
256)     grp_size(i):=(i-1/2)*grp_span
257)     put 2*grp_size(i):5. " ", frq(i)
258)     if frq(i)>0 then
259)         sum_r_frq:=sum_r_frq+(grp_size(i)/10**7)*frq(i)
260)     end if
261) end for
262) % Calculate equivalent precipitate sizes and critical grain sizes
263) r_eq:=(r_avg**2+r_stdev**2)/sum_r_frq
264) put "r_eq=" .r_eq*10**7:8:2
265) var Rc, Rc_old:real
266) Rc:=4/9*r_eq/f
267) Rc_old:=4/9*r_avg/f
268) put "Dc=", 2*Rc*10**6. " ". "Dc_old=", 2*Rc_old*10**6

```


Appendix C. Calculation of Grain Growth during Induction Heating

This model was suggested by Anderson and Grong (1995). The basic assumption of this model is grain growth of C-Mn steels with precipitate pinning. The constants for grain growth of C-Mn steels have been used for this calculation. The critical grain size is calculated from precipitate evolution, which has been shown in the previous section. Numerical integration has been used for this calculation.

The following program is written in Turing language.

```

1)   var Q_app:=224000      % apparent energy for grain growth of C-Mn steel.
2)   const n:=2            %Grain growth constant of C-Mn steel.
3)   const R:=8.314
4)   var M_star:real:=exp(ln(2.14)+10*ln(10)) %the constant in Equation 2.30.
5)   var T:real:=700+273. % starting temperature.
6)   var Treheat:=1000+273.
7)   var Vreheat:real
8)   var count:int:=()
9)   var t_held, t_hold:real
10)  t_hold:real:=60
11)  var step:=0.01 % time interval 0.01s
12)  var R_int:real:=0. % the right side of Equation 2.30.
13)  var g_size:real
14)  var D_lim:real:=135.2 % critical grain size calculated from the previous program.
15)  var g_dia:real:=0.

```

```
16) var L_int:real:=0. % the left side of Equation 2.30.
17) % Start calculation.
18) % calculate the right side of Equation 2.30.
19) loop
20)   if T<=870+273 then
21)     Vreheat:=12.5
22)   elseif T<Treheat then
23)     Vreheat:=2.5
24)   else
25)     Vreheat:=0
26)   end if
27)   T:=T+Vreheat*step
28)   if T>=Treheat then
29)     count:=count+1
30)     t_held:=count*step
31)     exit when t_held>=t_hold
32)   end if
33)   R_int:=R_int+exp(-Q_app/R/T)*step
34)   g_size:=M_star*R_int
35) end loop
36) % calculate the left side of Equation 2.30.
37) loop
38)   g_dia:=g_dia+(step/10)
```

- 39) exit when $g_dia \geq D_lim$
- 40) exit when $g_size \leq L_int$
- 41) $L_int := L_int + (step/10) / (1/g_dia - 1/D_lim)^{(n-1)}$
- 42) end loop
- 43) put "g_dia=", g_dia

Appendix D. Chemical Driving Force for Precipitation of (Ti,V)(C,N) Type Carbonitrides

It is assumed that $(\text{Ti}_x\text{V}_{1-x})(\text{C}_y\text{N}_{1-y})$ precipitates are in equilibrium with the austenite. The free energy change (ΔG) associated with the formation of f mole of $(\text{Ti}_x\text{V}_{1-x})(\text{C}_y\text{N}_{1-y})$ precipitates in one mole of austenite matrix is given by:

$$\begin{aligned} \Delta G = & f \left(\frac{x}{2} \bar{G}_{\text{Ti}}^p + \frac{1-x}{2} \bar{G}_{\text{V}}^p + \frac{y}{2} \bar{G}_{\text{C}}^p + \frac{1-y}{2} \bar{G}_{\text{N}}^p \right) - \\ & + (1-f) (X_{\text{Ti}}^{\gamma} \bar{G}_{\text{Ti}}^{\gamma} + X_{\text{V}}^{\gamma} \bar{G}_{\text{V}}^{\gamma} + X_{\text{C}}^{\gamma} \bar{G}_{\text{C}}^{\gamma} + X_{\text{N}}^{\gamma} \bar{G}_{\text{N}}^{\gamma} + X_{\text{Fe}}^{\gamma} \bar{G}_{\text{Fe}}^{\gamma}) \\ & - (X_{\text{Ti}}^0 \bar{G}_{\text{Ti}}^{\gamma'} + X_{\text{V}}^0 \bar{G}_{\text{V}}^{\gamma'} + X_{\text{C}}^0 \bar{G}_{\text{C}}^{\gamma'} + X_{\text{N}}^0 \bar{G}_{\text{N}}^{\gamma'} + X_{\text{Fe}}^0 \bar{G}_{\text{Fe}}^{\gamma'}) \end{aligned} \quad [\text{C.1}]$$

where \bar{G}_i^p , \bar{G}_i^{γ} , $\bar{G}_i^{\gamma'}$ are the partial free energy of element i ($i = \text{Ti}, \text{V}, \text{C}, \text{N}$ and Fe) in precipitates, the remaining austenite and the original matrix, respectively. X_i^{γ} and X_i^0 are the mole fraction of element i in the remaining and original austenite. The equilibrium between austenite and the precipitates gives the following equalities:

$$\bar{G}_{\text{Ti}}^p = \bar{G}_{\text{Ti}}^{\gamma'} \quad \bar{G}_{\text{V}}^p = \bar{G}_{\text{V}}^{\gamma'} \quad \bar{G}_{\text{C}}^p = \bar{G}_{\text{C}}^{\gamma'} \quad \bar{G}_{\text{N}}^p = \bar{G}_{\text{N}}^{\gamma'} \quad [\text{C.2}]$$

where $\bar{G}_i^{\gamma'}$ indicates the partial free energy of element i in the austenite which is at equilibrium with the precipitates. Further more, the mass balances for Ti, V, C, N and Fe yield:

$$X_{\text{Ti}}^0 = \frac{fx}{2} + (1-f)X_{\text{Ti}}^{\gamma} \quad [\text{C.3a}]$$

$$X_{\text{V}}^0 = \frac{f(1-x)}{2} + (1-f)X_{\text{V}}^{\gamma} \quad [\text{C.3b}]$$

$$X_C^0 = \frac{fy}{2} + (1-f)X_C^I \quad [\text{C.3c}]$$

$$X_N^0 = \frac{f(1-y)}{2} + (1-f)X_N^I \quad [\text{C.4d}]$$

Substituting Equations C.4 and C.3 into Equation C.2 gives:

$$\begin{aligned} \Delta G = & \frac{1}{2}fx(\bar{G}_{Fe}^I - \bar{G}_{Fe}^I) + \frac{1}{2}f(1-x)(\bar{G}_V^I - \bar{G}_V^I) + \frac{1}{2}yf(\bar{G}_C^I - \bar{G}_C^I) \\ & + \frac{1}{2}(1-y)f(\bar{G}_N^I - \bar{G}_N^I) + X_{Fe}^0(\bar{G}_{Fe}^I - \bar{G}_{Fe}^I) + X_V^0(\bar{G}_V^I - \bar{G}_V^I) \\ & + X_C^0(\bar{G}_C^I - \bar{G}_C^I) + X_N^0(\bar{G}_N^I - \bar{G}_N^I) + X_{Fe}^0(\bar{G}_{Fe}^I - \bar{G}_{Fe}^I) \end{aligned} \quad [\text{C.5}]$$

Since the molar fractions of the nuclei are very small, it is reasonable to assume that

$\bar{G}_i^I = \bar{G}_i^I$. Also considering that $\bar{G}_i = {}^0G_i + RT \ln a_i$, Equation C.5 can be rewritten as:

$$\frac{\Delta G}{RT} = \frac{1}{2}fx \ln\left(\frac{a_{Fe}^I}{a_{Fe}^I}\right) + \frac{1}{2}f(1-x) \ln\left(\frac{a_V^I}{a_V^I}\right) + \frac{1}{2}fy \ln\left(\frac{a_C^I}{a_C^I}\right) + \frac{1}{2}f(1-y) \ln\left(\frac{a_N^I}{a_N^I}\right) \quad [\text{C.6}]$$

where 0G_i is the free energy of one mole of element i . a_i^I and a_i^I are the activities of the element in the austenite at equilibrium and in the original matrix, respectively.

If we consider the austenite as a dilute solid solution, the free energy change that accompanies the formation of a unit volume of $(Ti_xV_{1-x})(C_yN_{1-y})$ nuclei from the austenite can be expressed as:

$$\Delta G_{\text{chem}} = \frac{RT}{2V_m} \left\{ x \ln \frac{X_{Fe}^c}{X_{Fe}^0} + (1-x) \ln \frac{X_V^c}{X_V^0} + y \ln \frac{X_C^c}{X_C^0} + (1-y) \ln \frac{X_N^c}{X_N^0} \right\} \quad [\text{C.7}]$$

where X_i^c and X_i^0 are the equilibrium and bulk concentrations of element i in austenite, respectively. V_m is molar volume of the precipitates, which can be calculated by:

$$V_m = \frac{N_0 a_p^i}{8} \quad [\text{C.8}]$$

where N_0 is Avogadro's constant and a_p is the lattice parameter of the precipitates, which depends on the detailed composition of the nucleus. To accommodate this variation, it is assumed that the lattice parameter of mixed carbonitride is proportional to the mole fraction of each binary compound according to the law of mixture; that is:

$$a_p = xy a_{\text{TiC}} + (1-x)y a_{\text{VC}} + x(1-y) a_{\text{TiN}} + (1-x)(1-y) a_{\text{VN}} \quad [\text{C.9}]$$

where a_{TiC} , a_{VC} , a_{TiN} and a_{VN} are the lattice parameters of TiC, VC, TiN and VN, respectively. Their values are given in Table 2.3.

Appendix E. Calculation of Strain-induced Precipitation

The calculation of strain-induced precipitation is based on classic nucleation theory, which has been discussed in details in Section 6.4. The solubilities at reheat and deformation temperatures are calculated first. Chemical driving force, interfacial energy, and elastic energy when nucleating on dislocations are then calculated. Nucleation rate is then calculated based on classic nucleation theory. The transformation fraction of precipitates is calculated by the Johnson-Mehl equation.

The following program is written with Maple V for precipitation of Nb(C,N) in 1541Nb.

- 1) # materials constants.
- 2) MNb:=92.91: MC:=12.01: MN:=14.01: MFe:=55.85:
- 3) #Regular solution parameter LCN and gas constant R
- 4) LCN:=-4260: R:=8.314:
- 5) Avogadro:=6.023*10²³:
- 6) Latt_Aust:=2.86*10⁽⁻¹⁰⁾: Latt_NbC:=4.47*10⁽⁻¹⁰⁾:
- 7) Latt_NbN:=4.39*10⁽⁻¹⁰⁾: Burg_Vect:=2.5*10⁽⁻¹⁰⁾:
- 8) Int_Erg:=0.50:
- 9) Boltzmann:=1.38*10⁽⁻²³⁾:
- 10) Sigh_Disl:=0.4:
- 11) # the Nb,V and Ti composition(wt%) in the steel.
- 12) Nb0wt:=0.036: gammaFe:=8.0: C0wt:=0.40: N0wt:=0.005:

- 13) # convert wt% into at%.
- 14) $C0:=C0wt*MFe/(100*MC):$
- 15) $N0:=N0wt*MFe/(100*MN):$
- 16) $Nb0:=Nb0wt*MFe/(100*MNb):$
- 17) $\text{gammaNbC}:=7.84: \text{gammaNbN}:=8.41:$
- 18) $Tr:=1200+273: Td:=1100+273:$
- 19) $\text{stress}:=240*10^6: \# \text{ from the stress-strain curves}$
- 20) # the reheat temperature.
- 21) $T:=Tr+273:$
- 22) # solubility product(in wt%) of NbC.
- 23) $KNbCwt:=10^{(4.37-9290/T)}:$
- 24) # solubility product(in wt%) of NbN.
- 25) $KNbNwt:=10^{(4.04-10230/T)}:$
- 26) # convert solubility product from wt% into at%.
- 27) $KNbC:=(MFe/100)^2/(MNb*MC)*KNbCwt:$
- 28) $KNbN:=(MFe/100)^2/(MNb*MN)*KNbNwt:$
- 29) $\text{Coeff4}:= -MN*MC:$
- 30) $\text{Coeff3}:=2*Nb0*MN*MC-C0*MC*MNb-N0*MN*MNb:$
- 31) $\text{Coeff2}:=MNb*MN*KNbN+N0*Nb0*MN*MNb-$
 $Nb0*Nb0*MC*MN+MNb*MC*KNbC+C0*Nb0*MC*MNb:$
- 32) $\text{Coeff1}:=N0*KNbC*MNb*MNb-KNbN*Nb0*MN*MNb-$
 $Nb0*MNb*MC*KNbC+C0*KNbN*MNb*MNb:$
- 33) $\text{Coeff0}:= -KNbC*KNbN*MNb*MNb:$


```

34) Eq:=Coeff4*Nbswt^4+Coeff3*Nbswt^3+Coeff2*Nbswt^2+Coeff1*Nbswt+
    Coeff0=0;
35) solution:=fsolve( { Eq }, { Nbswt }, { Nbswt=0..Nb0 } );
36) assign( % );
37) x:=Nbswt*C0*MNb/(MNb*KNbC+Nbswt*(Nb0-Nbswt)*MN);
38) Nbppt:=Nb0-Nbswt;
39) Cppt:=x*Nbppt*MN/MNb;
40) Cswt:=C0-Cppt;
41) Nppt:=(1-x)*(Nb0-Nbswt)*MC/MNb;
42) Nswt:=N0-Nppt;
43) fNbC:=Cppt*(1+MNb/MC)*gammaFe/gammaNbC;
44) fNbN:=Nppt*(1+MNb/MN)*gammaFe/gammaNbN;
45) f:=fNbC+fNbN;
46) X_Nb0:=Nbswt;
47) X_N0:=Nswt;
48) xr:=x;
49) unassign('f','x','xr','Cppt','Cswt','Nppt','Nswt','fNbC','fNbN');
50) unassign('Coeff4','Coeff3','Coeff2','Coeff1','Coeff0');
51) unassign('KNbC','KNbN','Nbswt','Nbppt');
52) # Calculate again for the solubility at deformation temperature.
53) unassign('f','x','y','Nbs','Ceq','Neq','Nbswt','Nswt');
54) KNbCwt:=10^(4.37-9290/Td);
55) # solubility product( in wt%) of NbN.

```

- 56) $\text{KNbNwt}:=10^{(4.04-10230/Td)}$;
- 57) # convert solubility product from wt% into at%.
- 58) $\text{KNbC}:=\text{(MFe/100)}^2/\text{(MNb*MC)*KNbCwt}$;
- 59) $\text{KNbN}:=\text{(MFe/100)}^2/\text{(MNb*MN)*KNbNwt}$;
- 60) $\text{Coeff4}:=\text{-MN*MC}$;
- 61) $\text{Coeff3}:=2*\text{Nb0*MN*MC}-\text{C0*MC*MNb}-\text{N0*MN*MNb}$;
- 62) $\text{Coeff2}:=\text{MNb*MN*KNbN}+\text{N0*Nb0*MN*MNb}-\text{Nb0*Nb0*MC*MN}+$
 $\text{MNb*MC*KNbC}+\text{C0*Nb0*MC*MNb}$;
- 63) $\text{Coeff1}:=\text{N0*KNbC*MNb*MNb}-\text{KNbN*Nb0*MN*MNb}-\text{Nb0*MNb*MC*KNbC}$
 $+\text{C0*KNbN*MNb*MNb}$;
- 64) $\text{Coeff0}:=\text{-KNbC*KNbN*MNb*MNb}$;
- 65) $\text{Eq}:=\text{Coeff4*Nbswt}^4+\text{Coeff3*Nbswt}^3+\text{Coeff2*Nbswt}^2+\text{Coeff1*Nbswt}+$
 $\text{Coeff0}=0$;
- 66) $\text{solution}:=\text{fsolve}\{\text{Eq}\},\{\text{Nbswt}\},\{\text{Nbswt}=0..\text{Nb0}\}$;
- 67) $\text{assign}\{\%\}$;
- 68) $x:=\text{Nbswt*C0*MNb}/\text{(MNb*KNbC}+\text{Nbswt*(Nb0-Nbswt)*MN)}$;
- 69) $\text{Nbppt}:=\text{Nb0-Nbswt}$;
- 70) $\text{Cppt}:=x*\text{Nbppt*MN}/\text{MNb}$;
- 71) $\text{Cswt}:=\text{C0}-\text{Cppt}$;
- 72) $\text{Nppt}:=\text{(1-x)*(Nb0-Nbswt)*MC}/\text{MNb}$;
- 73) $\text{Nswt}:=\text{N0}-\text{Nppt}$;
- 74) $f\text{NbC}:=\text{Cppt*(1+MNb/MC)*gammaFe}/\text{gammaNbC}$;
- 75) $f\text{NbN}:=\text{Nppt*(1+MNb/MN)*gammaFe}/\text{gammaNbN}$;

- 76) $f:=f_{NbC}+f_{NbN};$
- 77) $X_{Nbe}:=N_{bswt};$
- 78) $X_{Ne}:=N_{swt};$
- 79) $xr:=x;$
- 80) # diffusion. Assume the diffusion the controlled by the slowest microalloying element, i.e. Nb.
- 81) $Diff_Nb:=492*10^{(-6)}*exp(-285000/(R*Td));$
- 82) #concentration. Asume the concentration is only dependent on the concentration of the lowest microalloying element. Ti in this case.
- 83) $X_{Nbp}:=MNb/(MNb+MN);$
- 84) # lattice of NbCN
- 85) $Latt_NbCN:=(Latt_NbC+Latt_NbN)/2;$
- 86) $Atom_Vol:=(Latt_NbCN)^{3/8};$
- 87) $Mol_Vol:=Avogadro*Latt_NbCN^{3/8};$
- 88) $Shear_Mod:=0.35*(12.6-0.007*(Td-1013))*10^{10};$
- 89) #chemical driving force
- 90) $Gv:=R*Td/(2*Mol_Vol)*(ln(X_{Nbe}/X_{Nb0})+ln(X_{Ne}/X_{N0}));$
- 91) #elastic energy
- 92) $Ge:=0.4*Shear_Mod*Burg_Vect^2*r;$
- 93) $\#Ge:=Shear_Mod*Burg_Vect^2*r*(ln(2*r/(2*10^{(-10)}))/(2*Pi)+1/5);$
- 94) # interfacial energy
- 95) $Gi:=4*Pi*r^2*Int_Erg;$
- 96) #Driving force when nucleating on dislocation or homogeneous nucleation.

```

97) Delta_G:=4*Pi/3*r^3*Gv+4*Pi*r^2*Int_Erg-Ge;
98) Delta_Gh:=4*Pi/3*r^3*Gv+4*Pi*r^2*Int_Erg;
99) Deriv:=diff(Delta_G,r);
100) plot({4*Pi/3*r^3*Gv,4*Pi*r^2*Int_Erg,-Ge},r=0..10*10^(-10));
101) plot({Delta_G,Delta_Gh},r=0..5*10^(-10));
102) plot({Gv,Ge,Gi});
103) fsolve(Deriv=0,{r=10^(-10)..10*10^(-10)});
104) assign(%);
105) Delta_Gv:=4*Pi*r^3/3*Gv:evalf(%);
106) #Delta_Ge:=0.4*Shear_Mod*Burg_Vect^2*r:evalf(%);
107) Delta_Ge:=Shear_Mod*Burg_Vect^2*r*(ln(2*r/(2*10^(-10)))/(2*Pi)+1/5);
108) Delta_Gi:=4*Pi*r^2*Int_Erg:evalf(%);
109) #dislocation density
110) Disl_Dens:=(stress/(Burg_Vect*Shear_Mod))^2;
111) #Zeldovich constant
112) Zeldovich:=Atom_Vol*Gv^2/(8*Pi*sqrt(Boltzmann*Td*
(Sigh_Disl*Int_Erg)^3));
113) #incubation time
114) Tau_Disl:=64*Boltzmann*Td*(Sigh_Disl*Int_Erg)^3*Latt_Aust^4/(Diff_Nb*
Burg_Vect^2*Atom_Vol^2*Gv^4);
115) #critical nucleation energy
116) G_Star:=(Delta_Gv-Delta_Ge+Delta_Gi):evalf(%);
117) #nucleation rate

```

```
l18) J:=Zeldovich*Disl_Dens*Diff_Nb/Latt_Aust^3*exp(-G_Star/(Boltzmann*Td));
l19) evalf(J);
l20) #supersaturation ratio
l21) Alfa:=sqrt(2*(X_Nb0-X_Nbe)/(X_Nbp-X_Nbe)*Diff_Nb);
l22) #volume fraction of precipitate
l23) X_t:=1-exp(-4*Pi/3*J*Alfa^3*3/5*t^(5/3));
l24) plot(X_t,t=0..50);
l25) # reset the variables for next calculation
l26) unassign('f','x','xr','Cppt','Cswt','Nppt','Nswt','fNbC','fNbN','J');
l27) unassign('Coeff4','Coeff3','Coeff2','Coeff1','Coeff0');
l28) unassign('KNbC','KNbN','Nbswt','Nbppt');
l29) unassign('f','x','y','Nbeq','Veq','Nbeqwt','Ceq','Neq','r','Tieqwt','Neqwt');
```

Acknowledgements

I would like to express my thanks to Dr. J.D. Boyd for offering this exciting Ph.D. opportunity and selecting such a challenging topic. As my supervisor, his extensive experience, constructive suggestions, continuous encouragement, and detailed personal care inspired me to fulfill this research work with great motivation. What I have learned under his supervision is far beyond the thesis itself.

I would like to acknowledge Dr. J. Cameron, Dr. S. Saimoto and Dr. P. Wild for their critical suggestions and fruitful discussions on the experimental design, data analysis, thesis writing and comprehensive exam.

I would like to acknowledge Dr. D. Baragar and D. Dolan for designing and performing the double-hit recrystallization test at CANMET.

I would like to acknowledge the members of the Department of Materials and Metallurgical Engineering for the favorable conditions they have created for my study, and for their direct and indirect help to this thesis.

Finally, I would like to acknowledge the financial support from the industrial consortium of TRW Canada, Chrysler Canada, ISPAT-Inland, Ivaco Rolling Mills, ISPAT-Dosco, Stelco Steel, Slater Steels, Timken, Welland Forge, the Natural Sciences and Engineering Research Council of Canada, and Materials and Manufacturing Ontario.